A new vision for 3D experiments on flow in porous media

Joachim Falck Brodin

Thesis for the degree of Master of Science

Department of Physics
Faculty of Mathematics and Natural Sciences
University of Oslo

May 2019

Abstract

The thesis concerns experimental work in the context of flow in porous media, a multi-disciplinary field coupling such topics as fluid dynamics, emergence, statistical mechanics and percolation theory. For reasons of both theoretical and practical appeal, the bulk of the studies in this field have been done on two-dimensional systems. Although this is deemed far from exhausted as an approach, the accumulated insight urges confrontation with the impact of scaling up to three dimensions. In this thesis, the development of a fully functioning 3D-optical-scanner, for experiments on flow in porous media, is detailed. The image processing, segmentation-, visual rendering- and data analysis-protocols are also presented, with high-resolution images and qualitative and quantitative system assessments. The thesis also offers a very promising trial experiment, producing novel results that are comparable, both with studies conducted in 2D and 3D, as well as the theoretical framework. Invasion in the direction of gravitational acceleration, of a denser more viscous fluid, into a synthetic porous medium, displacing a less dense, less viscous fluid, displays dynamic behavior ranging from unstable displacement and fingering, for slow injection rates, to stable displacement and a narrow front, for high flow rates. Calculated fractal dimensions and dimensionless scaling numbers, put these results into an established framework, with links to experimental studies and values derived from simulations with invasion percolation- and diffusion-limited aggregation- algorithms.

Acknowledgements

In the face of custom and tradition, I have to start this segment by thanking my wife, Mari. Were it not for you I would never have picked up my unfinished studies and ended up writing these pages. I considered myself to be too old and too tied down, with our kids, the finances and all that other stuff - you are the one that convinced me that it was not so. Since then you have supported me all the way. Thank you!

My supervisor, Knut Jørgen Måløy, already had staked out the course for the project that I have undertaken. He has always been available, and he has contributed immensely throughout, both with the lab-work and in the final revisions of this thesis. The experimental course I took with Knut Jørgen, during the first semester of the degree, was the perfect introduction to experimental physics. Knut Jørgen is one of the world's key players in the field of research the work falls under, and his experience and subtle leadership, alongside Eirik Flekkøy and the PIs in Trondheim, is part of what makes PoreLab an exciting and privileged place to be. The only thing Knut Jørgen is more passionate about than pouring liquids through stuff is skiing. I have to say that I did not expect to be outgunned in the slopes by my professor. I'll get you next year young man!

My second supervisor, Marcel Moura, is my junior by about ten years, but in the field of physics, he is way ahead. Marcel has been alongside me all the way, participating in some critical moments in the lab, and always as an advisor and guru! Like me Marcel has a slightly subversive nature, he is deeply passionate about the work, but he also does not hide his conviction - it should be fun. I hope that our collaboration will continue, but I also slightly fear that we one day may be synchronized in our secret fantasy, to find out how much of a bang we can get out of the lab.

Eirik Flekkøy is one of my favorite oracles and has provided insight into many issues during my studies. It was in part his very inspiring course on quantum physics that brought my attention to PoreLab in the first place. His course on the theoretical aspects of our work has been invaluable for this work.

Nothing goes on in PoreLab without Mihailo Jankov having a hand in it. Mihailo

is probably the one that I have spent the most time within the group, as he also skulks in the basement like me. Mihailo and I are in a similar life situation, with the kids, house station-wagon and all - heavily subjected to the second law of thermodynamics - we find great consolation in our mutual suffering! I appreciate greatly your presence and the invaluable help you have provided!

Per Arne Rikvold came to join PoreLab the summer of 2018, after a distinguished career at Florida State University. The only truly brilliant thing I did in the entire master's project was to ask Per Arne if he would like to participate as a collaborator with my work. Per Arne is immensely experienced and knowledgeable, he has very graciously given me access to some of these resources, and this has been truly invaluable. Per Arne is by far the best proofreader and bullshit detector I have met. He has an excellent command of the English language and is a likewise keen mastery of physics. His revisions and comments to these written pages, through many rounds, have been extremely educating and, in my esteem, have been instrumental to whatever qualities the text might hold. I hope that this is only the beginning!

Francois Renard very timely has been going on for years using precisely the tool I needed to make a giant leap in the 3D-rendering and data-processing. He has been extremely generous, both in granting me instant and unlimited access to his computer lab, and in giving me the introductory lessons in using the software that I needed to get out of the starting pit.

I remember Arnt Inge Vistnes already form my first half-hearted studies in the early 2000s. This time around he has been a felt presence at the institute, both in his role in coordinating the education and with very inspiring lectures in the course that he is the creator and master of, *Physics of Oscillations and Waves*. Arnt Inge gave me very pointed and enlightening feedback on the sections on light physics and optics. This help was exactly what I needed, to unclog the stoppages and get the chapter into the shape I desired!

Torbjørn Skauli provided insight through two courses on optics and imaging systems, that have been essential for the work conducted in the project. Torbjørn also gave me some very encouraging feedback on during the writing process. I am sure we have not seen the last of one another!

I have also enjoyed the company of all the other people on the floor. Beatrice Baldelli, Fredrik Eriksen, Kristian Olsen, Le Xu, Monem Ayaz, Louison Thorens, James Campbell, Guillaume Dumazer, Antoine Léo Turquet, Luiza Angheluta-Bauer, Pavlo Mikheenko, Joakim Bergli, Mathias Reistad, Vegard Sørdal, Hilmar Birgisson and Nina Mino Thorud - all in particular - you have all helped me in one way or the other throughout the last two years. Thank you!

When I started on the second round of physics studies in 2015 Anders Malte-Sørenssen wished us all welcome as new students. Standing there, with my 20-year old soon to be fellow students, I chuckled when he told us about how we were about to meet the people that would probably be our best friends throughout the rest of our lives. In spite of myself, I have actually made some friends that might qualify, in particuar Henry Melikan and Peter Ørnulf Ivarsen!

I also have had good use of my many already best friends; Arthur, Vemund, André, Jørn, Håvard, Snorre, Mattias, Marius, Richard, Håkon and Christoph, to name a few.

I also have to thank André Viervoll (again), Lars Hamre and Tom Erik Skram at Newtone Studios, for their help with the design and construction of the flow-cells used in the experiments.

I also send warm thoughts to the sales representatives and technical support of the many companies I have communicated with to find solutions during this project, in particular Paul Cahill from Exciton and Julien Roussel and Jan Giesebrecht from Thermo Fisher Scientific.

Back on the personal note, I also would like to send some thoughts to our two boys, August and Eirik. Although I would say that I have done this work in spite of you rather than thanks to you, I still love you! By the way, if either of you ever opens up these pages and read even a single word of it - you are certainly up for ice cream.

My parents, Inger and Pål, have always stood up for me, and have been very encouraging and supportive throughout the whole period of both my first (they hoped against hope that I was actually studying) and second studies. I have it from an anonymous source, that I am a bit of a spoiled brat that never really have had to deal with any real problems - I guess I have you two to thank for that!

Preface

On the off chance that this thesis should fall into the hands of someone else in the middle of their masters or bachelor studies, I would like to use the opportunity to share a few methods, or tricks, that I have found useful during my studies.

In my experience, the academic staff at the university are highly involved and greatly motivated, both in their research and in their teaching. There is nothing they like more than likewise eager students. The lecture halls and seminar rooms are both dull and uninspiring unless we all participate. Asking questions and taking active part is vital, both to the ambience and to the quality of the sessions. Also, it is by far the most effective way to clear up the clogs that inevitably form when trying to grasp complex issues.

I have shamelessly asked and poked in my years at the university. Although I consider that I have worked quite independently on this masters project, there have been a great number of people involved, both in the experimental phase and in the development and revision of the text. This is actually not considered cheating! Certainly, the history of science contains monolith achievements by solitary geniuses, but these are exceptions. In general, science is a team effort. I recommend signing up!

Another little trick is to try to be ahead, rather than behind. There never is a way to know what you will run up against in a science project! I was fortunate in that I was aiming to finish a half year ahead of schedule. When the deadline approached I had come a far way towards this, but it turned out to not be realistic. It did, however, make me able to have what I considered a nearly finished manuscript, one month ahead of the *final* deadline.

I cringe at the thought of having just barely escaped handing in that rag! The extra month has given room, not only to discover a stunning amount of typos missing commas, and shocking errors, but it has also allowed for proofreading and feedback from other people. I cannot stress strongly enough how valuable this has been - to me, my understanding of the subject matter, and indeed to this thesis!

Finally, I strongly advise everyone attempting to do anything, to be motivated. If you are not, probably you are better off doing something else, at least until you are motivated again!

Contents

CHAPTER 1

Introduction

The somewhat pompous title of this thesis, *A new vision for 3D experiments on flow in porous media*, is both misleading and at the same time highly accurate. Experimental work on flow in porous media in 3D has been done for some time, but it is something that still must be considered to be at a very early stage. The focus of this project has not been to formulate a grandiose new vision in an abstract or theoretical sense, but rather to provide vision in the most concrete regard possible, in the form of a solution to allow common optical sight, in a place that has so far remained invisible.

The experimental work that is treated in this paper was conducted at PoreLab at the University of Oslo. PoreLab is a new center of excellence with a section at UiO in Oslo and one at NTNU in Trondheim. On the center web-page, one can read that the center joins three fields of science: hydrodynamics of porous media, non-equilibrium thermodynamics, and statistical mechanics. Specifically, the work is focused on what is termed *flow in porous media*. A porous medium is a solid with cavities. When the holes are interconnected, a fluid can flow through. The dynamics of such flow are startlingly complex, and it is something we have only begun to understand.

Fluid mechanics play a significant role in the phenomena studied by PoreLab, but the group has its roots more in the study of what can be called *complex systems* and statistical mechanics. A trend is that we try to understand the phenomena, through the patterns and geometries that can be observed. When we do computational simulations to imitate the physical behavior behind intricate patterns, such as those formed by ice crystals, or when mud dries and cracks up, we start from elementary building blocks, that alone has few attributes. What happens when several are put together though, is usually far from simple. I used to work as a carpenter, building wooden houses. When I was to erect say a balcony or an overhanging roof, supported at the front by two square posts, it was of importance that they appeared straight and had their best face outwards. I would try to pick two very suitable lengths, from the stack of framing wood, and then consider how to cut and place them. It did, however, not occur to me to calculate that there are 128 ways to combine

the posts even after I had cut them [1]. When you expand such combinatorics, to the whole balcony, the alterations very quickly reach astronomical numbers. You do not have to go far before the calculator runs out of digits. Should you try for the whole house, the amount would far exceed the number of atoms in the known universe, or that number to the power of itself, for that matter. This is what we call *emergence*, and it is what allows us to assume that the complex behavior we observe is the result of a finite number of relatively simple interactions, that we hopefully can describe with equations.

Flow in porous media is a field that is of relevance for a range of industrial applications, such as the extraction of oil from reservoirs or the development of more durable cement. It is also a field relevant to the understanding of structure and transport in biological and geological systems. For me, it is most of all an area related to the universal quest for understanding the universe - what we are made of and how it all works together. I find it to be an intriguing field, for its technique is to start from the simple and understandable, using methods and reasoning that are both humble and intuitive - but always leading to the complex and interconnected. It is a field where the theories can be readily tested, as the results are visible and tangible. You can see, touch and understand the matter you are probing.

Figure 1.1: *Picture from a quasi 2D experiment, conducted at PoreLab, with a Hele-Shaw cell, by Louison Thorens. The sample was prepared with a porous medium, saturated with dark liquid. The flow experiment was conducted by withdrawing liquid through a valve at the center of the sample. The air displaced liquid in fingers that formed a pattern, from the perimeter. Different flow rates produced different patterns.*

Flow in porous media has been studied experimentally in 2D since at least 1898 [1], when Henry Selby Hele-Shaw conducted experiments, introducing what has later been known as Hele-Shaw flow. It is an experimental set-up that has an immediate practical appeal. The essence of the set-up is two parallel glass plates that are minutely separated. Flow can then occur between the plates, and since the plates are made of glass, everything can be seen directly, and also be easily documented, by merely taking a picture or filming - with an entirely standard camera. As the movement is strictly limited in the direction

[1] The calculation goes as follows: There is the choice of which post goes left and which goes right, giving two options, combinations of what ends goes up and what ends goes down offers four possibilities, and finally, for each of the four faces left outward on one side, there are four alternatives on the other, thus contributing 16 outcomes. The total number of permutations then becomes $2 \cdot 4 \cdot 16 = 128$.

parallel to the plates, it is a reasonable approximation to consider the flow as happening purely in the plane of the plates - often dubbed quasi-2D flow. This set-up is still actively used, and it has not been exhausted - there are still phenomena that are not studied nor understood. The 2D set-up also has the obvious advantage of being easier to simulate and to derive theory on. In figure (1.1) a flow pattern, resulting from an experiment in a Hele-Shaw cell, can be seen.

Reality is not limited to a plane. It is of apparent interest to be able to conduct these experiments in 3D. The problem is that in a regular 3D-porous medium it is not possible to see inside, at least not without the use of special techniques, such as x-ray tomography. They have the disadvantage of necessitating very expensive and hard to get by machinery, limiting the flexibility and extent of the experiments.

One of the topics that have sparked interest in me, during my physics studies, has been the physics of light and the way it interacts with matter. It was not difficult to choose a project for me, as the first one proposed by my supervisor was right up my alley: namely to build a contraption to optically record flow in a porous medium in 3D and conduct an experiment with it. What was aimed at, is a rig that allows for 3D-flow experiments to be performed in the workflow and environment of our local lab, with similar flexibility and simplicity as the Hele-Shaw cell offers.

The basic idea behind the set-up is by no means mine. My supervisor, Knut Jørgen Måløy outlined the principal components, and he, in turn, has been inspired by similar ongoing projects from other groups around the world. A diagram of the initial idea can be seen in figure (1.2).

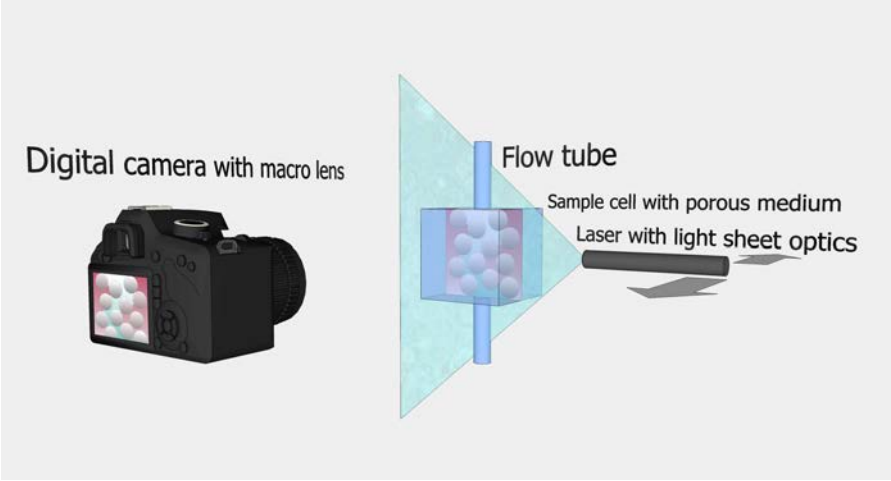

Figure 1.2: *The initial idea for the 3D-flow scanner.*

The idea is both brilliant and straightforward: make the sample transparent. What it means when we call something *transparent*, is that it lets visible light

pass through, like a window or a glass of water. The relevant parameter, of such a transparent medium, is its *refractive index*, this is a number larger than or equal to 1, that relates how much light is slowed down, compared to the light speed in a vacuum, when passing through the medium. When two media of different refractive index meet, they form an interface, where reflection and refraction occur, leading to distortions and loss of light. By using medium and liquids of closely matched refractive index, such interfaces become invisible, and a transparent sample that does not distort can be achieved. Still, we cannot see either the medium or the liquids, but this can be overcome by putting fluorescent dyes in the liquids and illuminating them with a laser.

By using two immiscible fluids and dissolving different fluorescent molecules in each liquid, they will radiate at different wavelengths and thus be separable. The medium should then remain transparent, while the fluids should appear as shining clouds of different colors. The laser light can be fanned out in a sheet, which in turn can be passed through the sample. It should be possible to depict the layer as it passes through the sample by a regular camera. From the collected frames, we can then construct a 3D-rendering of the sample.

This thesis is in the framework of experimental work. In the second chapter, I will outline the theoretical framework that experiments on flow in porous media relate to, as well as the relevant theory concerning the optical and other aspects that went into consideration. In the third chapter, the experimental process will be detailed, both as documentation of the steps leading to the particular results and as a hopefully helpful reference to anyone who might wish to replicate the whole, or parts, of the process. The fourth chapter contains the results I have arrived at. The fifth includes a discussion of the process and the results, with my thoughts on how to proceed with the work. I have tried to adhere to the formal template used for articles and theses within physics, but I have taken some liberties as I find that the format sometimes communicates poorly. For instance, I believe that figures and associated results or discussion should be placed so that it is possible to easily see the figure as one reads the text. Trivial practical points of discussion have been handled as the sections progress, and in the end, I have summed up a general discussion, possible with some repeated arguments from the previous sections.

I finish the thesis, like I begin, on a personal note. The final stop, the postface, can be read at your discretion.

CHAPTER 2

Theory

The study of the dynamics of flow in porous media is a multi-disciplinary endeavor. Incorporated is the entire body of fluid dynamics, coupled with such as statistical mechanics and the study of complex geometries. The field is quite young, but it is increasingly gaining interest and focus, as we come to realize that the type of processes it encompasses are present in a much wider range of phenomena than what could have been anticipated.

As much as this work has been about flow in porous media, it has also been about how to meaningfully record and present it - about light, optics, fluorescence, image analysis, and rendering and presentation. In this section, I aim to present some of the key theoretical concepts that I have considered in the experimental work.

2.1 Porous media

A porous medium is a solid that contains voids. A typical example could be sandstone or the bones in our bodies. When the voids are interconnected, they permit the passage of gasses and fluids. Such motion through the medium is often called *flow in porous media. A porous medium can be deformable or static, it can be made up of loose or cemented grains, rigid or elastic fibers, it can be uniform or diverse, and it can be ordered or disordered.*

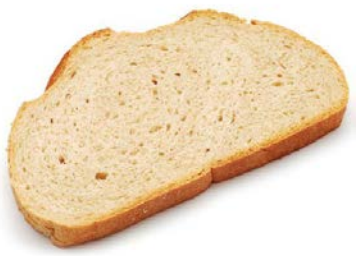

Figure 2.1: *Bread is a porous medium. The structure of interconnected and isolated voids in the mesh of dough is illustrating the types of structures we are considering. A noteworthy feature of bread is that the fractal nature of the medium is observable with the naked eye, as one can see the structure of voids and solid repeating itself on a smaller scale in the strands of dough [2].*

2.1.1 Porosity

The first parameter we come across, when dealing with porous media, is the ratio of void to the total volume, labelled *porosity*,

$$\phi = \frac{\text{pore volume}}{\text{total volume}} = \frac{\text{total volume - solid volume}}{\text{total volume}} = 1 - c, \qquad (2.1)$$

where c is the filling fraction.

2.1.2 The structure of the porous medium

Many natural processes lead to the formation of porous media. While there are parameters that are common to all of these, such as the porosity, there are other parameters that make more or less sense, depending on the specific structure.

When we do laboratory experiments, it can be convenient to look at a more homogeneous or ordered medium. A common way is to use grains of a given structure, such as spherical beads or rod-shaped particles. Thus a more reproducible medium can be made, and further structural parameters can be defined.

Using spherical beads of uniform size is common. When poured out on a flat surface in one layer, and then compacted while shaking or tapping, inside of the formation the beads order themselves in the densest possible formation, in a triangular lattice. However, unless the overall frame the beads are in perfectly matches the triangular organization, the edges become disordered, a phenomenon labeled *frustration*. An example can be seen in figure (2.2).

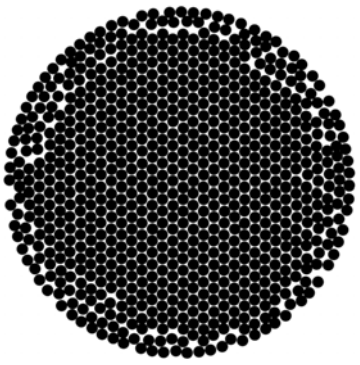

Figure 2.2: *In the center of the formation the disks are perfectly ordered in a triangular lattice, but as this does not fit into the outer circular shape, the pattern becomes disordered, or frustrated, towards the edge [3].*

As it turns out, the same does not happen in 3D. The beads do not compact in an ordered lattice, no matter how one shakes or taps the container [4, 5]. To achieve an ordered packing the spheres must be deliberately stacked. The densest possible packing, of spheres of uniform size, is in fact an ordered stacking, where both so-called *face centered cubic* (fcc) and *hexagonal close-packed* (hcp) lattices achieve the highest possible filling fraction: $c = 1 - \phi = \pi/3\sqrt{2} \approx 0.74$

[6, 7]. The reason the beads do not spontaneously order themselves, in such a formation, is that they lodge against one another. For a bead to be held in place, it only needs to be in contact with three other beads. As soon as this happens, it cannot move. In the densest packing formation, each bead is in contact with 12 others, which is the maximum possible. Experiments with random close packing show that in realistically scaled experiments this will not occur [4].

In an ordered stacking the beads will convey the forces exerted by a potential, such as gravity, in uniform, ordered strands. If one, for instance, makes an ordered cubic lattice, where each layer of balls is placed directly on top of the next, each stack will act as a column and carry only its weight. In a random packing, the forces tend to be held by branchlike lines throughout the structure, retaining most of the load from the layers on top, leaving the balls in between suspended as on shelves. Within each "shelf" the pattern repeats, distributing the forces in smaller branches [5, 8, 9].

Experiments show that, for spherical beads of uniform size, *random loose packing* (rlp) on average leads to a filling fraction of $c \approx 0.55$ [4], with each bead in contact with an average of 7.1 others. For *random close packing* (rcp) $c \approx 0.64$, with an average of 7.9 contacts per bead [4]. In comparison, stacking the beads in a *simple cubic lattice* gives a filling fraction of $c = 0.52$ [1].

In the end, this means that a random packing of uniformly sized spheres, will each time create a unique structure, even if produced in the same container, with the identical spheres, but the porosity will each time be nearly the same (especially if one disturbs the container so as to create a close packing). So will the overall structure, making it possible to introduce further parameters in terms of how a liquid or a gas inhabits and moves through the medium.

2.1.3 Pore volume

Figure (2.3) is a simplified 2D-illustration of flow in a porous medium. One of the parameters used to characterize the medium is the pore volume. Here, the volume of a single pore is confined by the line segments d_1, d_2 and d_3 and the disks. Although each pore is not the same size, they are of the same order of magnitude, and when the medium is disks or spherical beads one commonly refers to the diameter of the beads as the *characteristic scale*, which in turn is of the same order of magnitude as the *pore volume*.

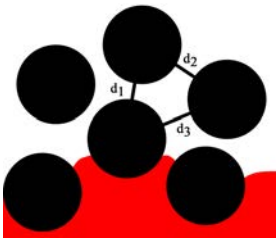

Figure 2.3: *Schematic of two-phase flow in a porous medium. The black disks are the solid that make up the matrix, and the red and the white are the two fluids.*

[1] This is quite straightforward to calculate, as the fraction of volume a sphere of radius r to that of a cube with sides $2r$, $c = (4/3)\pi r^3/(2r)^3 = \pi/6 = 0.52$.

Furthermore, we define the *pore throats* to be the openings between the pores, where the passage is at its most narrow, given as the line segments d_1, d_2 and d_3 in figure (2.3).

2.1.4 Saturation

The saturation is the fraction of one liquid to the total pore volume (assuming two liquids together occupy the entire available pore volume). In the case from figure (2.3), where we have a red and a white liquid, this yields

$$S_{red} = \frac{V_{red}}{V_{pore}} \tag{2.2}$$

$$S_{white} = \frac{V_{white}}{V_{pore}}, \tag{2.3}$$

where $S_{red} + S_{white} = 1$.

2.1.5 Percolation

Percolation has become a field of study in itself, but the term *percolation* means that something is filtering through a medium. For this to happen, the matrix of the medium must be interconnected in such a way that an invading fluid can find its way through, from one end to the other. When the liquid emerges on the far side, we say that it is *percolating*.

2.2 Fluid properties

For a physicist the word *fluid* means a liquid or a gas. The two share many properties and can be described by similar dynamics. The main distinction between the two is that liquids generally have a far greater density than gasses and that gasses are more compressible than liquids. Much of solid matter, so-called *crystals*, also share much of the same dynamic description, but the fluidity of such substances occurs at a much slower rate and is not observed in our everyday contexts.

2.2.1 Density

The density, ρ, is defined as the mass per volume,

$$\rho = \frac{m}{V}, \tag{2.4}$$

where m is the mass and V the volume. Common units for density are [g/cm^3] or [kg/m^3].

2.2.2 Compressibility

An essential feature of a fluid, when we derive laws for its dynamics, is its *compressibility*. If we can assume non-compressibility, we can take that, the same mass of liquid will occupy the same amount of volume, regardless of fluctuations in pressure or temperature, this eliminates a complicating factor and allows for a less complex description. Formally, the *compressibility* β is a measure of the relative volume change of a fluid as a response to a pressure change, expressed as

$$\beta = -\frac{1}{V}\frac{\partial V}{\partial p}, \tag{2.5}$$

where V is volume and p is pressure. The compressibility has units [Pa^{-1}] or [m^2/N]. Incompressibility is an idealisation, as no matter is truly incompressible, but it is one that holds well within reasonable margins of error when dealing with quasi incompressible fluids [10].

2.2.3 Viscosity

The viscosity of a liquid is the measure that quantifies the reciprocal of the "fluidity" of the liquid, informally called thickness. Technically it is the measure of the liquid's resistance to gradual deformation by shear stress, or more simply put - a measure of the friction between the molecules in the fluid. Except for superfluids, which have the special feature of having no such friction, all liquids have positive viscosity [11].

We use two different parameters to quantify viscosity - *dynamic*, μ, with common units [mPa·s] or [cP], and *kinetic* viscosity, ν, with units [mm^2/s]. The relation between the two is given by

$$\nu = \frac{\mu}{\rho}. \tag{2.6}$$

2.2.4 Ideal fluids

In the following, an *ideal fluid* is an idealized fluid, with the following constraints:

- It has zero viscosity.
- It is incompressible - the density is constant, in time and in space.
- The force exerted across a surface element $\mathbf{n}\mathrm{d}S$, within the fluid, can be expressed as $\boldsymbol{F} = -p\boldsymbol{n}\mathrm{d}S$, where p is a scalar value, representing the pressure, and $\boldsymbol{n}$ is a unit vector, normal to the surface element.

2.2.5 Newtonian fluids

A Newtonian viscous fluid is an idealized fluid where the shear stress τ is proportional to the velocity gradient $\mathrm{d}u/\mathrm{d}x$ such that

$$\tau = \mu\frac{du}{dx}, \tag{2.7}$$

where μ is the dynamic viscosity [12].

Another interpretation would be to say that the viscous stresses arising from the flow are, at every point, linearly proportional to the local strain rate - the rate of change of deformation over time [13].

2.3 Two-phase flow in porous media

When considering flow in porous media there are many factors that come into play. Some of the parameters to consider are:

- The wetting properties
- The characteristic length scales and geometry of the matrix
- The dimensionality of the system
- The viscosities of the fluids
- The compressibilities of the fluids
- The flow velocity
- Gravity-effects
- Temperature-effects
- Capillarity and surface tension
- Chemical reaction between the fluids and between the fluids and walls
- Deformations of the porous media
- Fracturing of the porous media
- Effects from electric and magnetic fields

It is entirely possible that there are other factors that we do not commonly consider that could be of importance. Already, the list of interacting parameters is long enough to make the modeling over-complex. It is therefore desirable to try to eliminate some interactions and focus the elaboration on a few at a time, by for instance doing such as looking at fluids that do not react chemically with one another, or by flowing horizontally, to limit the effects of gravity.

2.3.1 Volumetric flow rate and volumetric flux

The volumetric flow rate, Q, is defined as the volume of fluid that passes through a given surface per unit of time, with units $[\mathrm{m}^3/\mathrm{s}]$. The volumetric flux, q, is the rate of volume flow across a unit area, with units $[\mathrm{m}^3/\mathrm{m}^2\mathrm{s}]$.

2.3.2 Surface tension - the Young-Laplace equation

The physical properties of a fluid in contact with another, with which it is immiscible, are different at the surface than inside the bulk material. The interactions with neighboring molecules become different, as the molecules at the surface no longer are surrounded, on all sides, by other molecules of the same type. Between molecules of the same type, there are attractive, *cohesive*, forces. Near the interface between the liquid and the gas there are weaker, *adhesive*, forces. The result is that the interface behaves as if it was a stretched membrane

under tension. When the membrane is curved, it gives rise to a pressure jump across the interface, in equilibrium this pressure gradient is countered by the parallel components of the forces arising from the surface tension, tangential to the interface. As a system moves towards equilibrium, the free energy is reduced, and the entropy increased. A droplet of one liquid immersed in air minimizes the free energy by minimizing its area per volume, thus forming a sphere [14]. To then increase the surface requires work. The amount of work per unit surface increase is defined as the surface tension,

$$\gamma = \frac{dW}{dA} \tag{2.8}$$

The unit of surface tension is thus [J/m^2] or [N/m], energy per unit area or force per unit length.

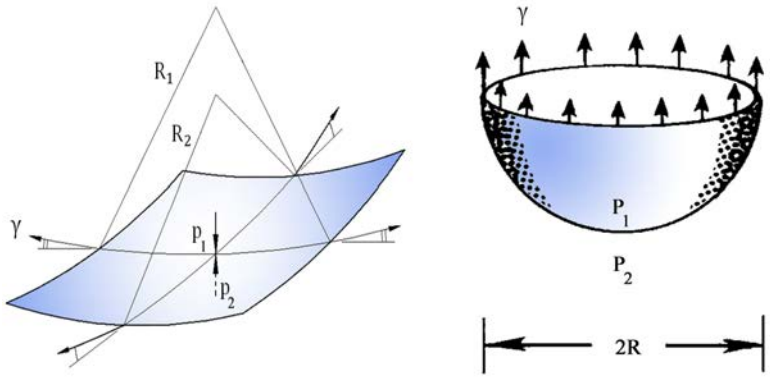

Figure 2.4: *Illustration of the interface between two fluids. R_1 and R_2 are the radii of curvature and p_1 and p_2 are the pressures at either side of the interface. On the right we see the cross section of a spherical drop.*

In figure (2.4) an interface between two fluids is illustrated. If the surface is curved in equilibrium, there will be a pressure jump across the interface. In the spherical case, where $R_1 = R_2$ this gives the force balance

$$\gamma 2\pi R = (p_1 - p_2)\pi R^2 \quad \Rightarrow \Delta p = \frac{2\gamma}{R} \tag{2.9}$$

Analysis with orthogonal radii of curvature that are different leads to the Young-Laplace equation,

$$p_1 - p_2 = \gamma \left(\frac{1}{R_1} + \frac{1}{R_2} \right). \tag{2.10}$$

2.3.3 Wettability

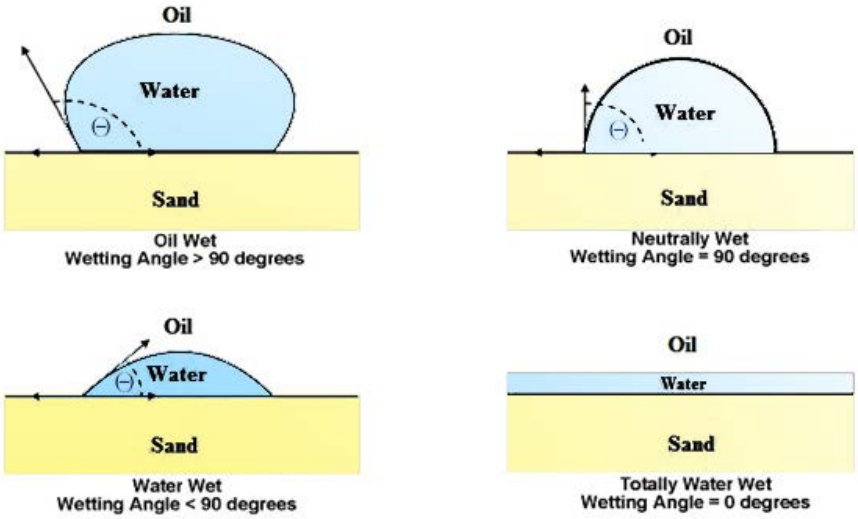

Figure 2.5: *Examples of how different wetting angles affect the wettability.*

Wettability is defined as the tendency of one fluid to spread on or adhere to a solid surface in the presence of other immiscible fluids. This spreading tendency can be quantified by measuring the angle of contact at the liquid-solid interface. Figure (2.5) shows how different wetting angles can be measured to define whether a fluid wets a surface or not. A perfect wetting fluids wets a surface fully and render a wetting angle of $\theta = 0°$. If the wetting angle is in the interval $0° \leq \theta \leq 90°$ we say that the fluid is *wetting*, if the wetting angle is in the interval $90° \leq \theta \leq 180°$ we say that the fluid is *non-wetting*. The wetting properties are given by the competition between the cohesive internal forces of the fluid, and the adhesive forces between the fluid interface and the solid.

2.3.4 Capillary pressure

If we insert a narrow tube, such as a straw, into a liquid, the liquid rises or falls in the tube, as can be seen in figure (2.6). If the liquid wets the surface of the tube, we get a capillary rise, and a non-wetting fluid leads to a capillary depression.

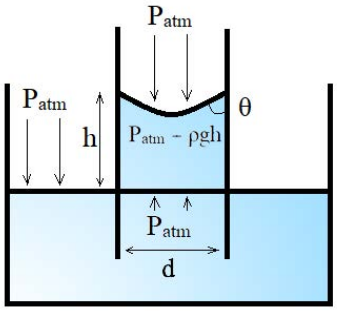

Figure 2.6: *Hydrostatic pressure inside a capillary tube.*

The pressure difference between the surroundings and inside the fluid, near the interface, is given by the hydrostatic pressure $\Delta p = \rho g h$. The balance between the adhesive force of the liquid stuck to the wall, pulling up by surface tension, and the weight of the water column, pushing down, is given by

$$\pi d\gamma \cos\theta = \pi \left(\frac{d}{2}\right)^2 \rho g h$$

Solving for γ,

$$\gamma = \frac{\rho g h d}{4\cos\theta}. \tag{2.11}$$

2.3.5 Drainage and imbibition

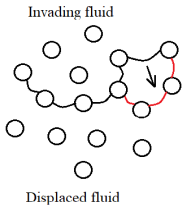

Figure 2.7: *Drainage: the non wetting fluid displaces the wetting fluid.*

We can distinguish between two types of flow, according to the wetting angle in the interface of the invading and displaced fluids. *Imbibition* occurs when a wetting fluid displaces a non-wetting fluid, and *drainage* when a non-wetting fluid displaces a wetting fluid. In figure (2.7) we see an example of drainage.

2.3.6 Equations of motion - Navier-Stokes equations

In this section, an abbreviated presentation of the developments leading to the Navier-Stokes equations will be given. The derivations are not complete, in the

sense that all the underlying assumptions and proofs are not represented, but the steps are referenced from more extensive sources [3, 12, 15].

One of the most fundamental concepts, for the following, is the notion of continuity. The assumption, that everything that is can only be displaced via continuous paths, in space and in time.

Equally fundamental is the notion of energy conservation, from the first law of thermodynamics. When summed up, the total energy (in all its forms), of an isolated system, is preserved. In the following, the assumption of conservation is separated, into the conservation of mass and the conservation of momentum. For the conservation of mass, the continuity equation reads

$$\frac{\partial \rho}{\partial t} + (\nabla \cdot \rho \boldsymbol{u}) = 0, \tag{2.12}$$

where ρ is density, t time and $\boldsymbol{u}$ is a vector field, containing the direction and magnitude of velocity, as functions of positions in time and space.

Together, continuity and conservation, allow for a system of accountability - what is there at one point in time, can be accounted for again, at another point in time - thus we can make equations.

An equation of motion describes the magnitude and direction of velocity, as a function of position and time. If one assumes that all the relevant dynamics follow strict causal laws, and one can account for all the rules governing a system, as well as all data describing the appropriate conditions at one given time - it should be possible to derive an equation to represent the conditions - at any other time.

An important question, when it comes to equations of motion for fluids, is: *What exactly* do they describe the action of? When we have a glass of water sitting on the table, there are dynamics in the water, on at least three levels. The first one is the unified, macroscopic movements that we observe. Unless we perturb the glass or liquid, nothing seems to be happening. Secondly, there is the flow due to thermal gradients and residual turbulence in the fluid, observable to the naked eyes, if one, for instance, stirs inn visible particles that remain suspended. Finally, there are the interactions at the molecular level, where every single molecule is randomly bouncing about, with average kinetic energy proportional to the ensemble temperature of the liquid.

To quantify something that we can derive an equation of motion for, we use what we call a *fluid element*. It is a volume that is carried and deformed, by the velocity field that governs the intermediate level, described in the previous paragraph. The fluid element is an artificial concept, as any such element, in a real fluid, regularly exchanges molecules with the surroundings. However, it is one that can be worked with. Most importantly, it captures the net transport of fluid, which, for many applications, is the result we are after.

In 1755 [12] Euler formulated, what is perhaps the first equations of motion for

an ideal fluid (as defined in section (2.2.4)), on the form

$$\frac{\partial \boldsymbol{u}}{\partial t} + (\boldsymbol{u} \cdot \nabla)\boldsymbol{u} = -\frac{1}{\rho}\nabla p + \boldsymbol{g}, \qquad (2.13)$$
$$\nabla \cdot \boldsymbol{u} = 0,$$

where $\mathbf{u}$, ∇p and $\mathbf{g}$ are vector fields, describing the magnitudes and directions of velocity, pressure gradient and gravitational force, at position $\mathbf{r}$ and time t, and ρ the fluid density. The second line signifies that the divergence is zero, meaning that the liquid is incompressible.

By introducing the substantive derivative

$$\frac{D}{Dt} = \frac{\partial}{\partial t} + \boldsymbol{u} \cdot \nabla, \qquad (2.14)$$

Euler's equations can be rewritten as

$$\frac{D\boldsymbol{u}}{Dt} = -\frac{1}{\rho}\nabla p + \boldsymbol{g}, \qquad (2.15)$$
$$\nabla \cdot \boldsymbol{u} = 0.$$

In 1822 [12] Augustin-Louis Cauchy intruduced the *stress tensor* σ_{ij}, to parametrize the forces acting on a fluid element. In figure (2.8) the stress tensor, and how it acts on a fluid element, are illustrated.

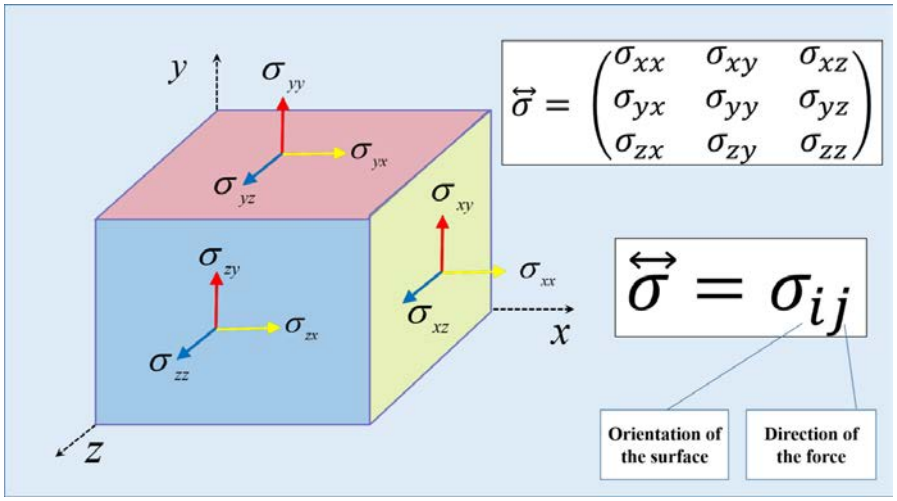

Figure 2.8: *The components of the stress tensor [16].*

Here it is necessary to briefly introduce what is known as Einstein notation or the Einstein summation convention (Cauchy, having been dead for some

time when Einstein lived, obviously used a different formalism). It is a simple trick, to save the number of symbols necessary to express summations, and in this context, it means that repeated indices should be summed over. σ_{ij} is the j-component of stress on a surface element δS, which has a normal $\boldsymbol{n}$ pointing in the i-direction. With the stress tensor Cauchy was able to formulate what is known as the *Cauchy equation*:

$$\rho \frac{Du_i}{Dt} = \frac{\partial \sigma_{ij}}{\partial x_j} + \rho g_i. \tag{2.16}$$

For an incompressible, Newtonian viscous fluid we have

$$\sigma_{ij} = -p\delta_{ij} + \mu \left(\frac{\partial u_j}{\partial x_i} + \frac{\partial u_i}{\partial x_j} \right). \tag{2.17}$$

The stress tensor is symmetric [12], $\sigma_{ij} = \sigma_{ji}$, this reduces the unique components of equations (2.17), from nine, to six. Inserting equations (2.17) into equations (2.16) yields the Navier-Stokes equations for incompressible, Newtonian viscous fluids[2]:

$$\rho \frac{\partial \boldsymbol{u}}{\partial t} + \rho(\boldsymbol{u} \cdot \nabla)\boldsymbol{u} = -\nabla p + \mu \nabla^2 \boldsymbol{u} + \rho \boldsymbol{g}. \tag{2.18}$$

The left hand side represents *inertial terms* and the right hand side *forces*. The first term on the left represents the unsteady acceleration of the fluid element; the second describes convective acceleration. The first term on the right represents forces from pressure gradients. The second term represents viscous force due to shear stress, and the third gravitation. The equations are named after Claude-Louis Navier and George Gabriel Stokes. They were derived independently, by the two, in the first half of the nineteenth century. The equations are considered to be a cornerstone of modern fluid dynamics.

Possessing the solutions for the Navier-Stokes equations for a given flow situation would somewhat represent the ultimate goal for that we are trying to do. When it comes to flow in porous media, we are usually very far from that goal. Not only are we unable to solve the equations, but we are also struggling to formulate them fully. The equations must contain all relevant information about the porous media, the involved fluids, all interactions, as well as boundary and initial conditions. The real dynamics are just too complicated and involved, for us to properly set up all the terms. Even if we could, the equations would be unresolvable, also with numerical methods, as they would require astronomical amounts of iterations. Therefore, we turn to another form of analysis and attempt to formulate phenomenological, macroscopic descriptions.

[2]There are some steps missing in arriving at this result. The six unique components of equations (2.17) should be written out and inserted duly into the three components of equations (2.16). For a more thorough derivation I refer to the text book reference [12].

2.3.7 Darcy's law

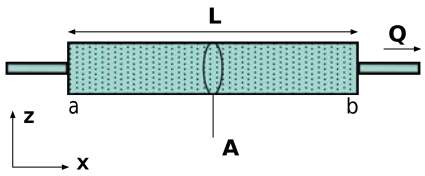

Figure 2.9: *Definitions for Darcy's law [17].*

Henry Darcy was involved in the public waterworks of the city of Dijon in the 1850s. To filter the water before distribution, he fed it through a porous medium. In figure (2.9) such a filter is illustrated. He experimentally established a proportionality, between the flow rate and the pressure gradient, and introduced the concept of *permeability*, for single-phase flow through a porous medium. Permeability, often labeled k with units [Darcy] or [m^2], is a geometric property of a porous medium. It is a number representing a fluid's ability to flow through the medium. Typically, narrow passages make it more difficult for the fluid to flow, yielding a low permeability, whereas wider passages facilitate flow and contribute to increased permeability. The relation is formulated in what is known as Darcy's law:

$$Q = -\frac{kA(p_b - p_a - \rho hg)}{\mu L}, \tag{2.19}$$

where Q is the volumetric flow rate, per unit time, k the permeability, p the pressure, A the cross-section area, L the sample length, h the vertical component of L, and ρg is the contribution from gravity. In figure (2.9) the flow is horizontal, the ρhg term can be ignored. By dividing with the area on both sides, and taking the limit as $L \to 0$, we get

$$\boldsymbol{q} = -\frac{k}{\mu}(\nabla p - \rho \boldsymbol{g}), \tag{2.20}$$

where $\boldsymbol{q}$ is the flux, with magnitude and direction, also defined as the *filtration-* or *Darcy-velocity*. The Darcy velocity is not the average velocity of the flow in the pore spaces, u, but proportional via the relation

$$u = \frac{Q}{\phi A} \quad \Rightarrow \quad q = \phi u, \tag{2.21}$$

where ϕ is the porosity.

2.3.8 Stable and unstable displacement

One of the methods to analyze and categorize two-phase flow is to look at the geometric properties of the pattern formations. One of the characteristics of such a property is the shape of the *front* that the invading fluid forms against the defending. If we start from the setting of the disk-shaped Hele-Shaw cell, with the invading fluid injected from the center, and the circumference open to the atmosphere, we have a situation as illustrated in figure (2.10). In the case of stable displacement, the front is *narrow*, whereas, in the case of unstable displacement, the front is *wide*. In this case, this is still a purely qualitative distinction. Idealized unstable displacement would be the invading fluid going in a straight line from the center to the edge, and the stable displacement would be the invading fluid growing out in a perfect disk from the center. To distinguish between the two, we parametrize the front and look at such quantities as the fractal dimension (treated in section 2.3.10), and define a domain for the two regimes. In the case of unstable displacement, the invading fluid moves in narrower passages through the defending fluid. This is called *fingering*.

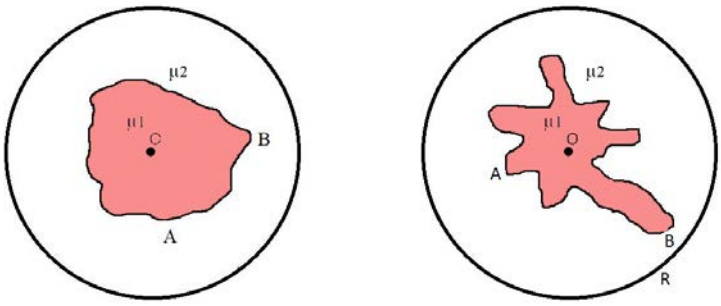

Figure 2.10: *A Hele-Shaw is prepared fully saturated with one fluid, here white. Another fluid, here colored, is injected through an inlet at the center. Stable displacement on the left and unstable displacement on the right.*

2.3.9 Laminar and turbulent flow - the Reynolds number

In 1883 Osborne Reynolds demonstrated the transition from laminar to turbulent flow by an experiment, in which he injected dyed water into the center of the flow in a large tube [18]. As the tube was made of glass, the streamlines could be seen as streaks of dye. At low velocities, the dye remained in straight lines, near the center of the tube. As he increased the velocity, there occurred a transition, where the dye lines broke up and clouded the water. To quantify these regimes he introduced what has become known as the *Reynolds number*,

$$Re = \frac{inertial\ forces}{viscous\ forces} = \frac{\rho u L}{\mu} = \frac{uL}{\nu}, \tag{2.22}$$

where u is the flow velocity and L is the characteristic linear dimension. Re is

a dimensionless number. High Reynolds numbers are associated with turbulent flow and low Reynolds numbers with laminar flow.

2.3.10 Fractal dimensions and box counting

Fractals are shapes that repeat themselves as dimensions are scaled up or down. Many phenomena in nature show fractal geometry, such as snowflakes or the shape of coastlines where land meets sea [19].

It has been shown experimentally, that the patterns formed by both viscous and capillary fingering are fractal [20–22]. One of the parameters we can use to characterize such formations is the fractal dimension. Among others, we use a box-counting method to determine the fractal dimensions of flow patterns. Different regimes give rise to different flow patterns. Figure (2.11) illustrates this method.

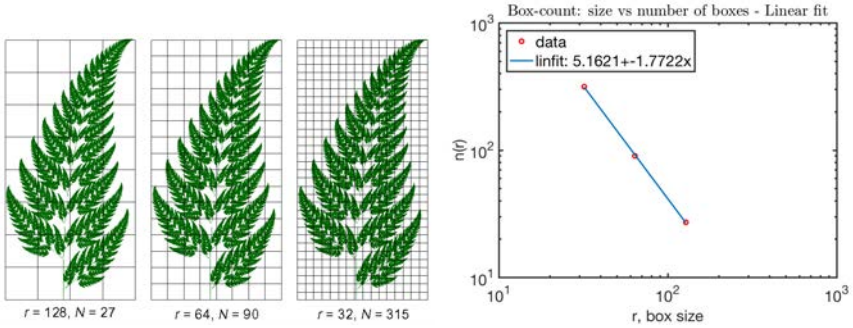

Figure 2.11: *Example of how the box-counting method can be used to determine the fractal dimension of a pattern. The box-counting routine counts how many boxes the pattern occupies. r is the length of one side of the box in pixels, N is the number of boxes occupied by the pattern. The plot is a log-log plot of N versus r. The fractal dimension D is evaluated as the negative slope of the fitted line, in this case $D = 1.77$.*

The method can be applied in the same manner to a 3D volume, by merely replacing the 2D-square boxes with cubical 3D ones [23]. Typically, a pattern that covers a more significant fraction of the area, with more or thicker fingers, will give rise to a higher fractal dimension.

2.3.11 Diffusion-Limited Aggregation and Invasion Percolation

Flow in porous media generates invasion patterns that can be analysed and understood in light of various numerical simulation schemes. Two of the most commonly referred to are presented here.

In 1981 Witten et al. published a new theory for pattern formation through aggregation and introduced the concept of *diffusion-limited aggregation* (DLA) [24]. The approach led to the development of a simulation scheme. One interpretation of this algorithm is to imagine a circular 2D-lattice. In the

initiation state every site is empty, symbolized by the value zero. In the center site a particle is placed, symbolized by a one. One by one random walkers are then sent in from a random site on the edge. If the walker comes to a site adjacent to the particle it stops, and also assumes the value of one, thus a cluster grows. However, if it wanders out of the circle without hitting the cluster it is discarded. The algorithm stops when the cluster reaches the edge at any point. Figure (2.12) shows a typical cluster formed with such an algorithm.

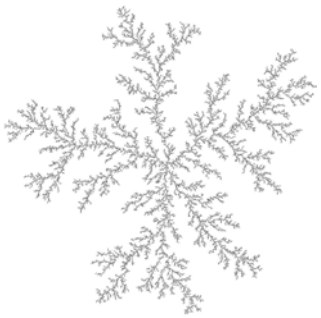

Figure 2.12: *From a 2006 publication by Paul Bourke, showing a traditional 2D-DLA structure, containing 30.000 particles [25]. This pattern is associated with fast flows in porous media and relates to so called viscous fingering, more on this in the coming sections.*

Slow drainage flows in porous media have convincingly been put into context with a simulation framework called *Invasion Percolation* (IP). Wilkinson and Willemsen introduced the concept in a 1983 paper [26]. Invasion percolation algorithms are considered to be one of the simplest ways to simulate displacement processes in porous media.

One way to configure the algorithm would be to generate an idealized porous medium as sites in a 2D-table of size L_xxL_y, where the sites are the pores of the medium. The table is initiated as fully saturated with fluid one, thus every site has the value one. Another equally sized table is generated. The sites here are assigned a random number in an interval signifying the range of capillary pressure-thresholds, p_c, for each site, and thus represents the geometry of the porous medium.

For comparisons with a physical system, where the pores are accessed by pore throats, we can use equation (2.10) to describe this threshold by

$$p_c = \frac{2\gamma}{r_m}, \tag{2.23}$$

where γ is the surface tension at the fluid-fluid interface, and r_m is the radius of the throat, here with the assumption that every throat is a circular tube. The range of random numbers thus reflect a range of pore throat sizes.

The flow is initiated by replacing the voids in the top row with fluid 2, in the form of twos. The system can be configured with periodic boundary conditions, but let us for the sake of simplicity say that the system is closed at the sides, and that displaced fluid can exit at the bottom. Fluid 2 can now displace

fluid 1 downwards through the throats. The actual flow process is conducted by looking at the sites along the front that are occupied by fluid 1. The site with the lowest associated capillary pressure-threshold is invaded, simply by replacing the one with a two . This step is then repeated, until the flow reaches the bottom row, and we say that fluid 2 is percolating. An additional rule that usually is applied is trapping. This rule requires that clusters of fluid 1 that have been completely surrounded by fluid 2, no longer can be invaded. Figure (2.13) shows in image generated with a similar algorithm (from a course I did on computational physics, in the fall of 2018).

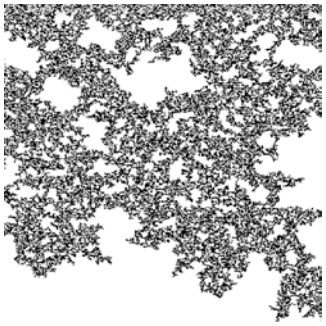

Figure 2.13: *Invasion percolation simulation with two phases. Here as a result of a slightly different algorithm, the so called Hoshen-Kopelman algorithm, but the pattern is quite similar to what one should expect form the described procedure. The figure shows a plot of the two phases as the black fluid has percolated from the top down to the bottom. This pattern is associated with slow flows in porous media and relates to so called capillary fingering, more on this in the coming sections.*

This description is perhaps the simplest possible version of invasion percolation. The code can be expanded to allow for configuration of different capillary pressure-thresholds for each neighbor-neighbor front, the porous media can be given geometric shapes by configuring it into the tables, and potentials such as gravity can be added through appropriate rules.

To further put the findings from [26] into context with the matter of this thesis i include some relations from percolation theory[3], here with symbols as presented in the Wilkinson and Willemsen paper.

The volume fraction of the invading fluid, S_I, can on average be expressed as

$$S_I = AL^{-\alpha}, \tag{2.24}$$

where L is the system size, and the exponent $\alpha = \beta/\nu$. β is the order parameter exponent and ν the correlation length exponent. The factor A is not defined, but analysis of the units dictates that it must have units $[\mathrm{m}^\alpha]$, further it becomes reasonable that it should represent the scaling of the system size with the characteristic length scale, a, on the form $A = a^\alpha$. In terms of the number of sites, N_I occupied by the invading fluid this translates to

[3]Making a more thorough presentation of percolation theory is outside the scope of this thesis, I, therefore, refer to the Wilkinson and Willemsen paper[26] and Broadbent and Hammersley's 1957 publication [27], which marked the advent of percolation theory.

$$N_I = BL^{\phi}, \tag{2.25}$$

where ϕ is the fractal dimension. The identification with the exponents is given by

$$\alpha = \frac{\beta}{\nu} \quad \text{and} \quad \phi = \frac{\Delta}{\nu}, \tag{2.26}$$

where Δ is the gap exponent. Further we have the corresponding relations

$$\alpha + \phi = d \quad \text{and} \quad \Delta + \beta = d\nu \tag{2.27}$$

where d is the space dimension.

2.3.12 Viscous and capillary forces - the capillary number

To characterize flow in porous media, we can look at the ratio between capillary and viscous forces, labeled the *capillary number*. It is defined in various manners for corresponding situations. Here is one way of defining this quantity. By starting from Darcy's law and assuming the Darcy velocity as the actual flow velocity at the pore scale, a, and consider that the permeability scales as $k \sim a^2$, we can write

$$u \approx \frac{\Delta p_\mu a^2}{\mu a} \quad \Rightarrow \quad \Delta p_\mu = \frac{u\mu}{a}, \tag{2.28}$$

where u is the velocity, μ is the dynamic viscosity, a the pore size and Δp_μ the viscous pressure drop along the pore.

The capillary pressure is affected by the geometry of a given porous medium and is a measure of the pressure difference between the wetting and non-wetting phases. From the Young-Laplace equation, it scales with the pore geometry as

$$\Delta p_\gamma = \frac{\gamma}{a} \tag{2.29}$$

If we look at the ratio between viscous pressure Δp_μ and capillary pressure Δp_γ, we get the capillary number

$$Ca = \frac{\textit{viscous forces}}{\textit{capillary forces}} = \frac{\Delta p_\mu}{\Delta p_\gamma} = \frac{u\mu}{\gamma} \tag{2.30}$$

This derivation of the capillary number is not necessarily appropriate to a given case, alternate capillary numbers are used. For instance the permeability can be taken into account, or Ca can be scaled with the system size.

2.3.13 Flow regimes - the competiton of forces

The study of the macroscopic pattern formations that result from the interplay between forces in two-phase flow, has led us to the formulation of what is known

as *flow regimes* [20]. In general, we consider a case where one fluid phase is displacing another. In reality there can be several driving forces, and there are cases where it is not necessarily clear which phase is defending and which is invading. For instance, if one prepares a sample in such a way that the lower half is fully saturated by a denser fluid and the higher by a less dense, and one then flips the sample - in this case they are both invading and defending, as the less dense liquid is driven up, and the denser is driven down. Clearly, gravity is present here, but there are also viscous and capillary forces, as well as potential temperature gradients, and so on. These types of ambiguities are part of why it is always necessary to be very precise with definitions and descriptions, while one at the same time maintains an understanding that the categories of flow regimes do not always represent absolute definitions, but rather degrees of tendencies - especially in real-life 3D-situations.

When the displacement front is narrow and stable, the flow is easily characterized and leads to one phase displacing the other. What is more interesting, but also far more complex, is when there are pattern formation. The flow branches out in fingers and leaves behind abandoned clusters of defending fluid.

Through experiments conducted with a quasi 2D-matrix in a horizontal Hele-Shaw cell and theoretical and numerical frameworks, a description of the main tendencies of the dynamics of viscous and capillary forces has emerged. Roughly we can say that for high velocity and high viscosity, the viscous effects are important. For low velocity and low viscosity, the capillary forces are important. However, experiments show that the two are both present in any physical flow in a porous medium [28].

Viscous fingering is associated with high Darcy velocities and a steep viscosity contrast between the fluids, and occurs when a less viscous fluid displaces a more viscous one [22]. An intuitive understanding can be gained from regarding the illustration of unstable displacement, on the right, in figure (2.10). If we take the colored liquid to be less viscous, we can make the argument that the pressure difference between the injected fluid and the atmosphere will be the approximately the same, anywhere within the fluid. As the distance from point B to the rim of the disk, is shorter than from point A, the pressure gradient will be at its steepest in a straight line from B to the outside. Thus this will be the likely path of the invasion. In a porous medium, we can make the added assumption, that the viscous fingers will favor the wider passages, where the permeability is highest.

As the Helle-Shaw cell in itself can be considered a porous medium, with an associated permeability and constriction of the flow, looking at two-phase flow in the cell itself is considered a relevant starting point. The theoretical framework for viscous fingering in a Hele-Shaw cell has among others been developed by Saffman and Taylor [29] and Chuoke, van Meurs and van der Poel [30]. In a benchmark 1958 publication, Saffman and Taylor studied finger formations in two-phase flow in a horizontal Hele-Shaw cell without a porous medium. Their findings led to a formulation that perturbations to a flat fluid-fluid interface

above a critical wavelength[4] would lead to the formation of viscous fingering. The pertubation-wavelength, λ, is described by

$$\lambda > \lambda_c = 2\pi \left(\frac{\gamma k}{(\mu_2 - \mu_1)(\bar{U} - U_c)} \right)^{1/2} \tag{2.31}$$

where λ_c is the critical wavelength, γ is the surface tension, $k = a^2/12$ is the permeability[5], with a as the separation between the cell plates, μ_1 and μ_2 are the viscosities of the invading and defending fluids, U_c is the critical velocity, and $\bar{U}$ is a constant injection rate.

When the cell is horizontal and $U_c = 0$ the critical wavelength is described by the *Saffmann-Taylor instability*,

$$\lambda_c = 2\pi \left(\frac{\gamma k}{(\mu_2 - \mu_1)\bar{U}} \right)^{1/2}, \tag{2.32}$$

The experiments were conducted with a cell that was sealed at two of the sides. One fluid was injected into another, from one of the open ends. They found that single viscous finger developed with a width that decreased to half the channel width as the capillary number, $Ca = u\mu/\gamma$, increases above 0.04. u is the fingertip velocity, μ, is the viscosity of the high viscosity fluid, and γ is the interfacial tension [29].

In 1984 Paterson et al. explored the similarities in the pattern formations described by DLA and those formed by viscous fingering in two-phase flow in porous media [31]. The relation is strengthened by a similarity in the theoretical framework of the two. In the case of viscous fingering we have, from Darcy's law, that the flow velocity in the porous medium scales as $u \sim \frac{k}{\mu}\nabla p$. We can require $\nabla \cdot \boldsymbol{u} = 0$ and when viscous forces dominate the pressure in the invading fluid equalizes. In equilibrium we then have the Laplace equation $\nabla^2 p = 0$. Similarly diffusion limited aggregation has a flux, J, described by Fick's law, $J = -D\nabla C$, where D is the diffusion coefficient and C is the concentration. In equilibrium we have $\frac{\partial C}{\partial t} = D\nabla^2 C = 0$, and thus the equivalent Laplace equation $\nabla^2 C = 0$. In a porous medium the noise in the modeling comes from the pore throat-distribution and in DLA it is generated by the inherent randomness of the random walker.

Figure (2.14) is from a 1985 experiment by Måløy et al. [22], where patterns formed with a fractal dimension of $D = 1.62 \pm 0.04$, which was found to be

[4]The wavelength describe the distance, across the front, from one minimum or maximum to the corresponding next minimum or maximum. This concept is rather involved and comes under what is known as *linear stability analysis*, for a thorough explanation I refer to the textbook reference [3].

[5]For a derivation of the permeability in the Hele-Shaw cell, I refer to the textbook reference [19].

consistent for theoretical predictions from diffusion-limited aggregation clusters [24].

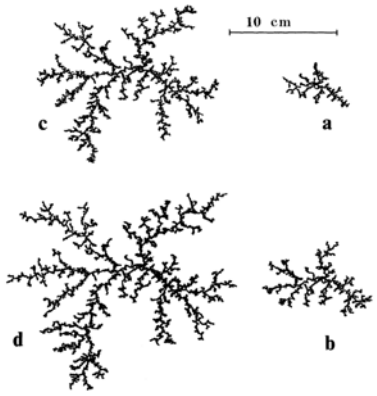

Figure 2.14: *Characteristic viscous fingers. Air is injected from the center into a circular, horizontal Hele-Shaw cell, prepared with a monolayer of glass beads and saturated with epoxy. [22]. The images a-c are high contrast renderings from photographies, taken at different times, from 2 s to 19.1 s into the experiment.*

Capillary fingering is characterized through a different line of reasoning, but general traits are that the Darcy velocity and the capillary number both are very low, and that the capillary forces strongly dominate over the viscous ones [20]. The capillary forces are determined by the wetting properties and surface tensions given by the fluids, the solid and by the pore geometry. The capillary action will favor the advance of the wetting fluid at an interface, with the capillary action being the strongest in the narrowest passages. However, the observed dynamics is that the wider passages are invaded by the non-wetting phase, as the opposing force due to capillary action is weakest here. The displaced wetting fluid then pushes the interfaces back in the surrounding menisci [32, 33].

Figure (2.15) is from an experiment expanding on the transition from capillary to viscous fingering, as the capillary number is tuned, in a drainage experiment (see the figure caption for further clarification) [34].

In this particular case, the capillary number is given as

$$Ca = \frac{\mu_w v_f a^2}{\gamma \kappa}, \tag{2.33}$$

with the following definitions: μ_w is the dynamic viscosity of the wetting fluid, v_f is the Darcy velocity or specific discharge, a is the characteristic pore size, γ is the interface tension, and κ is the intrinsic permeability of the homogeneous and isotropic porous medium.

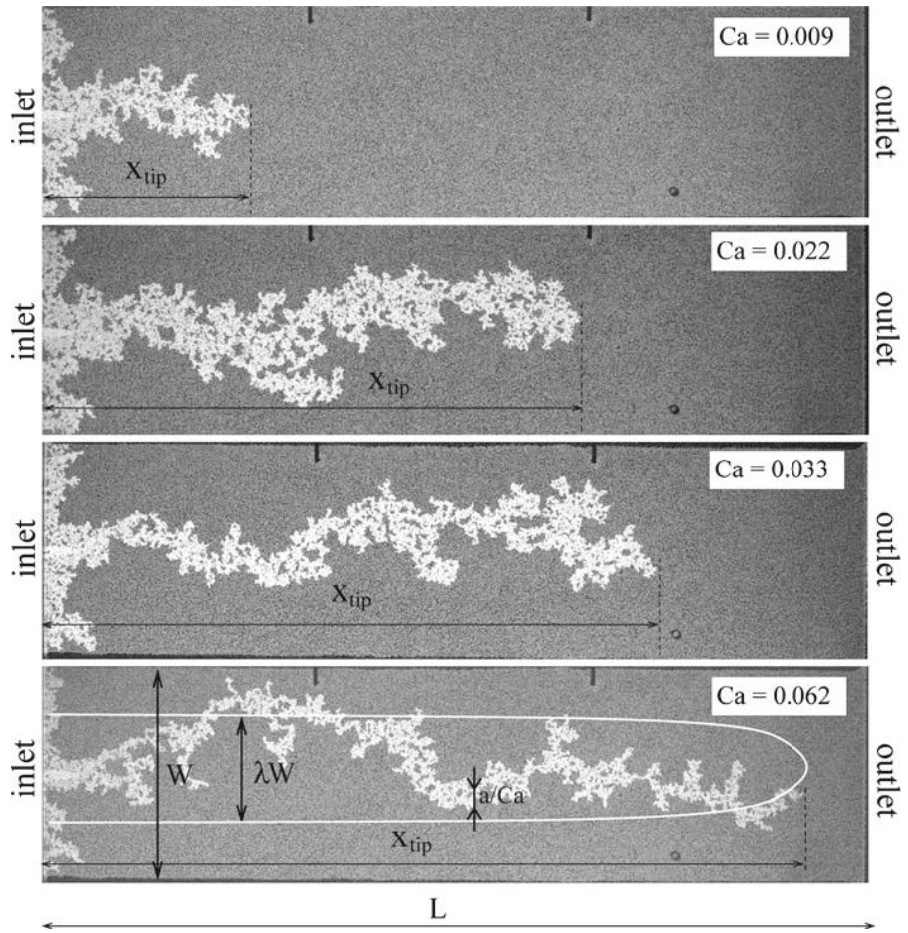

Figure 2.15: *Image from an experiment, conducted in the what was to become PoreLab, in 2010. This particular image is highly familiar to all of us in the community around PoreLab, as it has occurred in several articles. I believe I have found the first publication it featured in [34]. The experiments were conducted with a horizontal Hele-Shaw cell, sealed at the long sides, prepared with glass beads and saturated with a dyed water-glycerol solution. The liquid was withdrawn from the right, and air entered through the inlet on the left. The withdrawal rate was altered, from a slow rate for the top image, to faster towards the bottom. We see several flow regimes, developing from typical capillary fingering with a low capillary number at the top, to viscous fingering at a higher capillary number at the bottom.*

Here it should be stressed that the elaboration of capillary vs viscous fingering in [34] is quite involved. It is quite possible to achieve a qualitative understanding of the two regimes, from just looking at the pictures, but at the same time, it is also apparent that the two are highly connected phenomena. The viscous fingering drives the front towards the outlet, as the shorter distance, from the most advanced point of the front, creates a steeper pressure gradient than elsewhere. Capillary fingering will evolve more randomly, as it is the pore-

throat distribution that dictates which pores get invaded when capillary forces dominate. Rather than strictly saying that the one is a general example of capillary or viscous fingering, the article expands on how the set-up and the tunable parameters allowed for a range of fingering regimes, spanned by the two types at the idealized, theoretical extremes.

Løvoll et al. [34] defines several characteristic length scales. The cell has a length L, and a width W, and the pores scale with the diameter, a, of the beads used to make the porous medium. The fingers penetrate the cell to a depth x_{tip} and globally they occupy a width λW. Further it is found that at intermediate capillary numbers, the viscous and capillary forces dominate on different length scales. At the pore scale, capillary forces dominate and the local invasion structure assumes the form of capillary fingering. At larger scales, the viscous forces are more prominent and the structure resembles more the morphology of viscous fingering. The crossover length-scale between these two regimes, l_c, is found to scale as $l_c \propto a/Ca$, further it is deduced that the local width of the finger, w also scales as this lenght scale, $w = a/Ca$.

In a more recent study Moura et al. studies how the geometry of the porous media affects the dynamics of the flow, through experiments and simulations [35]. The experimental set-up is a rectangular, horizontal Hele-Shaw cell with localized glass beads. The cell is saturated with liquid and is open to the atmosphere in one of the short ends, the long sides are sealed, the liquid is withdrawn, from the other short end, and air is pulled into the matrix. The pressure is monitored at the outlet and correlated with images of the state of the drainage invasion pattern. Through image analysis the pressure-saturation curve is then established. Figure (2.16) shows an invasion pattern from one of the experiments.

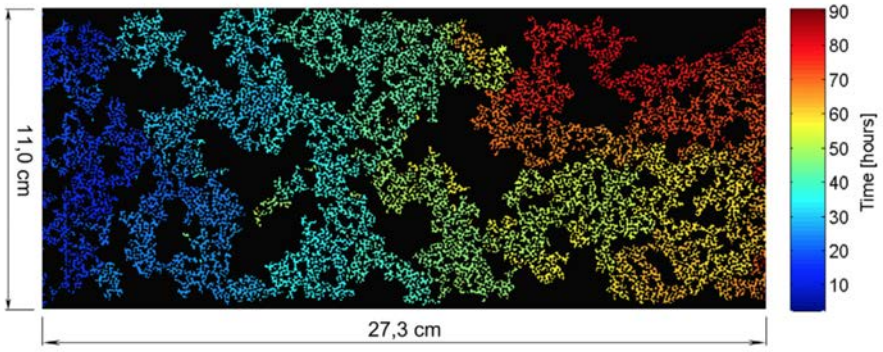

Figure 2.16: *Image from Moura et al. [35]. The figure shows a spatiotemporal map of the drainage invasion, coming in from the left.*

The study seeks to establish how the size and shape of the system affects the pressure-saturation curves. Figure (2.17) shows a measured curve from one of the experiments.

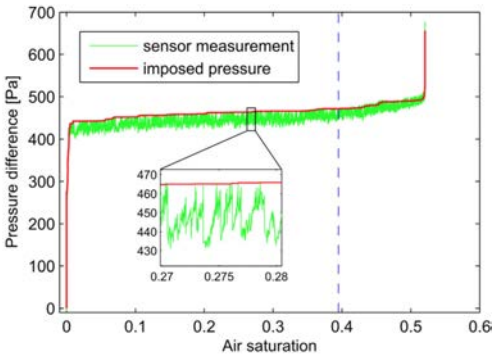

Figure 2.17: *Experimental pressure-saturation from [35]. The dashed blue line indicates the saturation at which the air phase first percolates through the model, reaching the filter at the outlet.*

Further the images are analysed to determine the geometric configuration of the beads in the matrix, thus a connectivity map can be established, with an associated capillary pressure thresholds distribution.

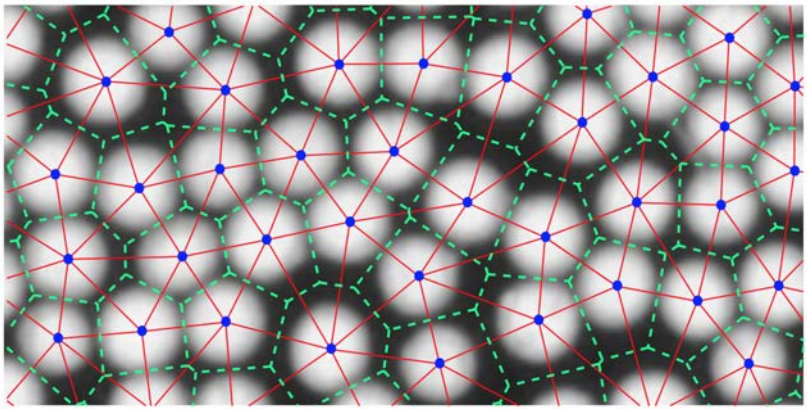

Figure 5. Pore-scale analysis used in the experimental determination of the capillary pressure thresholds distribution. Blue dots indicate the center of the beads, solid red lines show the Delaunay triangulation, and the dashed green lines are the Voronoi lattice (dual graph to the Delaunay triangulation). The vertices of the Voronoi lattice mark the centers of the pores and the points at which the lines from the Delaunay triangulation and Voronoi lattice intersect are the centers of the pore-throats. The bead diameter is ~1 mm.

Figure 2.18: *Image from Moura et al. [35]. The figure caption is also included for clarity. The image is a close up of processed photo from the experiments.*

Through comparisons with IP-simulations with configured capillary threshold distributions derived from the experiments, a model for the pressure-saturation relationship is established. Moura et al. finds that this relationship depends on the system size and aspect ratio, resulting in a simplified model, valid for systems that are large enough such that the invasion is not influenced by boundary effects. The model describes that most of the invasion happens at a nearly constant pressure, which is a function of the connectivity and the pore-throat size distribution.

2.3.14 Fluid transport dynamics - Haines jumps and thin film flows

Not only are the pattern formations observed in flow in porous media complex, the underlying mechanisms and dynamics are also equally so. In two-phase flow one fluid does not simply just push the other out in a linear, orderly fashion. In most cases there are actually several types of transport mechanisms going on, at the same time.

One mechanism, describing events of rapid motion and dramatic events is what is now referred to as *Haines jumps*. The phenomena can qualitatively be understood as a build up of pressure in the invading fluid in a pore, in such a manner that it at some point overcomes a critical threshold, and burst through the meniscus in the largest available throat, displacing the defending fluid, and invading a new pore. The displaced fluid then pushes back the menisci in the surrounding pore throats. This behaviour was first described by William B. Haines in 1930 [36], and since it has been studied in a number of publications. Figure (2.19) from Måløy et al. [33], illustrates such a burst event.

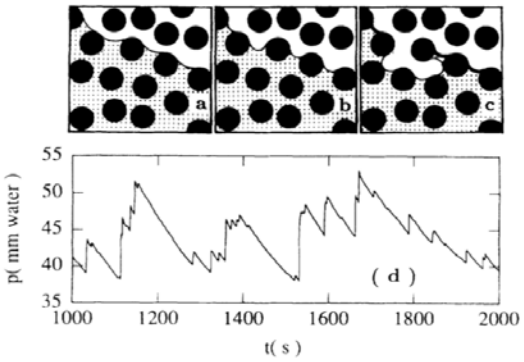

FIG. 1. (a)–(c) Invasion of air (white) into a two-dimensional porous medium filled with water. As water is extracted, the interface moves into narrower parts of the throats. During a burst new pores are invaded and the interface adjusts everywhere to the lower capillary pressure. The heavy black lines show the redistributed volume. (d) Pressure in the water during drainage as a function of time.

Figure 2.19: *Image taken from [33] with the original caption text. The experiments were slow drainage in a 2D-Hele-Shaw cell with a syntetic porous medium made of 1 mm glass beads. The sample was saturated with water that was then withdrawn, dragging air into the matrix. The invasion events are directly linked with characteristic sharp peaks in pressure measurements.*

The publication describes events where bursts typically span over a number of pores. Through comparative IP an exponential pressure jump size distribution is observed. The survey is followed up by Furuberg et al. in [32], where the burst size distribution, $N(s)$ is written on the form

$$N(s) \propto s^{-\tau'} f(s/s^*), \tag{2.34}$$

where s is the burst size, s^* is the typical largest burst size, τ' is the burst size distribution exponent (which is a function of the geometry of the invasion pattern), and f is a crossover function for the pressure jump distribution. The largest typical cluster, s^*, is found to scale as

$$s^* \propto \left(\kappa L^{D_f}\right)^{\nu D/(1+\nu D)}, \tag{2.35}$$

where κ is the volume capacitance, L^{D_f} describes the front length of the invaded structures, ν is the percolation correlation length scaling exponent, and D is the fractal dimension of the invasion pattern.

In section (2.3.17) a study [37] of Haines jumps in 3D is briefly presented.

Thin film flows is at the opposite end of the drama-scale of Haines jumps. The described dynamics are slow and subtle, and is actually often discounted, as its effects only can be observed over some time. In two-phase flow in porous media, thin film flow is a transport of fluid in a thin coating and over capillary bridges of one fluid, through pores that are apparently saturated by the other.

In a 2008 publication Arshad Kudrolli [38] explores the cohesive effect liquid can have on a granular material, such as sand when it is wet. X-ray microtomography is used to look at capillary bridges formed between beads of glass that have been saturated by liquid, as the bulk of the liquid has been drained away. Figure (2.20) is from the publication.

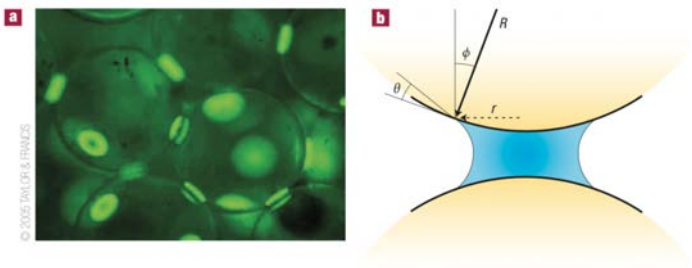

Figure 1 Liquid bridges form at the point of contact between grains, as a result of surface tension. **a**, Fluorescence microscopy image of liquid bridges between 375-μm-diameter glass beads[5]. **b**, Schematic of a liquid bridge (blue) between spherical surfaces (yellow). θ is the liquid–solid contact angle, ϕ is the half-filling angle, defined as $\phi = \tan^{-1}(r/R)$, where r is the radius of the liquid bridge, and R is the radius of the grain.

Figure 2.20: *From [38] with the original caption text. The capillary bridges observed between grains also play an important role in the mechanical properties of granular systems. They are responsible for the structural stability of sandcastles, for example.*

Aursjø et al. studied film flow in a simultaneous flow of two viscous incompressible fluids through a quasi 2D-porous medium [39]. The immiscible fluids were a water-glycerol mix and rapeseed oil, of comparable viscosities. the porous matrix is initially filled with the water-glycerol solution dyed with nigrosine. The experiment is started by injecting the oil and the water-glycerol solution simultaneously from every other one of inlet points on the left side of the model. The rapeseed oil enters the porous matrix and form distinct fingers. The water-glycerol phase is seemingly fragmented into disconnected clusters. These clusters are generally left in a fixed configuration behind the front. As the water-glycerol solution is constantly injected alongside the rapeseed oil, this suggests that the main fluid transport of water-glycerol solution occurs as film flow, in regions where a fluid phase is seemingly disconnected.

Figure (2.21) and shows how the flow reaches a steady state regime, where the transport of the dark water-glycerol solution is mainly dominated by film flow.

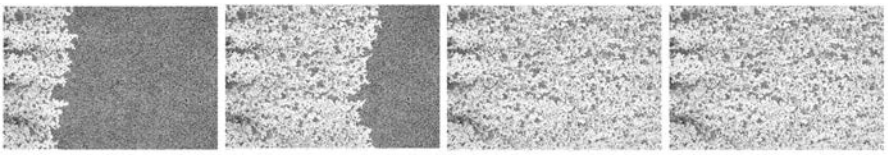

FIGURE 2 | For Q_{tot} = 0.3 ml/min and F_{oil} = 1/2, the flow structure is shown at four different times. The flow direction is from left to right. The images are ordered, from the top, by increasing time. The images are respectively captured at 68, 142, 228, and 330 min into the experiment. The two lower images show flow patterns, at steady state, with a large separtation in time.

Figure 2.21: *Picture from [39] with the original caption text (the images have been changed from a vertical alignment, to better fit on the page).*

Aursjø et al. [39] further concludes that the observed behavior is quite different from that observed in systems with large viscosity differences between the two fluids, and where compressibility plays an important part of the process.

2.3.15 The effects of gravity - the Bond number and the Rayleigh-Taylor instability

When we have two phases in a vertical tube, such as described in the section on capillary pressure, gravity comes into play. The bond number or Eötvös number, after Wilfrid Noel Bond and Loránd Eötvös, is a dimensionless number that measures the ratio of gravitational to capillary forces, quantified by

$$Bo = Eo = \frac{gravitational\ forces}{capillary\ forces} = \frac{\Delta\rho g L^2}{\gamma}, \tag{2.36}$$

where $\Delta\rho$ is the difference in density between the two phases, g the gravitational acceleration, L the characteristic length scale (for instance the radius of curvature for the fluid-fluid interface), and γ the surface tension. High Bond

numbers signify that gravitational force dominates, whereas a low Bond number means that surface tension effects are more important.

To parametrize the combined effects of viscous, capillary and gravitational forces several modified Bond numbers have been proposed [40], such as

$$Bo^* = Bo - Ca \quad \text{or} \quad Bo^{**} = \frac{Bo}{Ca} \tag{2.37}$$

When the effects of gravity comes into play linear stability analysis describes another critical behavior (still for two-phase flow in a Hele-Shaw cell without porous media) if the driving velocity $\bar{U}$ vanishes from equation (2.31), the gravitational effects become dominate, and the critical wavelength is described by what is known as the *Rayleigh-Taylor instability*,

$$\lambda_c = 2\pi \left(\frac{\gamma}{(\rho_2 - \rho_1)\hat{g}} \right)^{1/2}, \tag{2.38}$$

where γ is the surface tension, ρ_1 and ρ_2 are the phase densities and $\hat{g}$ is the component of gravity parallel with the flow direction.

2.3.16 Experimental studies of gravitational effects in flow in porous media

In two-phase flow gravity comes into effect when the fluids have different densities and the flow has a vertical component. As this would be the case in almost any natural scenario, it is certainly something to consider. However, as it is very convenient to put a Hele-Shaw cell horizontally, added with the fact that the horizontal case has provided more than ample complexity, this remains a domain where there is still plenty to do. Not to say that the matter has not at all been probed.

Effects from gravity on pattern formation from flow in porous media have also been considered in the context of invasion percolation. IP algorithms are easily adaptable to include the effects of gravity. In figure (2.22) an illustration of how the IP algorithm from section (2.3.11) can be altered to include gravity.

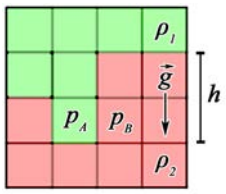

Figure 2.22: *Illustration of IP-algorithm with gravitational effects. The less dense fluid 1 is invading the more dense fluid 2. Each site has already been assigned a random capillary pressure-threshold, p_c, but in addition the invasion now includes gravity, by factoring in the gravitational acceleration, density, and the height of the fluid columns.*

To account for gravitational effects, each defending site along the front, now must have pressure-thresholds that are tuned. This must be done in every step of the iteration. We need only take into account the density difference and the vertical column of liquid spanned by the highest point of the defending fluid and the site in question (disregarding trapped clusters). Compared with site p_A, the site labeled p_B has added pressure because of the column of dense liquid over it. To account for that, the site labeled p_B now gets a new, tuned pressure-threshold

$$p_b = p_c + \Delta\rho g h. \tag{2.39}$$

As before, the defending site along the front, that has the lowest evaluated pressure-threshold, is invaded. The new thresholds are then re-evaluated, and the procedure goes on, until the invading phase reaches the bottom.

In a 1991 paper Birovljev et al. conducted experiments and simulations on 2D gravity invasion percolation in a porous medium [41]. The experiments were slow drainage; air displaced a dyed water-glycerol mix in a tilted flow cell. The bond number, as presented in equation (2.36), was tuned by adjusting the tilting angle. The article presents a theoretical and experimental scaling of the width of the front, w, with the Bond number as $w \sim Bo^{-0.57} \simeq Bo^{-\nu/(1-\nu)}$, where $\nu = 4/3$ is the correlation length exponent. Figure (2.23) shows an image of the flow patterns from the experiments and simulations. Here it is quite apparent how the pattern formed with the higher Bond number leads to a narrower front and a more stable displacement.

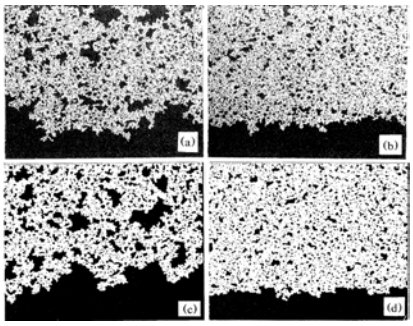

Figure 2.23: *Images from [41]. The two top frames are from the experiment and the two lower are generated from the simulations. In (a) the sample was tilted at $\theta = 3°$ from the horizontal ($Bo_a = 0.005$), in (b) the sample was tilted at $\theta = 11°$ from the horizontal ($Bo_b = 0.018$). In (c) and (d) the bond number was numerically tuned to $Bo_c = 0.001$ and $Bo_d = 0.01$.*

The article concludes that gravity tends to stabilize the drainage front. The comparable fractal dimensions, $D_{exp} = 1.34 \pm 0.04$ and $D_{sim} = 1.39 \pm 0.02$ found for length scales smaller than the front width, strengthens the comparison between experiments and simulations, it is concluded that the process is convincingly quantitatively modeled with an invasion percolation algorithm.

In a comparable study from 1992 Frette et al. studied buoyancy-driven fluid migration in a 3D-porous media [42], both through experiments and simulations. In the experiment, a cell with a porous medium composed of randomly packed

plexiglass cylinders was saturated with index matched dibutyl-phthalate. The Bond number was varied systematically by adjusting the density of the migrating fluid, water mixed with controlled concentrations sucrose (0-60%) and dyed with nigrosine. 2D-projections of the pattern formations were photographed and used for data analysis. The article concludes that the height, h of the invading fluid structure is proportional to the mass, M, of the invading fluid, and that the linear mass density, $S = M/h$, scales with the Bond number as $S \propto |Bo|^{-\alpha}$, where the exponent $\alpha = 0.72 \pm 0.06 = \beta/\nu$. β is the order parameter exponent and ν the correlation length exponent.

The competition between viscous capillary and gravity forces in drainage in a 2D-porous medium was investigated in 2002 by Méheust et al. [40]. A tilted Hele-Shaw cell with adjustable angle was prepared with a porous medium and saturated with a glycerol-water mix. The cell was sealed on the sides. The fluid was withdrawn through an outlet at the lower end of the cell and air was let in through an inlet at the higher end. Analysis of pattern formations made by the invading air led to the conclusion that viscous forces tended to destabilize the displacement front into narrow fingers against the stabilizing effect of gravity. The viscous instability was observed for sufficiently large withdrawal speeds or sufficiently low gravity components. The front width under stable displacement and the threshold for the instability is shown to be controlled by *the dimensionless fluctuation number*, F[6]. The front scales as $w \sim F^{-\nu/(1+\nu)} = [(\gamma/W_t a)(Bo - Ca))]^{-\nu/(1+\nu)}$, where w is the front width, ν the correlation length exponent, γ is the surface tension, W_t is the width of the normalized capillary threshold distribution, a is the typical pore size and Bo and Ca are the Bond and capillary numbers.

This was followed up with a study, using the same experimental set-up, in 2005 by Løvoll et al. [43]. The study further establishes a transition from capillary fingering behavior to viscous fingering behavior where the magnitudes of the viscous-, capillary and gravity forces were comparable.

2.3.17 Making the step from 2D to 3D

So far I have mainly presented studies conducted in 2D-set-ups. Investigations in 3D go back at least as far as those in 2D, and there are many interesting techniques and observations, such as Reynolds demonstration as described in section (2.3.9). Not only are the experimental challenges different when transitioning to 3D, the theory also undergoes changes, and not all derived relations hold up in the transition. Generally increasing the dimensionality will add to the overall complexity, thus making that which is already difficult and confusing, even more so, but there are also cases where a problem is more easily resolved in 3D than 2D. Another benefit one can hope to gain from this transition is new insights and inspirations, that might lead to an entirely different theoretical approach. Here are some of the more specifically relevant studies considered. Here, I will focus mainly on the experimental methods, and on the data that has been generated.

[6] F quantifies the ratio between the average pressure drop over pores and the fluctuations in capillary threshold pressures in the porous medium.

Frette et al. did several experiments and simulations with a 3D-set-up in the 1990s [42, 44, 45]. The studies were all conducted with an index-matched porous medium and defending liquid. The invading liquid was dyed dark, and the resulting pattern was documented as 2D-projections. Figure (2.24) shows an illustration of a set-up, taken from one of the publications [45]

In the context of the work done in this project, it is plain to see how the available technology determined the experimental possibilities. At that point, it would have been possible to pursue a scanner based on the principles this project follows, but the cost and level technical commitment would have been on an entirely different level and were not something that could have been done in the tabletop setting of the flow labs used for these experiments. As they did not have 3D-data they were forced to use a more indirect approach in their analysis. A characteristic length R_A was defined from the projected area A as $\pi R_A^2 = A$. Among the found results was the relation between the cluster mass, M, and the fractal dimension, D, as $M \sim A^{D/2}$.

The obvious drawback of these early 3D-experiments was that they only generated 2D-data, as the set-up did not enable the researchers to see past the dark dye, further inside the samples. An entirely different approach that does offer sight inside is x-ray tomography. In a 2013 publication Berg et al. used high-speed, synchrotron-based x-ray computed micro-tomography to investigate pore scale displacement events in porous rocks, in real time [37]. Figure (2.26) shows their experimental results, 3D-renderings made in Avizo from Thermo Fischer (a software, which is also used in the project treated in this thesis).

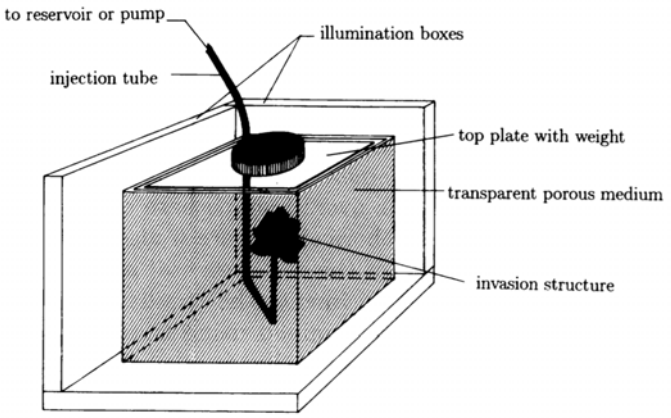

FIG. 1. Experimental setup. A transparent porous medium is held in a glass container. The plate on top of the medium is loaded with a weight to prevent grain movements during the displacement processes. The system is illuminated from below and through two adjacent faces. Two projections of the patterns that are generated when a second fluid is injected are photographed.

Figure 2.24: *Experimental set up and original caption text, from a 1994 paper by Frette et al. [45]*

Digital image processing was at that time very limited by computational speed and image resolution compared with today. In figure (2.25) the processed photos from the experiments are shown.

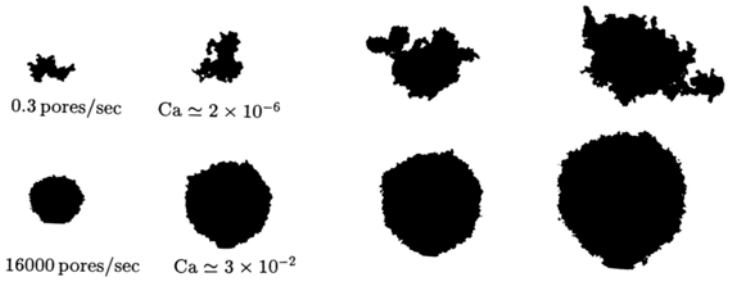

FIG. 3. Fluid-fluid displacement patterns generated in a three-dimensional porous medium. Each line show several stages in one experiment. The injection rates and the values of the capillary number Ca are given in each case. The physical flow rates were 0.004, 1.24, 21, and 210 l/h.

Figure 2.25: *Experimental results and the original caption text, from the same 1994 paper by Frette et al. [45]. To save some space I have cropped out two intermediate lines of pattern formation, from between the two shown.*

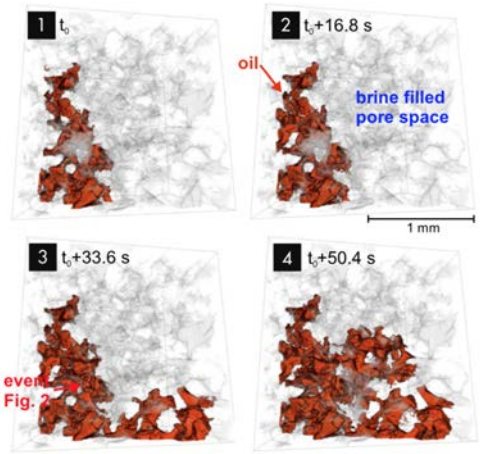

Fig. 1. Sequence of scans during drainage, at time intervals (Δt) of 16.8 s and with a voxel size of 3 μm. The volume change (ΔV) from time steps *3* to *4* was 14 nL.

Figure 2.26: *For clarification, the original figure caption is included. The experiment was conducted at a much smaller spatial scale than the other studies considered here. A 4-mm diameter and 10-mm length cylinder were saturated with water; drainage was conducted by injecting n-decane, from below, at a constant flow rate. The set-up allowed for scans at approximately 17-second intervals. Each scan consisted of* $1.440x896x1.401$ *voxels.*

The article focuses on the dynamics of so-called *Haines jumps*, pressure build-ups and releases caused by burst events as the capillary hold at a pore throat breaks and new pore is suddenly invaded. The article uses this definition: *In a Haines jump, the elastic energy initially contained in the liquid-liquid menisci is converted into kinetic energy, with substantial inertial contributions from the high Reynolds number, and finally dissipated.* They found that Haines jumps typically cascade through 10–20 geometrically defined pores per event, accounting for 64% of the energy dissipation.

Several groups have in recent years developed similar models to the one we

have developed. In particular, we looked closely at a 2018 publication by Dalbe and Juanes [46]. Figure (2.27) shows the illustration of the experimental set-up, from the publication. The experiment focused on the displacement of one fluid by another in a granular pack to uncover relationships between fluid invasion and medium deformation. They also used Avizo to build a 3D-model and visualize the results. Although much inspiration was drawn from this project, our set-up differs in some regards. More on this in chapter (3).

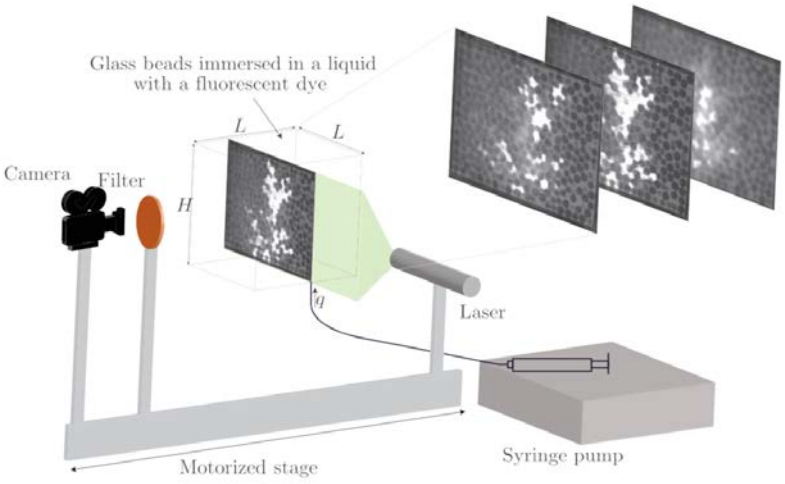

Figure 2.27: *The experimental set-up used by Dalbe and Juanes [46]. The scan was made by index matching a porous medium and two immiscible fluids, dying the fluids with fluorescent molecules and scanning through with a laser sheet. The porous medium consisted of borosilicate beads. The two-phase flow was conducted by saturating the cell with silicone oil and non-wetting, more dense, glycerol from the bottom.*

Figure (2.28) shows some images of the resulting 3D-visualizations from the experiments. Amongst the other results were measured fractal dimensions for the 3D-structures in the range of 2.2-2.8.

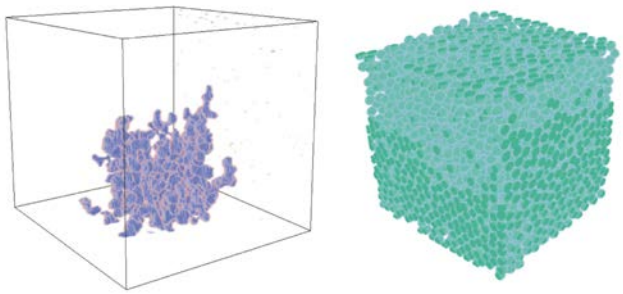

Figure 2.28: *Visualisations of the invasion body and porous medium, from the publication by Dalbe and Juanes [46].*

2.4 Light, fluorescence, geometrical optics and imaging

In this project, light plays a central role, as it is how the sample is probed, and by which the bulk of the data is collected and recorded. The actual experiment should not be affected by light, but the main focus of this project has not been the flow experiment, but rather how to record it meaningfully.

The tools used in the project are commonplace objects in the lab environment. Cameras, lenses, lasers, and filters are all used as a matter of course, and often with fruitful outcomes of high quality. However, much of the key to success and further development of this project depends on pushing the limits of the commonplace and arriving at something highly fine-tuned and well conceived. Light is modeled and understood in several ways, for different applications, in this work several of these approaches have been relevant. The field is one that has many valuable applications in work conducted by Porelab, and I think pursuing excellence in this field can help lift the quality of the group as a whole. Therefore this section has been devoted extra attention.

Light is one of the most studied, discussed, and fascinating phenomena in nature. What we call *light*, is a slice of the spectrum of what is known as *electromagnetic radiation*, with wavelengths from about 400 nm to 700 nm. From a theoretical standpoint, the full spectrum of electromagnetic radiation is one single phenomenon, which can be treated and modeled with the same dynamics. Any given electromagnetic radiation can, in fact, be shifted anywhere in the spectrum, by altering the reference-frame of observation, as Einstein convincingly revealed in the theory of Special Relativity. It is perhaps not correct to say that electromagnetic radiation is poorly understood, but it is indeed a phenomenon that still puzzles, and it is one that we struggle to find one unified description of. Perhaps there are those, that are far immersed in quantum field or string theory, that would disagree, but I for one am still stuck in what is commonly called the *wave particle duality*.

2.4.1 The early theories of light

It seems reasonable to assume that light and our vision have been a subject that has occupied man throughout the entire existence of the species. Archaeologists have uncovered a mirror dating from 1900 BC in Egypt. In *Exodus 38:8*, from about 1200 BC, it is recounted how Bezaleel melts copper mirrors and recasts the metal into basins. It is, however, not until later, from Greek antiquity, that we have specific accounts that expand specifically on theories of the nature of light [47].

Were we, without any prior education on the subject, to speculate on the nature of light and our vision, we would perhaps suppose that our sight was the result active probing of our surroundings, by our eyes, as the sonar of bats. Euclid made the same assumption in his work *Optics* from around 300 BC. Euclid's Optics is perhaps the earliest preserved attempt at a mathematical description of the dynamics of light. The book contains seven postulates, from which fifty-eight propositions are derived. The work is mathematically sound and has been very influential. Amongst others, it includes a formulation of the law of

reflection that is still held to be valid. Apart from his underlying assumption of the probing nature of our eyes, the text offers little in the way of explaining the physical nature of light [48, 49].

That is not to say that there were no theories about the nature of light at that time. Aristotle speculated, more in tune with our modern notions, that the light we perceive with our eyes is indeed not dependent on any active participation from our eyes, but rather something that is there, and that our eyes record. He also speculated that this *something* propagated at infinite velocity, in the sense that the perceived moment in time was shared both at the source and the reception [49].

Light has been a constant subject for philosophers ever since, but a significant shift occurred in the seventeenth century when discoveries were made, and theories were formulated, many of which we still use and hold as valid today.

The art of making lenses as spectacles were blooming, and a Dutch telescope maker named Hans Lippershey made the first telescope in 1608, which Galilei quickly copied [47]. Rene Descartes published *Dioptrique* in 1637, in which the most significant contribution is the law of refraction[7], formulated as

$$\sin\theta_i = n \sin\theta_r, \tag{2.40}$$

where θ_i is the angle of incidence, θ_r the angle of refraction and n the index of refraction. The law is formulated with the assumption that the light goes in our out of air from or to another medium, of refractive index n. To generalize the equation, to interactions between two mediums where neither is air, one can multiply the left-hand side with the refractive index of the other medium. Descartes postulated that light is made up of discrete particles, *corpuscles*, which travel in straight lines, at a finite velocity and possess *impetus* - kinetic energy.

The French mathematician and lawyer Pierre de Fermat (1607-65) was intrigued by the nature of light. In a letter dated January 1, 1662, to Cureau de la Chambre he formulated the earliest known version of what we now call Fermat's principle [51]. The principle can loosely be formulated as: The path taken between two points by a ray of light is the path that can be traversed in the least time. Meaning that, as a beam goes from one medium to another, it chooses a path that is an optimization between the distances traversed and the velocity of propagation in the respective media. More formally it can be put: Rays of light traverse the path of stationary optical length with respect to variations of the path. The idea is both elegant and intriguing, it can be read as a suggestion that the light has some conscious faculty, carrying out

[7]The law of refraction is most commonly called *Snell's law*, after Willebrord Snellius (1580-1626). The oldest known equivalent description was made the by the Persian scientist Ibn Sahl at the Baghdad court in 984, in the manuscript *On Burning Mirrors and Lenses* [50].

deliberations and calculations as it goes, something that Fermat probably did not intend to suggest.

In 1690 Christiaan Huygens published *Treatise on Light*. It contains his famous wave principle, which can be formulated as: *Every point on a wavefront can be viewed as a source of secondary spherical wavelets which spread out in the forward direction at the speed of light*[52]. Huygens also correctly identified that light slows down on entering a more dense medium. His model offered derivations of the laws of reflection and refraction. He also explained double refraction observed in calcite, and he is attributed with the discovery of the property of light called *polarisation* [47].

In 1704, Newton published *Opticks: or, A Treatise of the Reflexions, Refractions, Inflexions, and colours of Light*. Newton carried out a large number of experiments with light. The most significant discovery concerning light attributed to Newton is the spectrum contained in white light. We all are familiar with the image of the rainbow spectrum emitted as a ray of white light traverses a prism. Newtons explanation of this in the elaboration of what he named *dispersion* remains highly relevant. Dispersion is the dependence of phase velocity upon frequency - light moves at different speeds, in a dispersive medium depending on its frequency [53].

Along with Descartes, Newton is history's most prominent proponent of *the corpuscular theory of light*. The model stood in contrast to Huygens' wave treatment. Newton felt that an experiment, in which he first split white light with one prism, and then reconstituted it back to its original white beam, settled the matter. This model ran into trouble though, as it failed to explain aspects of light such as refraction, diffraction, interference, and polarisation.

The Dane Ole Christian Römer put Aristotle's assumption that lights propagation was instantaneous to rest. He correctly predicted that the time light would spend traversing the distance from Jupiter's moon, Io, would delay its emergence from an eclipse by Jupiter, by about ten minutes compared to calculations by astronomers of the time. Calculations, performed by several independent parties at that time, put the speed of light, in vacuum, at about $2.4 \cdot 10^8$ m/s, which is impressively close to our current estimation at $2.8 \cdot 10^8$ m/s.

In 1801 Thomas Young performed his famous double slit experiment and made his formulation of the principle of *interference*. Parallel with Young's efforts, Augustin Jean Fresnel expanded on Huygens' wave model and derived what is known as the Huygens-Fresnel principle, allowing for precise predictions of interference patterns. Mathematically it can be formulated as

$$U(r) = \frac{U_0 e^{ikr}}{r}, \tag{2.41}$$

where $U(r)$ is the complex amplitude at a distance r from a point source of a wave with a maximum amplitude of U_0, and $k = 2\pi/\lambda$ is the wavenumber.

Figure (2.29) shows a situation where an electromagnetic wave is emitted spherically from a point P_0.

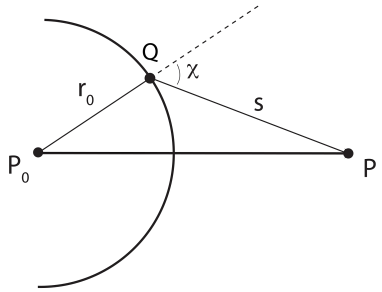

Figure 2.29: *Illustration of the Huygens-Fresnel principle. P_0 is considered to be a point source of electromagnetic radiation. The wave amplitude at point P can be evaluated as sums of contributions of secondary waves, originating from the wavefront at the points Q [54].*

Here it must be noted that there are several approximations and simplifications made, in particular, that the radiation originates from a point source. For the equation to be physically valid, we must require $r << \lambda$. To make the amplitude agree with experiments Fresnel had to make introduce a correction constant, $-i/\lambda$, by the assumption that the secondary waves oscillate a quarter of a period out of phase with respect to the primary wave, and that the magnitude of the secondary waves are in a ratio of $1/\lambda$ to the primary wave. As well an inclination factor $K(\chi)$ with a maximum at $\chi = 0$, and a value of zero at $\chi = \pi/2$, rendering a refined complex amplitude

$$U(P) = -\frac{i}{\lambda}U(r_0)\int_S \frac{e^{iks}}{s}K(\chi)dS, \tag{2.42}$$

where S is the surface of the sphere and s is the distance between Q and P.

By this principle, when considering contributions from several sources and using the principle of superposition, interference patterns could be correctly predicted.

Both Young and Fresnel were ridiculed by their contemporaries, as their theories were not conforming with the dogmas laid down by Sir Isaac Newton, but the observable phenomena of interference could not be mocked out of existence, and by 1825 the body of scientists was mostly unified around a wave theory of light [47]. A discovery that greatly fortified the wave interpretation as per the Huygens-Fresnel principle was the observation of what is known as the *Arago* or *Poisson spot*. It is a bright spot that can be observed at the center of a circular objects shadow on a screen, due to diffraction. For the phenomena to be observable, the light source must be a quasi point source, obtained by for instance using an illuminated pinhole. The dimensions of the set-up must be so that $F = d^2/l\lambda \leq 1$, where F is the Fresnel number, d is the diameter of the circular object, l is the distance between the object and the screen.

2.4.2 Electrodynamics

So far little has been said about the underlying physical mechanisms of light, the phenomena remained too elusive and intangible. In the decades leading up to his premature passing in 1879, James Clerk Maxwell published many works, culminating with *A Treatise on Electricity and Magnetism*. Together, his work must be regarded as the single most important contribution to our understanding of electromagnetic radiation, and as a consequence, of light. His writings are considered to be of poor literary quality, with many digressions and unclear rhetoric, but the underlying mathematical and physical interpretation, which forms the body of the field that we now call *electrodynamics*, is a cohesive and monumental body of theory. The outreach of Maxwell's work rivals the mechanics derived from Newton's laws. Maxwell's equations, 4 in number, are named after Gauss (two of the four), Faraday and Ampère, the scientists the equations are attributed to. In their modern formulation, in differential form, they are as follows:

- Gauss' law for the electric field,

$$\nabla \cdot \overrightarrow{\boldsymbol{D}} = \rho, \tag{2.43}$$

  where $\nabla \cdot \overrightarrow{\boldsymbol{D}}$ is the divergence of the electric displacement field and ρ the electric charge density. An interpretation is that electric field lines diverge out from electric charges.

- Gauss' law for the magnetic field,

$$\nabla \cdot \overrightarrow{\boldsymbol{B}} = 0, \tag{2.44}$$

  where $\nabla \cdot \overrightarrow{\boldsymbol{B}}$ is the divergence of the magnetic flux density. An interpretation is that the magnetic field has no divergence because there are no magnetic monopoles.

- Faraday's law,

$$\nabla \times \overrightarrow{\boldsymbol{E}} = -\frac{\partial \overrightarrow{\boldsymbol{B}}}{\partial t}, \tag{2.45}$$

  where $\nabla \times \overrightarrow{\boldsymbol{E}}$ is the curl of the electric field and t time. An interpretation is that an electric field arises from a time-varying magnetic field.

- Ampere-Maxwell law,

$$\nabla \times \overrightarrow{\boldsymbol{H}} = \overrightarrow{\boldsymbol{j}}_f + \frac{\partial \overrightarrow{\boldsymbol{D}}}{\partial t}, \tag{2.46}$$

  where $\nabla \times \overrightarrow{\boldsymbol{H}}$ is the curl of the magnetic field and $\overrightarrow{\boldsymbol{j}}_f$ is the electric current density of the free charges. An interpretation is that a magnetic field arises from an electric current as well as from a time-varying electric field. This is the only of the equations that Maxwell contributed to in itself, by adding the last term on the right side. This addition makes the four equations mathematically consistent for non-static fields and allows for the derivation of electromagnetic waves [52].

The electric displacement field, $\boldsymbol{D}$, is related to the electric field, $\boldsymbol{E}$, by the relation $\boldsymbol{D} \equiv \epsilon_o \boldsymbol{E} + \boldsymbol{P}$, where $\epsilon_0 = 8.85 \cdot 10^{-12}$ F/m is the vacuum permittivity and $\boldsymbol{P}$ is the density of permanent and induced dipole moments in the material. The magnetic flux density, $\boldsymbol{B}$, is related to the magnetic field, $\boldsymbol{H}$, by the relation $\boldsymbol{H} \equiv \boldsymbol{B}/\mu_0 - \boldsymbol{M}$, where $\mu_0 = 4\pi \cdot 10^{-7}$ H/m is the vacuum permeability and $\boldsymbol{M}$ is the magnetization vector field.

With the addition of the Lorentz force, $\boldsymbol{F} = q(\boldsymbol{E} + \boldsymbol{v} \times \boldsymbol{B})$, where q is the particle's charge and $\boldsymbol{v}$ is the particles charge, all of the classical electrodynamics can be derived from Maxwell's equations.

Most notable in this context is the derivation of the wave equations for the electric and magnetic fields. In their most simplified forms, they look like

$$\frac{\partial^2 \overrightarrow{\boldsymbol{E}}}{\partial t^2} = c^2 \frac{\partial^2 \overrightarrow{\boldsymbol{E}}}{\partial z^2} \tag{2.47}$$

and

$$\frac{\partial^2 \overrightarrow{\boldsymbol{B}}}{\partial t^2} = c^2 \frac{\partial^2 \overrightarrow{\boldsymbol{B}}}{\partial z^2}, \tag{2.48}$$

where $c = \frac{1}{\sqrt{\epsilon_r \epsilon_0 \mu_r \mu_0}}$ is the speed of light, and z is the direction of propagation. The equations has solutions on the forms

$$\overrightarrow{\boldsymbol{E}} = E_0 \cos(kz - \omega t) \overrightarrow{\boldsymbol{i}} \tag{2.49}$$

and

$$\overrightarrow{\boldsymbol{B}} = B_0 \cos(kz - \omega t) \overrightarrow{\boldsymbol{j}}, \tag{2.50}$$

where $E_0 = cB_0$. These solutions together form a planar electromagnetic wave, as represented in figure (2.30). Maxwell thus concluded: *The agreement of the results seems to show that light and magnetism are affections of the same substance, and that light is an electromagnetic disturbance propagated through the field according to electromagnetic laws* [55].

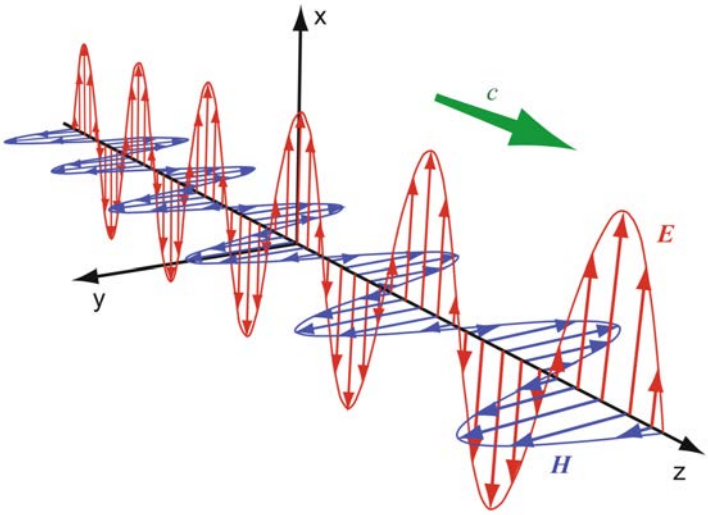

Figure 2.30: *Light as modelled by electrodynamics, here in the form of linearly polarized coherent light - the so called plane wave - with oscillations in the electric and magnetic fields perpendicular to each other and to the direction of propagation [52].*

2.4.3 The photon

For a short while, the matter of the nature of light seemed to be settled. There was still the unresolved issue of the medium in which the electromagnetic waves propagated. Various schemes were attempted to identify such a medium, the so-called *aether*, but they remained unsuccessful. In 1905 Einstein published his special theory of relativity, where he argued that such a medium was superfluous. His mathematical description of the *photoelectric effect*, along with Planck's introduction of the quantum, as a response the Violet catastrophe (relating to Rayleigh-Jeans law, that predicted divergent radiation at frequencies above 10^5 GHz), again rocked the notion of light and reintroduced the idea of the corpusculae of light - the so-called *photon*.

Einstein's description of the photoelectric effect entails light of discrete quantum being absorbed by atoms, leading to the emittance of electrons. A single quantum of light, or photon, is absorbed for each electron emitted. Reversely, quantum mechanics describes a process of generation of light, where an excited electron loses some of its energy and emits light, in the form of a single photon. By this description, all matter that has a positive temperature is continuously emitting and absorbing photons, according to internal energy and radiation from the surroundings.

Photons are considered to be massless particles, but they have momentum, given by the De Broglie equation

$$p = \frac{h}{\lambda}, \tag{2.51}$$

where p is momentum, h the Planck constant and λ the wavelength. The wavelength is related to the frequency by

$$c = \nu\lambda, \tag{2.52}$$

where c is the speed of light and ν the frequency. The energy of the photon is given by the Planck-Einstein relation

$$E = \frac{hc}{\lambda} = h\nu. \tag{2.53}$$

2.4.4 Quantum field theory

Physicists have further evolved our understanding of electromagnetic radiation, as well as all other forms of energy and interactions. What is considered to be perhaps the most concise and coherent of current models is what is labeled *quantum field theory*. I myself have had little in ways of formal courses here, and only have a rudimentary understanding of the matter. The field theory is little used in the community that develops the practical applications that have been of relevance in this project, I, therefore, end the elaboration on this subject here, and continue with topics more relevant to the experimental project.

2.4.5 Lasers

The word laser is an acronym for Light Amplification by Stimulated Emission of Radiation. In 1946 Charles H. Townes was awarded the Nobel Prize in physics for the development of laser principles, and the first laser was made in 1960 by Theodore Maiman [56].In figure (2.31) the main components of a typical laser can be seen.

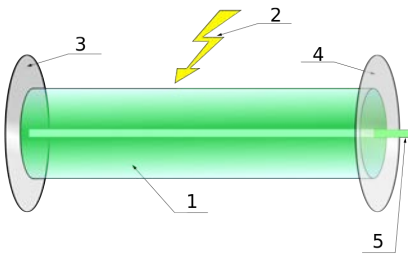

Figure 2.31: *Components of a typical laser: 1. Gain medium 2. Laser pumping radiation 3. High reflector (mirror) 4. Output coupler (mirror) 5. Laser beam[57]*

A laser is a device that creates a beam of concentrated, monochrome and coherent light. The light originates from stimulated atoms that emit photons. The trick is to generate a cascading feedback mechanism, where the stimulation spreads and sustains itself through positive feedback. In this project, a so-called *solid-state* laser was used. A crystalline rod, which is doped with ions to provide a required energy state, is trapped between two mirrors, in what is known

as the *Fabry-Perot cavity*. It is then excited with electromagnetic radiation, causing excitation and emittance in the material. To feed the process, you need to add energy, referred to as optical pumping, commonly done with a flash tube or optical diodes. The radiation bounces back and forth between two mirrors, creating a standing wave, the one at one end transmits 1-5% of the light that is then let out as what we perceive as the laser beam.

2.4.6 Flourescence

Fluorescence is the phenomenon that qualitatively can be described as: When a substance that is radiated with light of some wavelength (or color) emits light at another wavelength (or color). The phenomenon has been known since at least the 16th century [58], but in our age, we describe its mechanism by quantum mechanics, where an orbital electron is excited by a photon from the incoming radiation and then is relaxed again, emitting a photon in the process. Experimental work shows that the process is more complex, but a simplified description allows the process to be described in two steps [59]:

- Excitation:

$$S_0 + h\nu_{ex} \rightarrow S_1$$

- Fluorescence:

$$S_1 \rightarrow S_0 + h\nu_{em} + heat,$$

Where S_0 and S_1 denotes the relaxed and the excited states and $h\nu$ is the photon energy by the Planck-Einstein relation (equation (2.53)). Inherent in this process is that the emitted photon must have less energy than the initially absorbed photon, as some energy is lost to heat in the process.

2.4.7 Geometrical optics

One of the fields that extensively probe the nature of light is the lensmaking community. Their highly practical but also extensively theoretical field is known as *geometrical optics*. Here we introduce another model of light - *the ray model*. On the most fundamental level, lenses are constructed by imagining light traveling in straight rays, emitted in every direction, from the object. The purpose of the lens is to map these rays, through the interfaces and various materials, and reconstruct the object, in the image plane. On a more involved level, lens makers also deal with the wave and quantum natures of light, by making corrections for unwanted interference and aberrations, and by designing filters and coatings to limit reflection and filter out unwanted radiation.

The most basic lens components are the *concave* and the *convex* lenses, figure (2.32) shows how they differ.

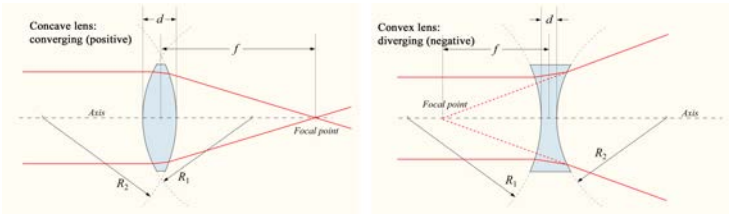

Figure 2.32: *Cross sections of a concave and a convex lens, normally the lenses are disk shaped in the plane going into the paper, around the optical axis (the dashed line) [60].*

To calculate the focal length of the lens surrounded by air (with an approximated refractive index of zero) we use the lensmaker's equation

$$\frac{1}{f} = (n-1)\left(\frac{1}{R_1} - \frac{1}{R_2} + \frac{(n-1)d}{nR_1R_2}\right), \tag{2.54}$$

where f is the lens' focal length, n is the refractive index and R_1, R_2 and d are as specified in figure (2.32). Convex lenses are *converging* and concave lenses *diverging*. In a real camera objective there are numerous lens elements. In addition to converging and diverging lenses they are aspherically shaped lenses, to avoid spherical aberrations, as well as lenses designed to avoid chromatic aberrations, see figure (2.33).

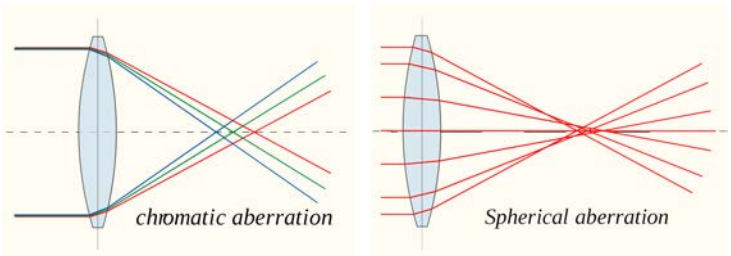

Figure 2.33: *Chromatic and spherical aberrations. It is desirable that all the rays intersect in the focal point to form a sharp image. The chromatic aberrations are caused by the lens material being dispersive and is usually countered by an achromatic doublet, which is a bonding of two lenses with differing dispersion. The spherical aberrations are a result of the sphere not being the ideal shape for image formations, but it is still commonly used, as it is the simplest shape to grind and polish. Spherical aberrations are countered by making lens components that have aspherical corrections [60].*

It is still useful to consider what is known as the *thin lens approximation*, in particular, to understand such concepts as focal length and magnifications, which are vital in being able to use an imaging system deliberately. Figure (2.34) shows how a single converging lens is used to form an image.

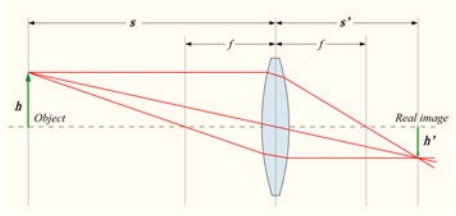

Figure 2.34: *Image formation by a single converging lens [60].*

With the distances as specified in figure (2.34), for a lens of much smaller thickness than the diameter, we get the thin lens formula

$$\frac{1}{s} + \frac{1}{s'} = \frac{1}{f}. \tag{2.55}$$

To focus an object in the image plane, we shift the lens elements according to equation (2.55), to make the plane given by h' fall onto our imaging plane (camera sensor).

From simple geometrical considerations, we get the formula for the transverse magnification

$$\gamma = -\frac{h'}{h} = -\frac{s'}{s}, \tag{2.56}$$

where h, h', s and s' are lengths as specified in figure (2.34). The negative sign signifies that the image is inverted with respect to the object.

The aperture of a lens is the effective lens diameter. As there are benefits to being able to alter this, lenses generally come with an adjustable aperture, often in the form of adjustable intersecting blades. In figure (2.35) a typical example from inside a camera-lens can be seen. A lens' maximum aperture is a number proportional to its size, and thus its ability to capture light. When the aperture stop is left at the largest, the maximum amount of light is let in. As the aperture stop is reduced, less light passes through. For camera lenses, the convention is to give the aperture stops as ratios of the focal length, f, a usual range could be $f/2.8$ to $f/22$.

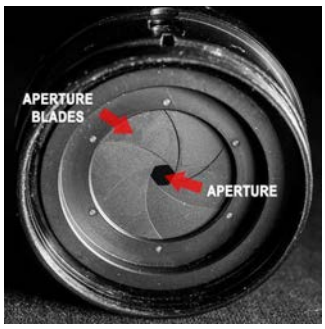

Figure 2.35: *Example of the typical aperture mechanism found inside photographic lenses [61].*

When the aperture is altered the imaged *depth of focus* (DOF), is affected. A large aperture gives a shallow DOF and a smaller aperture increases the DOF. This is a phenomenon that it is hard to find a good physical explanation for in the literature. I brought this up with the in-house specialist on geometric optics and light physics at the institute, Arnt Inge Vistnes, and he related his way of thinking about it, which I fount to be an intuitive and intriguing explanation. Much like Fermat's principle this reasoning does not convincingly describe the underlying physics, but rather serves as an illustrating geometrical analysis. Figure (2.36) shows the principle.

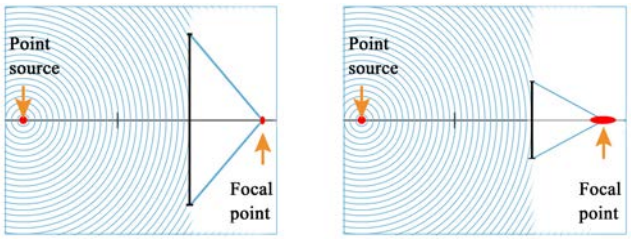

Figure 2.36: *Light is radiating from a point source and is imaged by a lens with a large aperture on the left, and one with a small aperture on the right. As the large aperture catches a large segment of the wave-front "it has better information" about the origin of the radiation, through the front curvature, and it is thus more able to map the incoming radiation to the appropriate focal point. Inversely, the lens with the smaller aperture "sees" less of the wave-front, and thus has less information about the distance to the origin.*

In case no one else has made claim of this explanation of DOF before, I am tentatively coining it *Vistnes' Principle*, as it is surely worthy of a good name.

The resolution a lens can reproduce is ultimately limited by its *diffraction limit*. For a microscope, this is quantified by the *Abbe limit*, after Ernst Abbe. In 1873 he found a relation describing the minimum distance resolvable by a microscope [62]

$$d = \frac{\lambda}{2n \sin\theta}, \tag{2.57}$$

where d is the dimension of the minimal object, λ the radiation wavelength, n the refractive index and θ half the angle the object will project from the lens to the image plane. For practical purposes the ideal Abbe limit is considered to be $d \approx \lambda/2.8$, giving a quick reference to how small an object we can resolve with an optical microscope using radiation of a given wavelength.

For an imaging system, such as the digital camera with a telephoto lens used in this project, the elaboration of the diffraction limit is more complicated. The diffraction effects interact with the pixel grid, together we then consider *the convolution of the point spread function*. The point spread function is also known as the *Airy disk*; it is a function that describes the best-focused spot that a perfect lens can create, described by George Biddel Airy [63]. In fact, the Airy disk is a pattern described by a Bessel function of the first kind. Figure (2.37) shows a computer generated example of the Airy disk pattern.

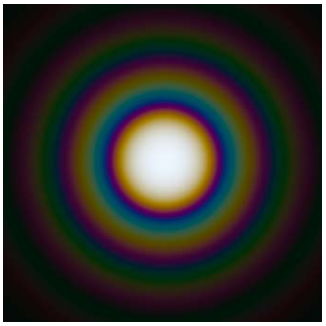

Figure 2.37: *Computer-generated Airy disk from diffracted white light [64]. Far from the aperture, the angle at which the first minimum occurs, measured from the direction of incoming light, is given by the approximate formula* $\sin\theta \approx 1.22\lambda d$*, where* d *is the lens diameter (or aperture).*

To quantify the diffraction limit of a telescope, or a telephoto lens, it is common to use the Rayleigh criterion, after Lord Rayleigh,

$$\sin\theta = \frac{x}{f} \approx 1.22\frac{\lambda}{d}, \tag{2.58}$$

where d is the lens diameter (or aperture), x is the smallest resolvable distance in the image plane, and f is the lens focal length. The evident lesson to learn from this is that the lens diameter and the radiation wavelength are the tunable parameters. The lens will thus ideally resolve the small spatial frequencies according to the Rayleigh criterion, but how the airy disk scales with and lands on the pixel grid in the image sensor (elaborated in section (2.4.8)), ultimately determines the limitations of the system.

A body of a medium with one refractive index, surrounded by another medium, such as the water in a pond surrounded by air, is also a lens. Compared to air, the water magnifies objects under the surface. In this project, a plane at a distance, s_i, inside a cell of refractive index, $n_i \approx 1.5$, is imaged by a camera at a distance, s_o, from the cell. As the plane moves a distance, Δs_i, further into the cell we want to maintain a constant magnification, M, by moving the camera the appropriate distance, Δs_o. This can be achieved by assuring that

$$M \propto \frac{1}{(s_o - \Delta s_o) + \frac{s_i + \Delta s_i}{n_i}} = constant \tag{2.59}$$

In the project, the plane is created by a laser sheet. As the camera and the plane, both will be moving at constant velocities, maintaining a constant magnification M implies the relation

$$v_{camera} = \frac{v_{laser}}{n_i}. \tag{2.60}$$

A related concept, that follows from the considerations taken in Fermat's principle, is the *optical path length*. Formally it can be defined by the line integral

$$OPL = \int_C n \mathrm{d}s = s_o + n_i s_i, \tag{2.61}$$

where n is the refractive index, and $\mathrm{d}s$ is the infinitesimals of the path C. An interpretation of the OPL would be that rather than saying that light slows down as it enters a medium of higher refractive index, it goes into a medium where the *optical path* is longer than the *geometrical path* that we measure.

2.4.8 Imaging with a digital sensor

In figure (2.38) we see a schematic of a digital single reflex camera, of a similar type to the one, used in the experiments. As the camera is used in video mode, the mirror and shutter in the camera are left permanently open, and the shutter speed of each frame is handled by regulating the integration time over the sensor.

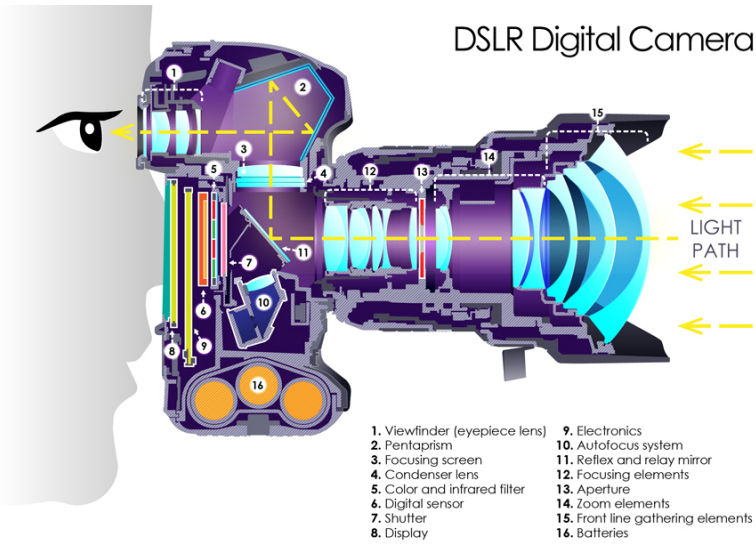

Figure 2.38: *Diagram of a digital single lens reflex camera, with a mounted lens[65].*

The heart of the camera is the image sensor. The *sensor* is an array of millions of tiny sensors. In figure (2.39), we see a schematic of such an array.

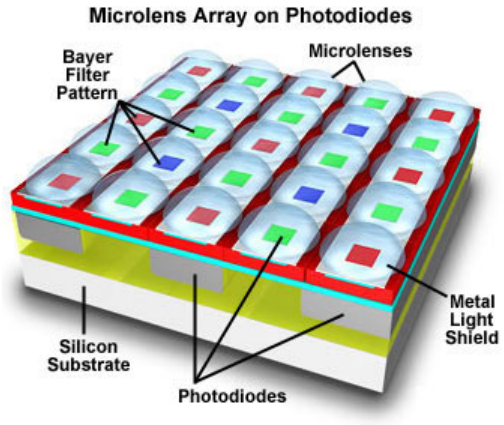

Figure 2.39: *Diagram of an array of individual image sensors[66].*

Each sensor, or *pixel*, is a piece of semiconductor material, connected to integrated electronics for storage, and even on-site processing. Modern digital cameras typically record images in a format known as *RGB* (red, green and blue), where the three colors are recorded in separate *channels*. The lenses covering the sensors are there to focus the incoming light, as only a part of the surface is covered by the photosensitive material. The color filters separate red, green, and blue light so that only one channel is recorded, at any one site. The values for the two other channels are then obtained by averaging over the nearest neighbors for one, and the diagonal neighbors for the other. There are many filter patterns in use, but the by far most common is the Bayer, that can be seen in the figure. For each red or blue site, there is two green. This is because green light is in the center of the spectrum visible to humans. The green light is more important, for our impression of image brightness, which in turn is what creates contrasts, and thus shapes, which dominate in importance over colors, in our perception.

There are many sensor technologies in use. In the early years of digital imaging CCD (charge-coupled device) sensors dominated, but now CMOS (complementary metal-oxide-semiconductor) are more common, and it is this type of sensor that is in the camera used in this project. In figure (2.40) we see a single pixel sensor from such a CMOS array.

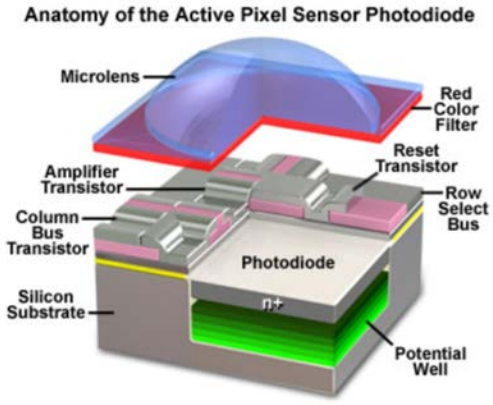

Figure 2.40: *Schematic illustration of a pixel element in a CMOS image sensor [67].*

The sensor is a photon detector. One by one the photons are absorbed, and they each excite a single electron. The electrons are held in a trap, and as more are collected, the charge builds up. When the integration time is up, the voltage is read off, and the trap is flushed and reset for a new recording. Ideally, a single photon can be detected, but as the sensor is active, there is a constant probability of electrons being excited by leaking current, what is known as dark noise. There are several more sources of noise that all add up in the estimation of the sensor capabilities. Analysis, evaluation, and reduction of noise is a significant part of any sensor technology. In general, whenever new technology offers enhancement of the sensor sensitivity, it comes with an

embedded contribution of noise that must be accounted for.

The theory behind noise estimation and sensor classification is elaborate and complex, but to offer some insight into the types of considerations that are made, the most general expressions for the characterization of a detector is offered. In the following derivations I reference the lecture notes for the course Unik4330 [67] and the textbook *Infrared Detectors and Systems* [68].

It is common to separate between a characterization expressed through the electrical signal in the sensor, or as a dimensionless signal, based on a photon count. Here we proceed with the former. To quantify the strength of the signal in the detector it is common to express its *power*. The energy carried by the signal, or power, is proportional to the square of the signal amplitude, i_s. Here signal impedance is not accounted for, so it would not be correct to give this power the customary units of watts, rather it remains a relative quantity, suited for system comparisons. The incoming signal power can be expressed as

$$i_{sig}^2 = (q\eta\phi_{q,sig})^2, \tag{2.62}$$

where q is the electron charge, η the quantum efficiency or the probability that an incoming photon will be detected, $\phi_{q,sig}$ is the incoming signal photon flux. The noise power is given by

$$i_n^2 = 2q2\eta(\sqrt{2}\phi_{q,sig} + \phi_{q,bg})\Delta f + i_{det}^2 = i_s^2 + i_{det}^2, \tag{2.63}$$

where $\phi_{q,bg}$ is the photon flux from so-called shot noise (photons that leak in that are not part of the signal), Δf is the signal bandwidth[8], i_s^2 is shot noise, and i_{det}^2 is noise from the dark current in the detector. We can now express *the signal to noise ratio*

$$\left(\frac{S}{N}\right) = \frac{(q\eta\phi_{q,sig})^2}{2q^2\eta(\sqrt{2}\phi_{q,sig} + \phi_{q,bg})\Delta f + i_{det}^2}. \tag{2.64}$$

As the denominator is a sum of noise terms, the largest source of noise dominates the characterization. Here it should also be noted that by the definition of the signal bandwidth, the noise factors other than i_{det} increase with prolonged integration times. It is usual only to keep the dominating noise term and ignore the others.

[8]The signal bandwidth is given by the integration time t_i, by the relation $\Delta f = 1/2t_i$. To fully explain how this works a more elaborated introduction to signal theory is needed, see [68]. The concept is derived with the assumption that the integration over a time interval, t_i, is equivalent to integrating the power spectrum from 0 to a frequency, $f = 1/(2t_i)$. Here it is assumed that the signal is "white", meaning that it has a power that is independent of frequency. The signal noise power then becomes proportional with the signal bandwidth.

A common industry standard, to give a number to the quality of a detector, is *detectability*. To derive this parameter, we quantify the smallest signal that the sensor can detect, the optical signal power for which the signal to noise ratio is unity, the so-called*Noise Equivalent Power*. To find the NEP the dominating noise term is kept, the others ignored. We set S/N=1, insert $\phi_{sig} = \phi_{q,sig} E_\nu$, where $E = h\nu$ is the photon energy according to equation (2.53), and solve for ϕ_{sig}. In the signal-limited case, which is the ideal case, this gives

$$\left(\frac{S}{N}\right)_{SL} = \frac{\eta \phi_{sig}}{2\sqrt{2} E_\nu \Delta f}, \tag{2.65}$$

$$\Rightarrow \quad NEP_{SL} = \phi_{sig} = 2\sqrt{2}\frac{1}{\eta} E_\nu \Delta f. \tag{2.66}$$

As the NEP is a measure for the inverse of the detector quality, *detectivity* merely is defined as

$$D = \frac{1}{NEP}. \tag{2.67}$$

The noise profile and detectivity of a sensor are important factors to look into when designing an imaging system. When using the imaging system in a practical situation, the most important thing to understand is the concept of *dynamic range*.

The digital sensor, along with the built-in processing, deliver images with a given bit-rate. This rate specifies the maximum dynamic range that the system can provide. For the recordings done, in this project, the camera has delivered frames with 8-bit RGB data. This means that each pixel contains red, green and blue values, between 0, for entirely dark, and 255, for saturated with light. Thus the dynamic range, for each channel is 256 (we also count the 0 value). To further elaborate on this concept I introduce *the effective dynamic range*, which can be interpreted as the degree of utilization of the systems optimal dynamic range.

As stated before, the individual pixels only sample one of the colors; the other two are estimated. The pixel can be regarded as a bucket, left out in the rain for the exposure time, the photons are the raindrops. When a specified amount of drops are collected, the sensor holds a charge equivalent of the value of one, as the drops keep increasing, the value goes up until we are out of bits, in our case the value is then 255. Whatever new drops that then land in the bucket, just run over the edge - the bucket is full.

There are two ways that the sensor can become saturated, one is if the physical capacitor gets fully charged, the other is if the charge is larger than what is defined as equivalent to the maximum allowed intensity value, in this case, 255. How we interpret this range is regulated by the parameter called *ISO*. When we

used analog film in cameras, the term ISO was defined as a measure of the light sensitivity of the film. Typically the least sensitive film you could get would have an ISO of 25, and it was used for conditions with extreme amounts of lights and rendered the maximum level of detail and effective dynamic range, at the other end of the spectrum were ISO 3200 films, for use in very poor light conditions, rendering grainy images with reduced effective dynamic range.

When we set a low ISO with a digital camera, each step in the dynamic range, from 0 to 255, represents a high number of photons. Thus, the signal to noise ratio is high. A high ISO is used in low light conditions. The digital intervals, from 0 to 255, then represent fewer collected photons. The signal to noise ratio is smaller, and the image becomes less sharp, resulting in a poorer effective dynamic range. In either case, the contrast in the image will impose challenges to the system. If there are both very bright and very dark areas in the picture, we have to make a compromise, either dedicating the range to the bright part of the image, or to the dark, or to some compromise, where the mid-tones are well represented.

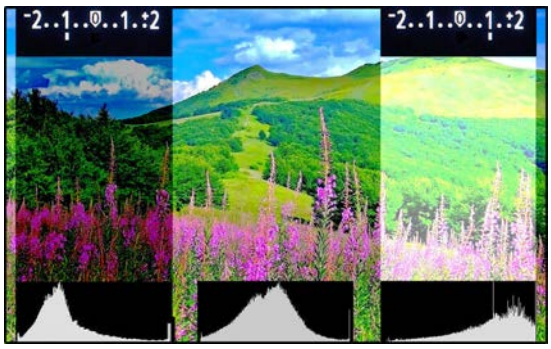

Figure 2.41: *Illustration of how the histogram - the graph at the bottom of each segment - can be used to correctly expose an image. The bar at the top, left and right, signifies stops of under- or overexposure [69]. As can be seen, the correctly exposed image has a much more even spread over the dynamic range, both highlights and shadows are well represented, with an emphasis on the mid-tones. In practical situations it will often not be possible to get an optimal rendering of the whole range, from the brightest to the darkest parts of the frame, one must, therefore, make a considered choice, as to how best represent the nuances that are of importance.*

The main tools to optimize the dynamic range in a practical situation are the histograms. In figure (2.41) we see how the dynamic range is properly exploited when correctly exposing an image. The "buckets" are filled in such a manner that a maximal number of shades and colors, from dark to saturated, are represented. In this case, only the histogram for the average, over the red, green and blue channels is depicted, but with an advanced camera, each channel can be inspected separately.

When we make a photographic image, we seek to perform an optimal exposure.

What this signifies, is that we try to have all our little buckets filled with such an assortment of drops, as to optimally represent the relevant information and dynamic range in the radiation from the depicted object. In a practical situation, the following parameters govern this:

- **The lighting of the object (as well as the object itself)** - in general, more light is better, but in some rare cases, such as on a very bright day, there can be more light than the system is optimized for.
- **The imaging system** - it is important to choose a sensor type and imaging system that is optimized for the specific situation.
- **The camera objective** - choosing a lens with a suitable focal length, aperture range and optical quality is critical to achieving high-quality images. Usually fixed focal length lenses are better than zoom lenses, and extreme wide-angle or telephoto lenses should be avoided.
- **Composition and imaging geometry** - irrelevant information should be physically removed or cropped out. Perspective distortions should be avoided by aligning the optical axis orthogonally to the object plane. It is also useful to keep in mind that most lenses perform better in the central region of the frame than toward the edges.
- **Filtering** - before the radiation enters the imaging system, we can add filters, so that we can dedicate the recording capacity to specific information.
- **The lens focus** - setting the focus ensures that the correct plane is captured.
- **The ISO setting** - this setting sets a baseline for the lighting situation. In a case with much light, a low ISO should be set, and in one with little light, a higher ISO must be chosen.
- **The white balance** - this setting gives a reference value for what is to be considered as color-neutral, and should be set according to the temperature of the lighting.
- **The lens aperture** - a small aperture means less light, but a larger depth of focus, whereas a large aperture gives more light and a more narrow depth of focus.
- **The exposure time** - longer exposure time gives more light but creates motion blur if the object or the camera is not stationary.

If the camera is used to record experimental data, as is the case in this project, it is of crucial importance to manually control all of these parameters, to optimize the imaging and to ensure consistency in the recordings.

CHAPTER 3

Experimental Methods

The experimental works presented here were conducted throughout several phases. I was introduced to the general idea for the master's project sometime into the first semester and started very slowly to look at some of the experimental issues already then. It was however not until the second year that I had the time to focus fully on the lab work. The most time-consuming parts involved finding solutions, designing the components and waiting for orders to be delivered. At times finding solutions to problems, that seem trivial in hindsight, represented serious concerns in the process, whereas other challenges resolved themselves surprisingly effortlessly. In this chapter, I wish to detail the steps that I went through in the development of an optical scanner for flow in porous media, in a series of experiments conducted, and in the computer analysis and visual rendering of the results.

3.1 The scanner

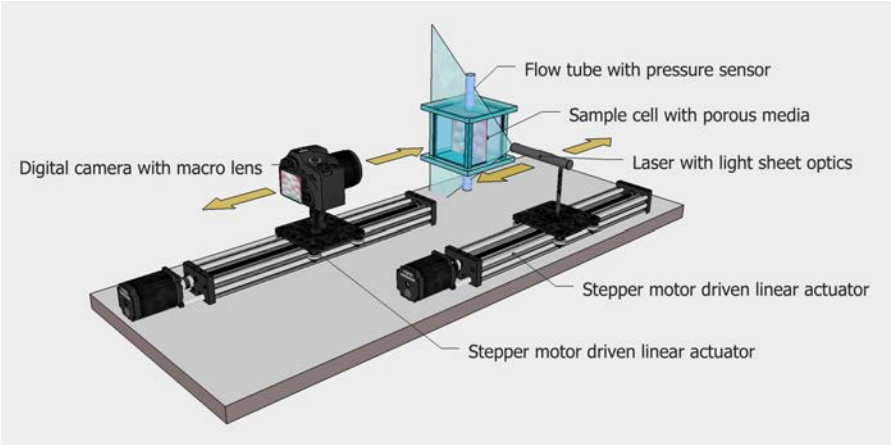

Figure 3.1: *Image from a 3D-model of the final set-up made in Sketch Up. The most important features are represented in the figure.*

The first part of the project was to develop a 3D-scanner for flow experiments. The methods themselves were developed experimentally, through research and

trial and error. A 3D-model of the final design can be seen in figure (3.1). In the first part of this chapter, the steps leading to the working scanner will be gone through. In the second, the flow experiment that was conducted with the 3D-scanner will be treated.

3.1.1 The sample container

A vital part of the set-up was the sample. It had to be suited for relevant flow experiments, contain a porous medium and at the same time allow for scanning. The container had to be large enough for flow patterns to form without reaching the boundaries, and at the same time small enough to be spanned and penetrated by the laser sheet.

To get some initial ideas of how the scanner could work, trials with microscopy test tubes, with a square base of approximately 1 cm x 1 cm and a height of 5 cm, were conducted. This set-up was practical for testing different liquids and dyes, to see how well the refractive indices matched, and to what extent the areas with the different dyes could be separated. As promising candidates emerged, the sample size was increased to a container with a base of approximately 2.5 cm x 5 cm and a height of 5 cm. This gave some idea of how deeply the laser would penetrate, as well as how much moving through the sample would affect the focus of the image. In figure (3.2), the set-up for these initial tests, as well as an initial result, can be seen.

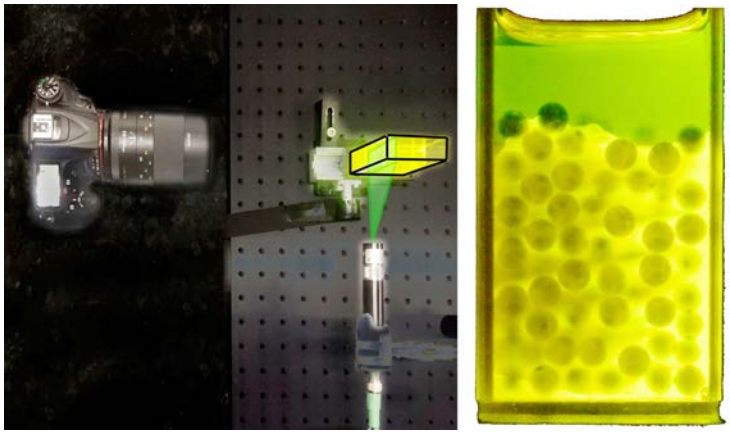

Figure 3.2: *Set-up to conduct tests to determine what liquids and dyes to use, as well as the sample dimensions, seen from above. The laser sheet, as well as the sample cell edges, have been drawn onto the image for clarification. The camera was sitting immobile on the table, and the laser remained fixed on a stand, with the sheet going vertically into the sample. The sample was placed on a manual slide actuator that was operated by turning a wheel. To get a more smooth motion, a strap was wound around the wheel. It could then be pulled to turn the wheel. On the right is a sample of what the camera recorded. 3 mm borosilicate beads are immersed in glycerol, with rhodamine 6G dye, at the bottom and barely past the interface, with rapeseed oil with difluoro dye, at the top.*

The sample had to have at least two entirely flat surfaces, that could act as windows without distortion, both for the incoming laser sheet and for the outgoing image. The logical solution was to make it with a square base and top, with rectangular sides. After testing with the few containers at hand, and also gluing together a primitive box, open at the top, from five sheets of 80 mm by 80 mm glass, an idea about the approximate realistic scale, had emerged. The solutions proposed from the in house glass-blowers and our regular suppliers for cell designs were not that good and not available on short notice. It was decided to design and construct the cell from scratch.

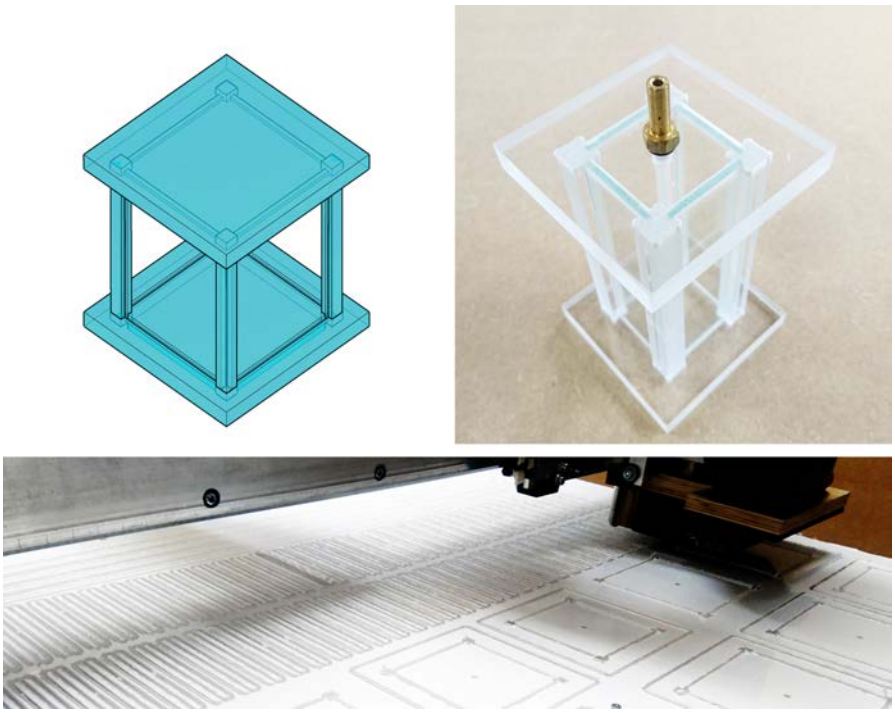

Figure 3.3: *3D-design made with Sketch Up and a finished flow container on the top left and right. The CNC-router carving out the top, bottom and columns on the bottom.*

The result can be seen in figure (3.3). The base, top and columns are made from plexiglass, drawn with Sketch Up and cut with a CNC-router at Newtone Studios in Oslo. The glass panes are cut out by the glass blower in the chemistry dept. of the University of Oslo. They are made from borosilicate glass. To have the opportunity to make different scale samples, I made bases and tops with inside cell dimensions of 30 mm x 30 mm, 50 mm x 50 mm, 80 mm x 80 mm and 100 mm x 100 mm, as well as columns that can be cut to size, up to 1 m long.

Figure 3.4: *Some details from the cell design. In the first two pictures, we see pieces cut from needle tips, glued across the drain and inlet of the cell. At the inlet there is a nipple on both ends, to ensure that the flow commences inside the matrix. On the middle right there is a picture of the spring with a plate to jam the bead matrix in position. The plate has a hole that can be threaded over the injection nipple. To the right, we see an outlet valve to vent air from the cell.*

Figure (3.4) shows details added to the sample cell design. When injecting liquids from one end, the drain at the other end got clogged if a bead was sucked in. To counter this, a thin grove was cut across the drain, and a snipped-off needle from a syringe was glued across. During tests, it became apparent that, when injecting from the top, the liquids had a tendency to flow across the beads in the gap over the bead matrix, and thus continue along the walls, rather than through the center of the sample. To prevent this, lids with nipples mounted in two directions were made, so that one would dig down and penetrate between the beads, while the other end served to fit tubes. Here too, a groove in the nipple was cut, and a piece of a needle tip was glued across.

When filling the sample, it was challenging to get rid of all the air at the top. Therefore, another hole was made, near one corner of the lid, with a nipple to drain excess air.

To allow for flow through a static medium, the glass beads needed to be locked in place. The beads were stuck against the container at the bottom and sides, but they could move freely upwards, as it proved impractical and very difficult to completely fill the cell with beads. One possibility would have been to sinter the beads, but this would have brought several challenges. The plexiglass would have melted, the medium would have fused with the container, and it would have been complicated to saturate the sample with liquid. A metal plate with a hole that fits over the matrix of beads was cut, complete with a spring that exerted a downward force, flexing against the underside of the lid.

To hold the lid in place, a clamp, from under the bottom to over the top, was applied. The top was sealed on, by putting silicone vacuum grease in the groove before putting it on.

3.1.2 The porous medium

As a starting point, the proposed medium was randomly packed spherical glass beads of uniform size. Based on previous work conducted at MIT by Dalbe

and Juanes [46], spherical borosilicate beads of diameter 3 mm were tested and chosen for the first experiment. The beads have product code *Z143928 Aldrich*, they are quasi-spherical, with a specified diameter of 3.0 mm ± 10%.

3.1.3 The fluids

With the medium given, the next step was to find matching liquids. For the scanning to work, the container, medium, and liquids need to have the necessary optical qualities. They need to be good transmitters of the laser sheet, be closely index-matched, and safe and practical to work with. The refractive index of a medium is usually both wavelength and temperature dependent. It is hard to find charts with both these factors accounted for. In table (3.1), some of the relevant fluids are listed.

Table 3.1: *Refractive indices for some media at approximately 20° C*

Medium	Refractive index
Borosilicate glass	1.51–1.54 [70]
Water	1.33
Glycerol	1.46-1.48 [71]
Rapeseed (Canola) Oil	1.47 [72]
Corn Oil	1.47 [73]
Sugar solution (80%)	1.49 [74]
Ethyl salicylate	1.52 [75]
Ethyl cinnamate	1.56 [75]
Methyl salicylate	1.54 [75]
Benzene	1.50 [75]

The most promising candidates were collected, and then borosilicate beads were poured into containers with the liquids. The containers were sorted by visual inspection, both in the lamp light and when illuminated with the laser. An assortment of the test-tubes can be seen in figure (3.5). After the early trials, it was opted to carry on with glycerol and rapeseed oil. Reference data, for the two fluids, can be seen in table (3.2).

Figure 3.5: *A selection of some of the liquids that were tested. Most were immediately discarded upon visual inspection, but the more promising candidates were put in the square-based container and scanned with the primitive set-up.*

Table 3.2: *Reference data for the two fluids, at approximately 20° C.*

Parameter	Glycerol	Rapeseed oil
Chemical formula	$C_3H_8O_3$ [76]	-
n (refractive index)	1.46-1.48 [77]	1.47 [72]
ρ (density)	1.261 g/cm ^{3} [76]	0.914-0.917 g/cm^3 [78]
μ (dynamic viscosity)	1412 mPa·s [76]	63.5 mPa·s [79]
ν (kinematic viscosity)	1119.7 mm^2/s [76]	78.2 mm^2/s [78]
Melting point	17.8° C [76]	-10° C [78]
Boiling/smoke point	290° C [76]	220-230° C [78]
γ (surface tension - vs air)	64.0 mN/m [80]	31.3-33.4 mN/m [79]

3.1.4 The laser

Several laser solutions could be imagined as suitable for this type of a scanner, but based on the work of Dalbe and Juanes [46], a 532 nm laser with fixed sheet optics was chosen. It is a Z-laser ZM18GF029 operating at 5-30 V DC and delivering an output of 1-200 mW. The lasing material is Nd:YAG (neodymium-doped yttrium aluminum garnet; Nd:$Y_3A_{l5}O_{12}$). Nd:YAG absorbs in the bands between 730-760 nm and 790-820 nm and typically emits at 1064 nm, in the infra-red. To get the 532 nm green light used, the pulses are frequency doubled in the device[1]. The device generates a concentrated beam with a Gaussian intensity distribution. Attached at the tip is a distorting lens that fans the ray out in a sheet with a 60° fan angle.

3.1.5 The fluorescent dyes

The first dye trials were done with Rhodamine 6 G and Difluoro, from Sigma Aldrich. It turned out that the Rhodamine 6G would only dissolve in the glycerol and the Difluoro only in the rapeseed oil. At first, these tests seemed promising, but it turned out to be very difficult to distinguish the liquids through image analysis, as the two emitted wavelengths were too close.

A feature of fluorescent dyes is that they always emit at a longer wavelength than the incident light. A right choice then seemed to get one dye with an emission peak quite close to the laser wavelength and another with the peak as far away as possible (within the visible spectrum). After some constructive communication with a company called Exciton, fluorescein (peaks at 548 nm) for the glycerol and pyrromethene (peaks at 650 nm) for the rapeseed, were ordered. This turned out to be a good choice, as can be seen in figure (3.6). The glycerol with the fluorescein comes out like a bright green, and the rapeseed as a deep red, making the two distinguishable, both to the naked eye and by image processing. Some results from these tests can be seen in figure (3.6).

[1]Frequency doubling is an optical process in which two photons with the same frequency are combined in an interaction with a nonlinear material, to generate a new photon with twice the energy of the initial photons. The process is rather intricate, but can be investigated in the reference source [81].

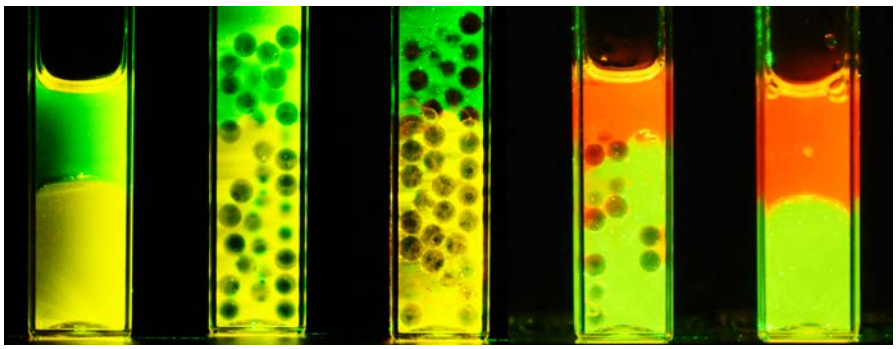

Figure 3.6: *From the left, we see glycerol with rhodamine 6G dye at the bottom and rapeseed oil with difluoro dye at the top, without glass beads. In the next tube, 3 mm borosilicate beads are immersed in the same mix. As can be seen, it is no longer entirely clear where the boundaries between the two liquids are. In the center, there is Rhodamine 6G in both the glycerol and in the rapeseed on top. The dye in the rapeseed is not dissolved, and the green specks are a result of Rayleigh scattering, emitting at the same wavelength as the laser. At first, this image was encouraging, but further testing revealed some problems, such as the oil transmitting particles to the glycerol and leaving them on the beads and sample walls. In the final two tubes there is fluorescein 548 in the green glycerol and pyrromethene 650 in the red rapeseed oil, with beads in the former, and without in the latter.*

To further improve the optical separation of the two phases, a notch filter from Thorlabs was added. It removes the wavelengths around the emission from the laser. This could alternatively be replaced with a low pass filter that cuts off at wavelengths above around 540 nm. For further improvement one more notch filter, eliminating the wavelengths between the two can be considered. The emission graphs for the dyes and the transmission graph for the filter can be seen together in figure (3.7).

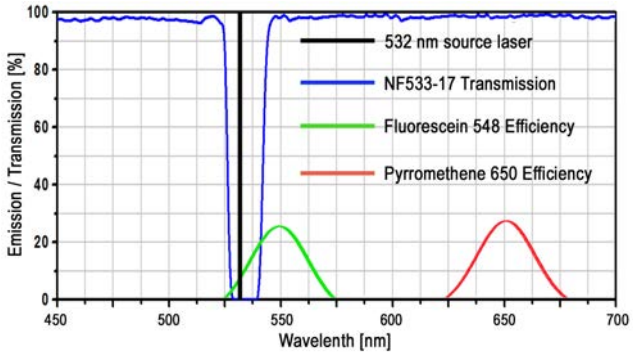

Figure 3.7: *Chart made from charts the manufacturer of the dyes, Exciton [82], and the manufacturer of the notch filter, Thorlabs [83], on the right.*

3.1.6 Dye conentration

Through a series of trial and error, it was determined that a dye concentration of 5-20 mg/l was appropriate for both dyes, depending on the sample size and fluid saturation. For instance, if the flow experiment led to a wide front and fingering, the defending fluid would have a high saturation. To compensate, the invading fluid should then have a higher dye concentration to be detectable, especially where the fingers were thin.

3.1.7 Imaging

Right from the beginning of the testing, until the end, a Nikon D7200 DSLR camera, with a Rokinon 100 mm f 2.8 macro lens, with manual focus, was used to record the laser sheets. A camera body and a lens of the same make and model can be seen in figure (3.8) Some tests with smaller cameras were done. They had the appeal of being lighter and more compact, but they proved to be hard to focus, as they were not optimized for manual focus. It should be noted that the rig can be improved with a camera upgrade. This will be treated in the discussion.

Figure 3.8: *The camera body and the lens (images taken from the manufacturer's web sites).*

As the sample scan was to be constituted from a succession of frames, the natural starting point was to record the image sequence as video. The drawback with this is that the resolution of each frame, as well as the overall image quality, is lower. Trials showed that the resolution and the image quality were sufficient. To ensure comparable recordings the camera was set in a manual mode, with specified white balance, shutter speed, aperture, ISO, compression mode and frame rate.

When doing the first tests, the sample was on a translational stage, that could be moved by turning a wheel. See figure (3.2). The camera and the laser remained in fixed positions. Even with a sample with a base of 10 mm x 10 mm it was apparent that the focus was not maintained, as the sample was shifted

through the laser sheet. The distance from the image sensor to the object plane remained the same, but the optical path was altered as the sheet was moved deeper into the sample, altering the fraction of air to sample. The liquids and media had refractive indices of about 1.5. When you look at a plane inside the sample it is like when you look at your hand held under water - it gets magnified, compared to when it is held at the same distance in the air. The light gets refracted at the interface and the medium acts as a lens.

To compensate for this, and keep the image focused throughout the sample, two solutions were envisioned. One approach would be to do like Dalbe and Juanes at MIT [46]. They reduced the aperture on their objective, to achieve sufficient depth of focus, for the image to remain sharp throughout the sample, without moving the camera or altering the focus. There are three major drawbacks with this solution. The first is the loss of light intensity. When one reduces the aperture, one reduces the incident light intensity on the sensor. One must compensate by setting the ISO value higher, which reduces image quality, or by extending the exposure time, which affects frame rate and also creates a risk of motion blur. The second is the enlargement of the depth of the image plane. When the depth of focus is increased, one images a thicker slice of the sample. Even though the laser sheet only illuminates a thin slice, there is light scattering and spreading, creating a blur on the image of the illuminated plane. The third drawback is the warping of the sample dimensions. When the fraction of air to medium changes, the magnification of the object also changes, making the recording skewed, stretching the image of the sample more as the laser penetrates deeper into the sample.

The more appealing solution is to move the laser and the camera on separate stages, to maintain a constant optical distance, as the fraction of air to medium changes. Per unit length the laser moves into the sample, the camera should move $1/n$ units length, where n is the refractive index of the medium, as per equation (2.61).

Several crude sketches of how such stages could be conceived were made. A stepper motor was chosen as motorization, as they are cheap, reliable, precise and easy to program through a DAQ interface. In the beginning, the plan was to machine the whole rig from base components, but during the search for these, several ready-made translational stages were found. In the end, two 500 mm linear actuators with fitting stepping motors, from Openbuilds in the USA were chosen. The actuators came in parts, but the assembly was done in a couple of hours. An added benefit of everything from Open Builds is that all the pieces are available as computer 3D-models that can be downloaded and imported to software such as Sketch Up. The actuators have product code *1170-Bundle Openbuilds*. A picture of an actuator of the same make can be seen in figure (3.9).

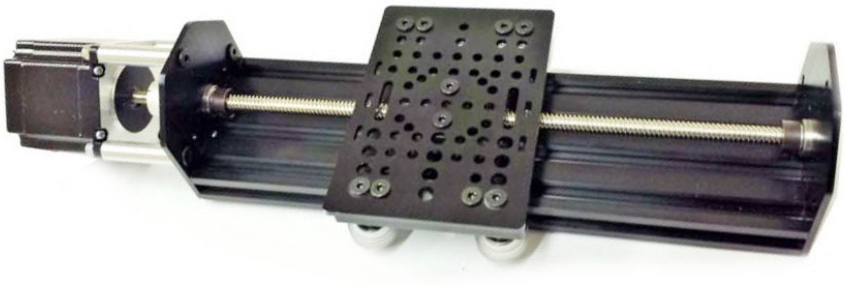

Figure 3.9: *The type of linear actuator used, here with a 300 mm rail (image taken from the manufacturer's web site).*

There were already some heavy breadboards, with pre-drilled M6 holes, from Thorlabs, in the lab. One of these was used as a base for the build, and then it was just a matter of drilling some mount holes in the actuators and screwing them on. Adaptors from Thorlabs were used to attach the laser to one sled, allowing for adjustments of the laser sheet around the three orthogonal axes of rotation. A solid aluminum bracket was fabricated to mount the camera, in a vertical position, on the other sled.

To have a reference, for the locations of the sleds on the actuator rails, measuring tapes were printed out on paper, and taped to the rails, along with a piece of red tape on each sled, to mark the read-off points.

3.1.8 Controlling the linear actuators

The linear actuators for the laser and the camera are driven by NEMA-23 stepper motors. These can be operated through a DAQ unit by a script on a computer. ST5-S controller units from Applied Motion were chosen, and upon testing, they worked well with the motors supplied with the actuators. The motors can be programmed to move a precisely determined amount of steps, at a specified rotational speed. Each full rotation comprises a fixed number of steps, and the actuators move a set length per rotation.

The actuators are controlled from a laptop, via a control script that was written in Matlab. The program starts with the assumption that the sample cell is placed centrally in the camera frame, with the laser traversing across the center line of the cell, giving a known geometry. This has the added bonus that one can observe the image plane directly across the inlet and outlet, in the cross-section that has the highest probability of capturing the most significant fraction of the flow pattern.

3.1.9 Determining the geometry of the scan and the scanning velocity

The total volume that gets scanned is spanned by three orthogonal rectangles, a so-called *hyper-rectangle* or *3-orthotope*. The axes are defined as x and y

spanning the plane given by each frame recorded by the camera, with x as the horizontal direction and y as the vertical, and by the direction of movement of the laser as the z-axis.

As previously stated, the velocities of the two stages were coordinated, so that the camera moved at $1/n$ times the speed of the laser. It was desirable to have the voxels (*voxel* is the term for a 3D-*pixel*) recorded attain a cubic shape. The pixels in the xy-plane, recorded by each frame, already had a square geometry. The dimensionality in the z-direction, was given by the distance the laser moved, per time interval, between frames. It was therefore desirable to configure the velocity of the laser so that this distance matched that of the dimensions of the imaged pixels, in the object plane. The coordination of the velocity of the camera with that of the laser, through the refractive index, ensured that the magnification in the xy-plane remained constant. To preserve the same scale in the z-direction, the laser needed to move with a constant velocity given by the relation

$$v_{laser} = \frac{framerate \cdot pixel\text{-}dimension}{magnification}. \tag{3.1}$$

The frame-rate was set in the camera settings. For the work done in this thesis, 29.97 FPS was used.

The sensor of the camera measures 15.6 mm x 23.5 mm [84], and at the resolution used, standard HD, there are 1920 pixels in the y-direction, which is the longest, as the camera is tilted vertically. In the x-direction the image is cropped, so the entire sensor area is not used (the sensor has a resolution of 6000 x 4000 px, the 1920 x 1080 px resolution of the HD standard requires reprocessing, in the camera). The pixel dimension then comes out at 12.2 µm.

To complete equation (3.1), it was necessary to have a measure for the magnification. The magnification of a lens is a function of the distance to the object. It can be determined by equation (2.56). The problem here lies in that the camera object used is not a single thin lens. To use the equation one must determine where the "lens" is, to be able to measure distances from the object to the lens, and from the image plane to the lens. To work around this problem, the camera, laser and sample cell were put in predetermined starting positions. For a given sample cell size, the magnification would then remain constant and thus remove the need for an approximation of the magnification, based on measuring the distances. To determine the magnification, the camera, laser, and cell, were put in position, the cell was filled with rapeseed oil, and a ruler was put in the sample, with the scale-bars centered on the laser sheet. A brief movie-clip was then shot; the result can be seen in figure (3.10). Rendering a calculated dimension of 52.55 µm per pixel and by equation (2.56), a magnification of

$$\gamma = \frac{h'}{h} = \frac{12.24\mu\text{m}}{52.55\mu\text{m}} = 0.23. \tag{3.2}$$

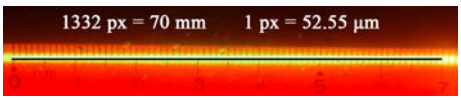

Figure 3.10: *Screen shot of the ruler imersed in oil in the sample cell. I measured how many pixels 70 mm corresponded to, at the plane where the laser sheet hit.*

The scan velocity was then calculated by inserting into equation (3.1),

$$v_{laser} = \frac{29.97 \text{ s}^{-1} \cdot 12.24 \text{ µm}}{0.23} = 0.158 \text{ cm/s}. \tag{3.3}$$

The camera velocity can then by calculated from equation (2.60)

$$v_{camera} = \frac{v_{laser}}{n_i} = 0.105 \text{ cm/s}. \tag{3.4}$$

3.1.9.1 Verification of the scan geometry

To verify that the laser moved with the velocity as specified, a mobile phone was put on the sled, and used to film down on the ruler, taped to the linear actuator rail. The sled moved 4.00 cm in 28.09 seconds, and the phone filmed with the same frame-rate as used in the scans, 29.97 fps, meaning that it moved 47.47 µm per frame. Frames from the clip can be seen in figure (3.11).

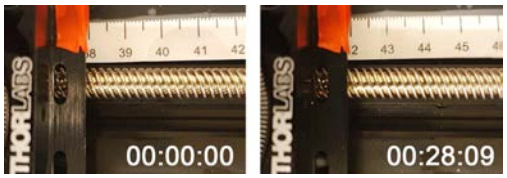

Figure 3.11: *Screen shots from the clip shot by the mobile phone on the sled of the laser. The sled moved 4.00 cm in 28.09 seconds, putting the actual laser velocity at* $v_{laser} = 0.142$ *cm/s.*

This velocity is not conforming with the intended programming of the scan code, meaning that something was miscalculated in the script, but verification proved the velocity to be persistent. As this test was done after the flow experiments, the recorded voxel geometry, in the recorded data, is as specified in table (3.3), with the x and y dimensions as calculated in section (3.1.9).

Table 3.3: *Voxel dimensions for the recorded data.*

Direction	Voxel dimension
x	52.6 ± 0.5 µm
y	52.6 ± 0.5 µm
z	47.5 ± 0.5 µm

3.2 Experiment: 3D flow regimes in gravity unstable invasion

To test the capabilities of the scanner, and learn about the dynamics of the chosen fluids and medium, many trial experiments were run. There was no systematic recording of data, but rather multiple, rapid trials, with minimal preparation and deliberation. In such a manner some of the characteristics, both of the scanner and the flow dynamics were uncovered.

After this trials, a first experimental approach was decided on. The set up allows for both static and deformable media, but to start with the most simple case, it was decided to run an experiment with a static medium. It was chosen to look at the pattern regimes with glycerol injected at fixed flow-rates from the top, into a medium made of loose, randomly packed, 3 mm borosilicate glass beads, locked in place in a static matrix, and saturated with rapeseed oil. The pressure was to be held constant at the outlet.

Based on test experiments, the injection rates were set to 0.1 ml/min, 0.5 ml/min and 5.0 ml/min.

To get comparable data, the experiments were defined to start at the moment when the invading fluid entered the cell, and end at the moment of percolation, meaning when the invading fluid reached the bottom of the cell.

The invading fluid, glycerol, is both denser and more viscous than the defending fluid, rapeseed oil. By expectations based on trial experiments and studies conducted in 2D, this should give a broad front, with fingering, for the slow rate, and a more narrow front, and more stable displacement, for the faster rate [40–43, 45]. See section (2.3.16) for a brief treatment of the reference studies.

The experiments had two primary goals. Primarily we wanted to asses the quality of the gathered data, and thus the scanner and experimental methods. Secondly, the matter at hand has, to our knowledge, never been investigated in 3D, and could very well produce results suited for publication.

3.2.1 Preparation of the fluids

The fluids used were 2 liters of rapeseed oil, from 2 x 1-liter bottles, of brand Eldorado, and 2 liters of Glycerol, from a 5-liter bottle, of brand VWR. The fluids were poured into separate 5-liter bottles, and a 100 ml container was drawn from each.

Into the 100 ml containers, 50 mg of fluorescein 548 was mixed with the glycerol, and 50 mg of pyrromethene 650 was mixed with the rapeseed oil.

From the concentrates 80 ml was mixed into the glycerol, putting the final concentration at 20 mg/l, and 60 ml was mixed into the rapeseed oil, giving a concentration of 15 mg/l. The fluids were then poured into 1-liter bottles for storage.

3.2.2 Measurements of fluid properties

The physical properties of the fluids used in the flow experiments are of vital importance in any interpretation of the dynamics found. Some of the measurements done, such as the density and viscosity, follow procedures well established in PoreLab, and the findings inspire confidence and are presented with well-funded margins of error. The measurements of surface tension and wetting properties are slightly more ambiguous, as they have been performed with a new machine that we have rather little experience with. As the main focus of the experiments was testing the scanner itself the measurements of fluid properties must as of yet still be considered to be incomplete, in particular, we have yet to develop a model for error in the surface tension and wetting angle measurements, these are therefore presented as is. This topic is elaborated more extensively in chapter (4).

3.2.2.1 Densities

The densities were found by weighing a strictly known volume of the liquids. A specially designed container, a so called *pycnometer*, with a known volume of 51.017 ml, was filled and weighed. The procedure can be seen in figure (3.12), and the results are presented in table (3.4)

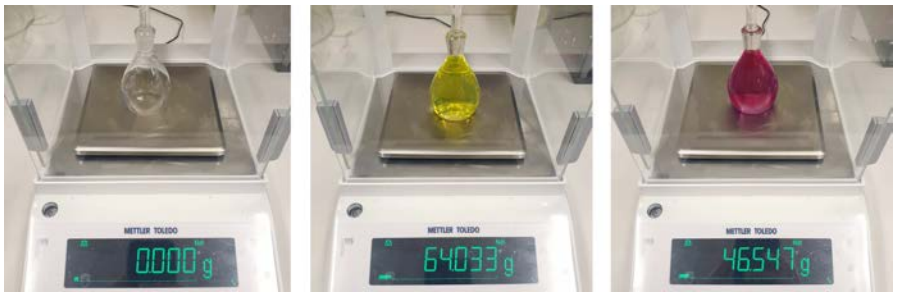

Figure 3.12: *Density measurements, with margins of errors established from the fluctuations in the fifth significant figure on the digital scale.*

Table 3.4: *Fluid densities.*

Medium	ρ (density)
Glycerol	1.255 ± 0.002 g/ml
Rapeseed oil	0.912 ± 0.002 g/ml

3.2.2.2 Viscosities

The viscosities were measured, using a viscometer, see figure (3.13) for an understanding of the procedure. For the glycerol a Lauda, type III viscometer, with constant $C = 1.0204$, was used. Seven measurements were made, with a mean measured time of $t = 751 \pm 4$ s. For the rapeseed oil a Lauda, type II viscometer, with constant $C = 0.11127$, was used. Seven measurements were

made, with a mean measured time of $t = 575 \pm 3$ s. The results are presented in table (3.5).

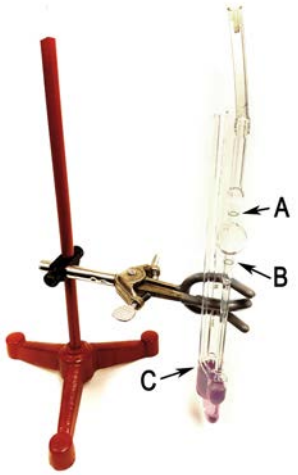

Figure 3.13: *Measurements with a viscometer. The fluid is injected into the viscometer so that the liquid reaches the level C. The liquid is then pulled up by a syringe connected to the left tube, pulling it past the level A. The liquid is then released by disconnecting the syringe. The time, t, it takes the interface to go from level A to level B, is measured. The kinematic viscosity is found by the relation $\nu = Ct$, where C is a constant, specific to the viscometer.*

Table 3.5: *Fluid viscosities, with margins of errors calculated from the standard deviation in the mean of the measured time periods.*

Medium	ν (kinematic viscosity)
Glycerol	767 ± 4 mm^2/s
Rapeseed oil	64.0 ± 0.3 mm^2/s

3.2.2.3 Surface tension

In figure (3.14) a drop shape analyzer, from Krüss, can be seen. It was used to determine the surface tension between the glycerol and the rapeseed. To make the measurements, the machine makes live image analysis of a close-up image of a drop, hanging from a syringe tip, and fits a Young-Laplace equation (equation (2.10)) to the drop shape.

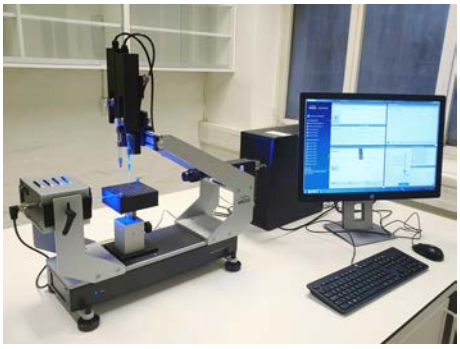

Figure 3.14: *The rig for measurements of surface tension and wetting angles. It is a drop shape analyzer, manufactured by Krüss, fitted with a syringe-based system for drop formation and a high-speed macro camera, connected to a computer, for real-time geometric analysis.*

To give the measurement scale, the diameter of the needle tip is measured with a caliper. The machine takes as inputs the fluid densities, the image of the drop, as well as an input of measurement of scale, in the form of a bar dragged across the needle tip with the mouse, and the corresponding needle diameter typed into a box. To measure the surface tension between the two fluids, the needle tip, connected to a syringe with one fluid, was lowered into a small basin containing the other. As the rapeseed is less dense than the glycerol, a special needle, curved up again like a U, was used to form a drop of rapeseed oil in the glycerol. As the two fluids are index matched, the created drop was invisible in the first attempt. To counter this, nigrosine was mixed into the glycerol to form the drop, surrounded by rapeseed oil as used in the experiments. The rapeseed drop was made from a concentrate with pyrromethene, surrounded by glycerol as used in the experiments. To ensure that that the added dye did not affect the surface tension, measurements of the surface tension against air were made, both the regularly dyed liquids, as used in the flow experiments, and the more concentrated ones, as used for the fluid against fluid measurements. The measurements showed negligible deviations with the more dyed drops. In figure (3.15), screenshots from the software used can be seen, with a presentation of the results in the images.

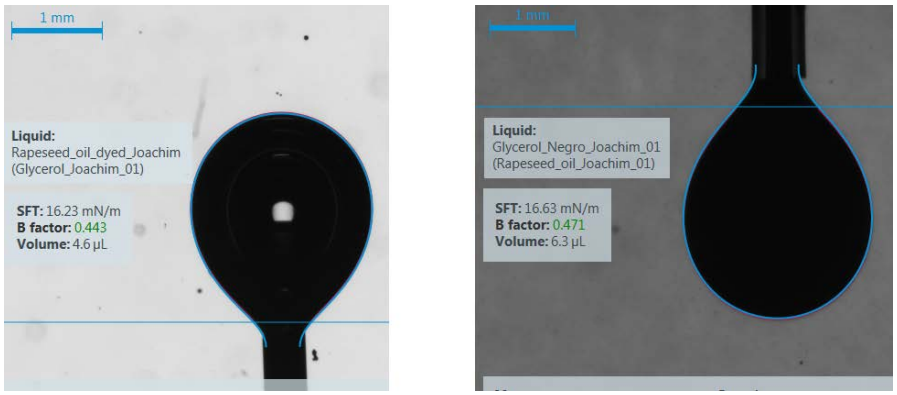

Figure 3.15: *Surface tension measurements; on the left, a drop of rapeseed oil, surrounded by glycerol, and on the right, the inverse. As can be seen the measurements were in good agreement, with results* $\gamma_{r\ in\ g} = 16.23\ mN/m$ *and* $\gamma_{g\ in\ r} = 16.63\ mN/M$

The machine used for the measurements offers several approaches to measuring the surface tension. The method used is called *pendant drop* and fits the Young-Laplace equation to a *drop shape analysis*. The shape is automatically recorded by digital imaging and processing, but the fitting can be manually tuned, by dragging the horizontal blue lines in figure (3.15)up and down. The measurement quality is reflected in the $B - factor$ (as shown in the figure) when it is green the fit is considered adequate. As the pressure difference in the fluids is proportional to the imputed densities, the geometrical analysis, along with the calculated $B - factor$ allows for solving the Young-Laplace equation for the surface tension, γ [85].

3.2.2.4 Wetting properties

The drop-shape analyzer, used in section (3.2.2.3), also has a functionality to measure wetting properties. To derive the wetting properties of our two fluids, in combination with borosilicate glass, a shard of the same material was put in the measurement container. The needle was lowered into the frame, the scale was calibrated by typing in the needle diameter, and a drop of glycerol was created, large enough to disengage from the needle and drop down on the glass beneath. In figure (3.16), we se screenshots from the measurements, and figure shows (3.17) a chart of the evolution of the drop during of the measurements.

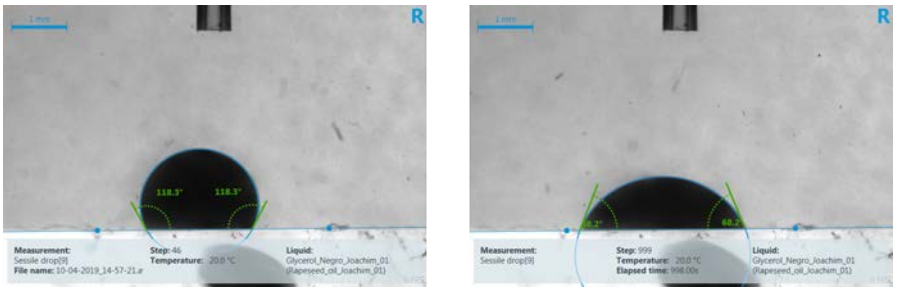

Figure 3.16: *Wetting-angle measurements at two different times. To the left, the drop has just reached the surface, while to the right, 16 minutes have elapsed.*

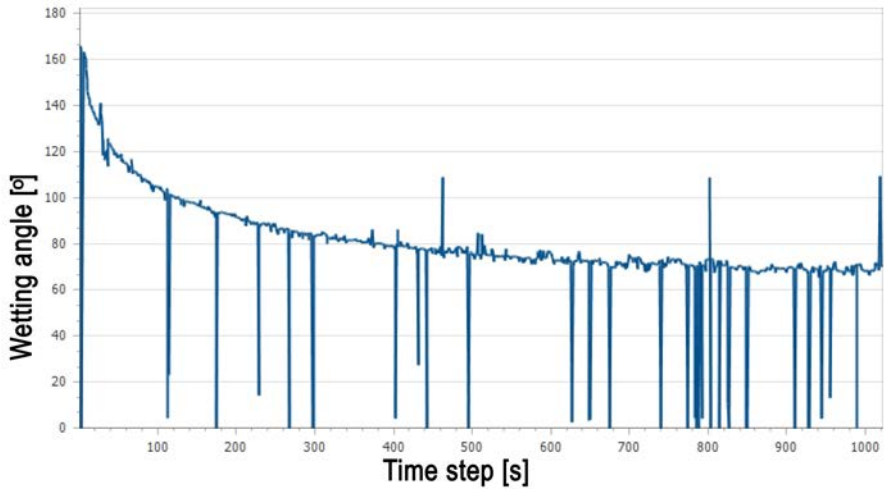

Figure 3.17: *Wetting-angle measurements from the first 16 minutes after the drop formed on the surface. There is one time-step per second on the x-axis. The vertical spikes are artefacts, as the measuring algorithm occasionally fails to interpret the image data.*

The measurements of a drop of glycerol immersed in rapeseed oil on borosilicate glass indicate a not constant wetting angle. In a time-frame relevant to the experiments the angle converges at about 70 °, in the domain referred to as

neutrally-wetting or *intermediate-wetting* [86]. Figure (3.18) shows close-ups of the fluid-fluid interfaces form trial experiments with the fluids and medium. The pictures show how the two phases alternate in assuming the wetting or non-wetting role, from which it can be concluded that the combinations of fluid and medium fall under what is referred to as *dynamic wetting* [87, 88]. It should therefore be concluded that the terms *drainage* and *imbibition* are not suited to characterize the flow (see section (2.3.5)).

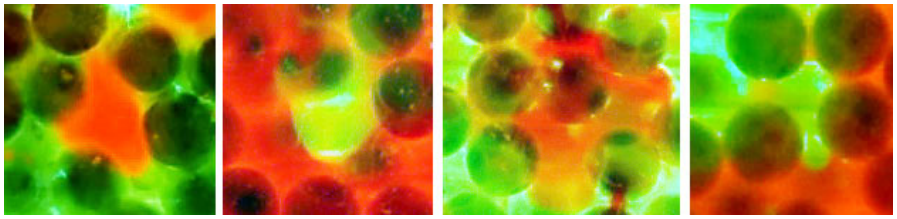

Figure 3.18: *Close up of frames from trial experiments with the used fluids and medium. The last two pictures are actually close ups from regions of the same image. In this test, the buoyant rapeseed oil (red) was injected from the bottom. It seems that the soaring rapeseed assumes a non-wetting shape as it displaces the glycerol. In the last image, a trapped cluster of glycerol is making its way down, here the glycerol appears as non-wetting.*

3.2.3 Installation of the pressure sensors

The pressure sensors were 26PCAFG6G Honeywell Pressure Sensors. They were wired and connected according to the manufacturer's data sheet. The sensors are of a flow-through type, see figure (3.19). They have four connection points, two for an applied operating voltage, specified at 10 V, and two for voltage readings, corresponding to the pressure in the flow-through chamber. To correctly interpret absolute pressure they must be calibrated. As the purpose of including the sensors was to get preliminary ideas of how such readings could be interesting, this has not been done. The correction factor provided from the manufacturer was used to get a baseline for relative pressure readings.

Figure 3.19: *Picture of the type of pressure sensor used, from the manufacturers website [89].*

3.2.4 The flow experiments

The experimental set-up can be seen in figure (3.20). The procedure was the same for the three flow rates and will be described as one. Each experiment was conducted in one day and took about eight hours, including preparation and cleaning.

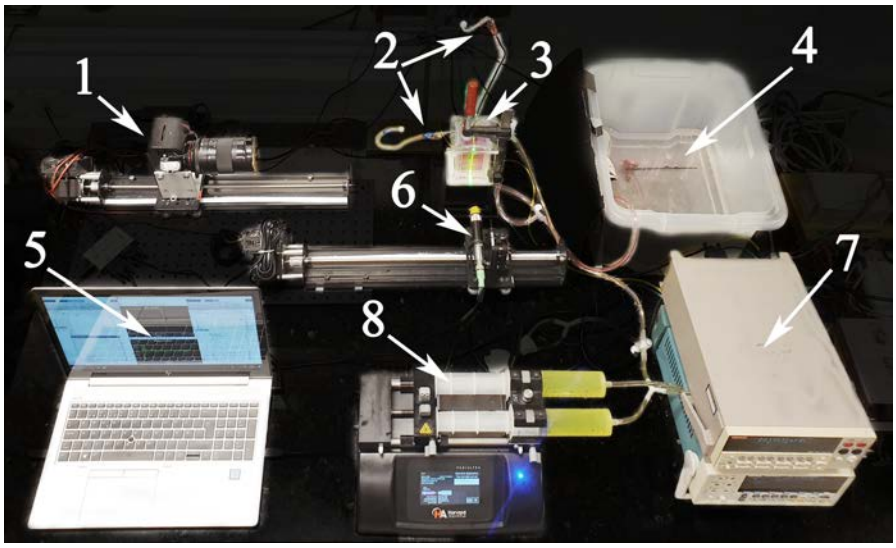

Figure 3.20: *The set-up in the lab, for the flow experiments. 1. The camera; mounted on a linear actuator, 2. The pressure sensors; connected with the injection and outlet tubes, 3. The flow cell, 4. A large surface outlet basin, 5. The computer; controlling the actuators and reading pressure data, via the multimeters, 6. The laser; mounted on a linear actuator, 7. The multimeters; reading the pressure sensors, 8. The syringe pump; for controlled injection*

3.2.4.1 Preparations

Before each experiment, the cell had to be set up anew. The beads, cell, tubes, and syringes were cleaned and reused. Trial and error revealed that preparing the sample cell and flow tubes required deliberate and precise execution. It was imperative that no air remained trapped anywhere in the system, that all connections were properly sealed and that the flow cell was saturated entirely with the defending fluid, while the tube from the syringe pump was filled with the invading fluid

The cell was put on a massive aluminum base, with the shape of a toppled U, allowing for the outlet tube to pass out. A tube was attached to the bottom valve of the cell and inserted into an empty bottle at the other end. The cell was then half filled with the defending fluid, and the bottle was held under the table, to fully fill the outlet tube and leave its tip submerged in the bottle. The bottle was then put on a vertically adjustable stage, and was used to regulate the fluid level in the cell.

Glass beads were poured slowly into the fluid. With the rising level, a metal spatula was used to stir out air bubbles. When the fluid and beads reached about 1.5 cm from the top, the metal plate and spring, seen in figure (3.4), was put onto the matrix.

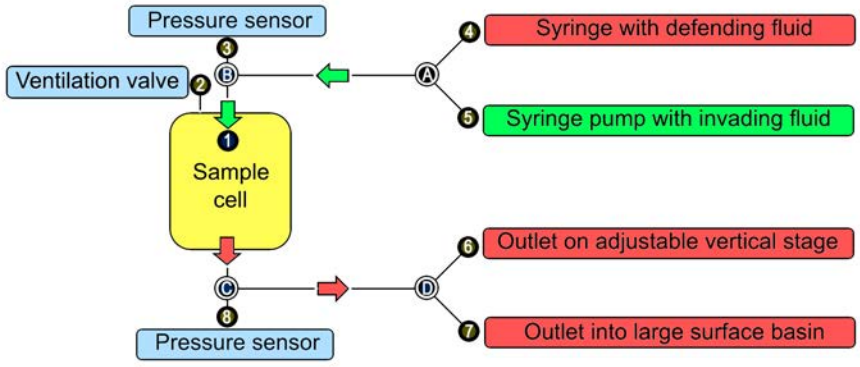

Figure 3.21: *Diagram of the tube connections. The letters A-D represent 3-way valves and the numbers 1-8 are components connected via tubes. For this experiment, the injection tube was connected to the valve at the top of the cell, and the outlet tube went out from the valve at the bottom.*

Figure (3.21) shows a schematic diagram of the flow component and tube connections. Two 140 ml syringes were filled with the invading fluid and attached via a y-connection to the inlet tube. The syringes were then mounted in the syringe pump (5). A 50 ml syringe (4) was filled with the defending fluid. A 3-way valve (A) joined these with the inlet tube. Another 3-way valve (B) connected the pressure sensor (3) to the tube, which finally was connected to the inlet valve on the lid of the sample cell (1).

The groove on the lid was filled with high-vacuum silicone grease, to seal the sample.

The tube leading through the pressure sensor (3) was flushed with the invading fluid and sealed off at the end. The valve (B) was then turned to cut off the pressure sensor, and the tube was flushed with the defending fluid. This turned out to be necessary, as there was no way to get the invasion nipple into the sample without a drop of air coming along. To avoid this, the nipple was barely submerged in the cell, stranded air was flushed before the nipple was inserted into the matrix, then the lid was pressed down and clamped on. This had to be done with the defending fluid in the injection tube, to avoid getting any of the invading fluid into the cell. Trapped air under the lid of the sample was evacuated via the ventilation valve (2) (seen in figure (3.4)) by raising the bottle connected to the outlet (6), until the air had escaped and then sealing the flushed tube.

The adjustable outlet (6) was then disconnected at (D), while the outlet basin

⑦ was patched in. The basin was half-filled with water, and the outlet tube was submerged, pinned at the bottom by an attached weight. The outlet basin had a surface of approximately 1500 cm^2, meaning that a complete replacement of the about 250 cm^3 of defending fluid, by invading fluid, would lead to a rise of approximately 1.7 mm, and thus a maximum pressure rise of about 17 Pa (by approximating the fluid density to that of water). The purpose of this solution was to maintain a quasi-stable pressure at the outlet [2].

The syringe with the defending fluid ④ was then shut out, and the invading fluid was driven by the syringe pump ⑤ to the point, where the interface was poised to invade the cell. The pressure sensor was re-included in the circuit with valve Ⓑ.

The syringe sizes and injection rate were programmed into the syringe pump ⑤. The pump was reset, so as to start the measurement of injected volume, at zero.

To correlate the data recorded on the memory card, in the camera, and the pressure voltage readings from the pressure sensors, in the computer, the clocks in the camera and the laptop were synchronized.

The sample cell, camera, and laser were set in the initial positions, with the laser sheet traversing through the center of the cell, passing right over the inlet and outlet valves.

The scanning script and pressure sensor script were initialized and checked.

The camera was set to record video, with the settings as listed in table (3.6), and the focus setting was verified.

Table 3.6: *Camera settings for the recorded data.*

Parameter	Setting
Mode	Video
Resolution	1920 x 1080
Frame rate	29.97 FPS, progressive
White balance	5500 K
ISO	1250
Shutter speed	1/30 s
Aperture stop	f/2.8

The lights in the room were turned off.

[2]Here it should be noted that it was a mistake to fill this basin with water and not the defending fluid. Capillary effects, as drops of displaced fluid were pushed out of the tube into the water basin, might have lead to feedback pressure-waves, which in turn may have affected the experiment.

3.2.4.2 Conducting and recording the flow experiments

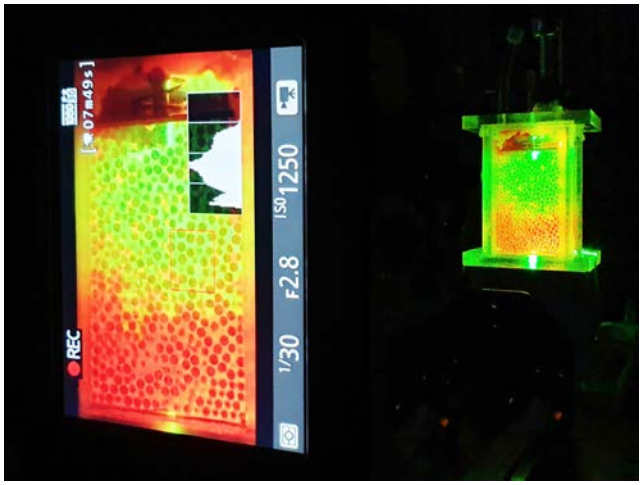

Figure 3.22: *View from behind the camera, during the 5 ml/min experiment.*

Before starting the syringe pump, the pressure sensor readings and camera recording were initiated. The camera was set to record continuously.

A scan of the initial condition was conducted.

The syringe pump was started, and scans were conducted with 5-minute intervals. Between scans, the center cross-section of the sample was observed and recorded. A picture from the 5.0 ml/min experiment can be seen in figure (3.22).

The time and syringe pump reading, as the invading fluid reached the bottom, were noted, and a scan was performed. The initial data from the three experiments can be seen in table (3.7). In figure (3.23) the center slices, at approximately the percolation moments, can be seen.

Table 3.7: *Data from the flow experiments. The large margin of error is due to the fact that only one 2D slice of the sample can be observed at any given moment, and it is thus not possible to determine the percolation moment precisely, unless the the fluid reaches the bottom in the plane coincidentally observed.*

Injection rate	Percolation time	Injected volume
0.1 ml/min	38.5 ± 1 min	3.85 ± 0.10 ml
0.5 ml/min	28.5 ± 1 min	14.3 ± 0.5 ml
5.0 ml/min	15.0 ± 1 min	75 ± 5 ml

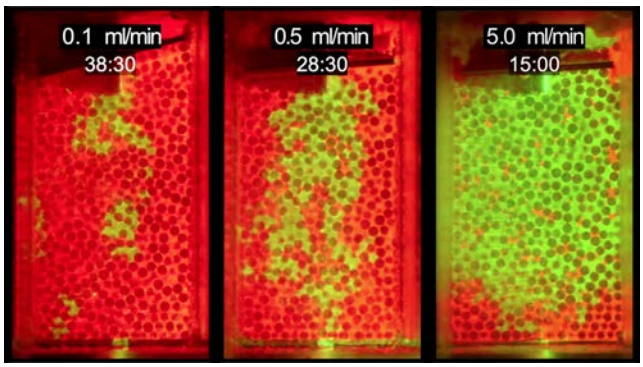

Figure 3.23: *The percolation moments.*

3.2.4.3 Readings from the pressure sensors

Initially, there were pressure sensors, connected both to the inlet and to the outlet. Each sensor was fed by a power supply, set at 10 V, the pressure was then read off as the voltage by a separate multimeter, that in turn was read off by the computer. There were problems with the readings from the top sensor. After a while, the script reading the multimeter would crash. Unfortunately, the data from the top sensor was deemed to be of greatest interest, as the outlet at the bottom was intended to be kept at a constant pressure.

During the experiments, I figured out that the problem lay with one of the multimeters and its communication with the computer, so for the last two experiments (the slowest and fastest), the top sensor was connected to the working multimeter, and the bottom one discarded. The readings from the pressure sensor, connected to the inlet, in the 0.1 ml experiment (conducted last) can be seen in figure (3.24).

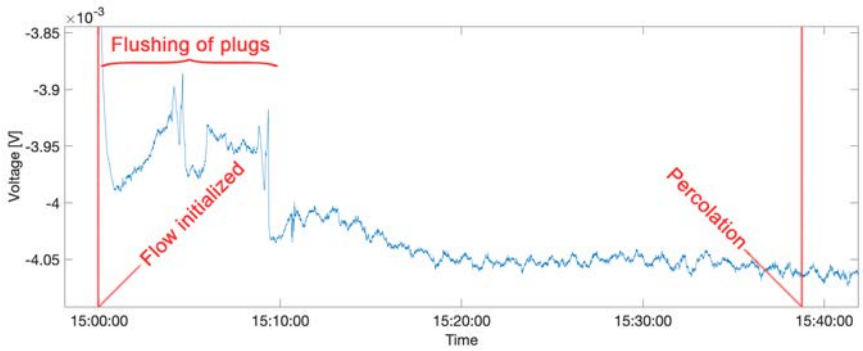

Figure 3.24: *From the 0.1 ml/min (slowest) experiment. Voltage readings over the pressure sensor, connected to the inlet valve at the top of the sample cell. The invading fluid is poised to enter the cell as the flow is initiated, marking the beginning of the experiment. The pressure data is explored further, with the voltage converted to relative pressure units, in section (4.2.2).*

The period referred to as *flushing of plugs* must be interpreted in relation to the properties of the valve and tubing at the inlet. The dimensions of the valves and tubes were not small enough for interface boundaries between the fluids to form unbreakable barriers. Even with the pump inactive, there were dynamics. The more buoyant defending fluid would start climbing up the inlet valve, displacing the invading fluid. This was not so much a problem for the faster experiments, as these dynamics were very weak compared to that from the syringe pump, but in the slowest experiment it was a factor. To initialize the experiment correctly the valve at the inlet was kept shut until the very last moment, this created the elevated pressure seen at the beginning, as the valve was opened dynamics occurred in and around the inlet valve until this somehow stabilized and the pressure dropped. This is treated more extensively in chapter (4).

3.3 Image analysis and rendering of a 3D-model

The development of a workflow for image analysis and 3D-rendering has gone alongside the work in the lab throughout the entire project period. Also here there was much trial and error, and many discarded attempts are not presented here.

3.3.1 The raw data

The data recorded by the experiments consists of RGB movie clips, of resolution 1920 x 1080, compression format Linear PCM, H.264 and FPS=29.97, from the camera, and of a list of voltage readings, with a corresponding list of time-codes, from the pressure sensor. In figure (3.25), the video-data is illustrated.

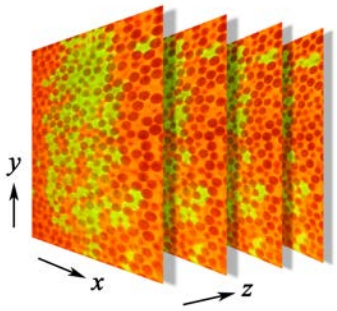

Figure 3.25: *Frames from the video-data. The volume rendering axes are represented by the arrows.*

In figure (3.26), a close up of a frame can be seen. By this method information about the image channel values was collected. The blue channel was inactive in the images, so only the red and green were of concern. The oil (red in the picture) had red channel values 220-254, and green channel values 33-119, the beads (dark, red patches) had red channel values 122-222, and green channel values 19-67 and the glycerol (green) had red channel values 148-167 and green channel values 96-232. Also, a method was used to detect the disk shapes in the frames, and thus localize the beads.

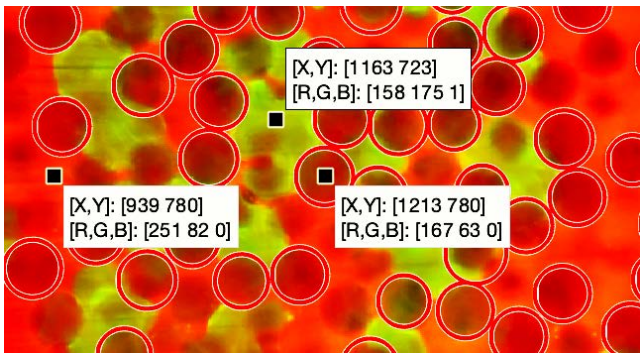

Figure 3.26: *Section of a frame, with data points from Matlab. The points give the coordinates and red, green and blue channel values (from 0 to 255), at the point. The red circles signify disk shapes, detected with the imfindcircles command in Matlab (a function to detect disc-shapes in a 2D image, based on a method called the Hough transform).*

During the testing and development of the scanner, various methods for image analysis and volume rendering were probed. In figure (3.27), an example of a volume generated in Matlab can be seen. This served well to verify that the method was viable, but the results were crude, and the manipulation was slow. Conceivably it could have worked better, with an optimized computer, or another application.

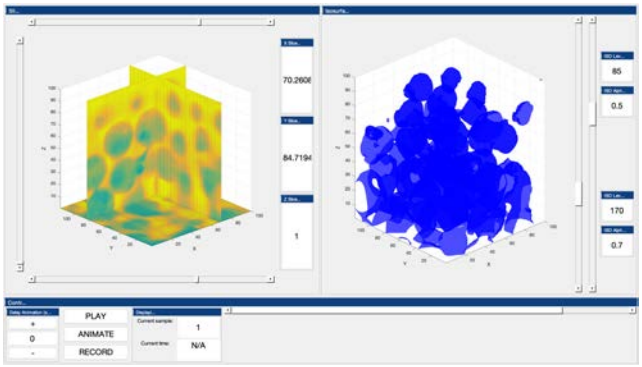

Figure 3.27: *Preliminary investigation in Matlab. Here there is only one liquid phase and the visualization tool was very slow and crude, but it gave some idea as to what could be achieved.*

3.3.2 Using Avizo from Thermo Fischer

The final data analysis and 3D-rendering were conducted using *Thermo Scientific Amira-Avizo*, from Thermo Fischer.

From the manufacturer's web page: *Thermo Scientific Amira-Avizo and Pergeos Software are the leading high-performance 3D-visualization and analysis solutions for scientific and industrial data. Wherever 3D-imaging data sets need to*

be processed, Amira-Avizo and Pergeos Software offer abundant state-of-the-art image data processing, exploration and analysis features within an intuitive workflow and easy-to-use graphical interface.

The software is a potent tool that requires a powerful computer. The geophysics group which shares the same floor as Porelab at the University of Oslo has had an Avizo computer lab for some time already, and the responsible professor, Francois Renard, gracefully let me use the lab for the analysis and rendering.

The work station used has an Intel Xeon(R) 2.3 GHz CPU, 128 GB RAM, and a dedicated graphics card from Radeon. The configuration was barely adequate for the performed processing. During the first phase of the processing, the rig was stable and dependable, but after an update to the operating system the platform became unreliable, and crashes were quite frequent. This was in particular frustrating due to the sheer data volume ($\sim$100 GB) that had to be reloaded into the memory after a reboot. For continued work this is something that must be dealt with.

Before importing the data into Avizo, the movie clip had to be converted to single-frame TIFF files. This was done with Adobe Photoshop. Avizo processes either grayscale or binary data, each channel from the original data was handled separately, but it is possible to perform cross-channel operations, such as algebraic operations between the channels, or comparisons. The program is very extensive, and as of yet, I have only scratched the surface of the capabilities, especially concerning data analysis and simulation. The work-flow was improvised, through trial and error, but after several attempts, a convincing procedure was established.

There were three separate phases to localize: the spherical glass beads, the defending red rapeseed oil, and the invading green glycerol. The procedure followed these main steps; finding the coordinates of the mass centers of the beads and generating binary spheres there, separating the green from the red and creating binary bodies, and finally subtracting the beads from these volumes. Once each phase was separated into a binary volume, data analysis could be conducted, and volumes could be rendered for visualization. In the following, the various steps taken are briefly outlined.

3.3.2.1 Importing the raw data

A new project is initiated and the import data tab is chosen. The image files are marked and selected. A series of choices and tabs are filled out, to specify that all three channels are to be imported, crop out the relevant regions of the images, and to specify the spatial dimensions of the voxels. For the data processed from the flow experiments, each scan consisted of 875 frames, with the region of interest, in each frame cropped down to 870 x 1420 pixels, resulting in about 1.1 billion voxels ($\sim$1 GB of data per channel).

3.3.2.2 Grayscale processing

Before segmenting the phases, the image data had to be optimized. This was done in two different branches, one for the porous medium, and one for the fluids. The first step was to utilize the channel values in the red and green channel (the blue channel was nearly dead, containing no relevant data), to enhance the desired separation, by performing algebraic operations with the two channels. Then followed noise removal, removal of intensity gradients, contrast homogenization and finally equalization. The filters used were the following:

- **Arithmetic** - this function allows for algebraic operations between up to three channels. To localize the beads, the mean of the red and green channels was calculated. To separate the fluids, the red was subtracted from the green, with a normalization term. This goes back to the considerations around figure (3.26), as the areas with had very low values in the green channel, this procedure greatly accentuated the contrast between the different liquids.

- **Background Image** - calculates an average intensity over larger, overlapping segments, and uses it to render a gradient map that can be subtracted from a channel to create a gradient-free volume.

- **Gaussian Filter** - also known as low pass filter. The highest spatial frequencies are removed with a specified Gaussian profile, removing small specks and unwanted lines from the image data.

- **Adaptive Histogram Equalisation** - the image contrasts are homogenized, imposing a similar contrast range section by section to the frames in a plane. The filter can be applied to several planes in sequence, thus making the whole volume similar in contrast. This filter was suitable in localizing the beads, but not the fluids, as they were rendered as equal, by the filter.

- **Brightness-Contrast** - this filter can be used to optimize the dynamic range and normalize the channel histogram.

3.3.2.3 Segmentation

Avizo offers several segmentation methods, the simplest one, interactive thresholding, was used for the analysis.

- **Interactive thresholding** - this filter takes a grayscale volume as input and segments out a fraction, as a binary volume. The fraction is evaluated as an interval in the intensity range. For the segmentation of the beads, values less (dark areas) than a certain threshold were kept, whereas to separate the green glycerol (bright areas) values above a threshold were kept.

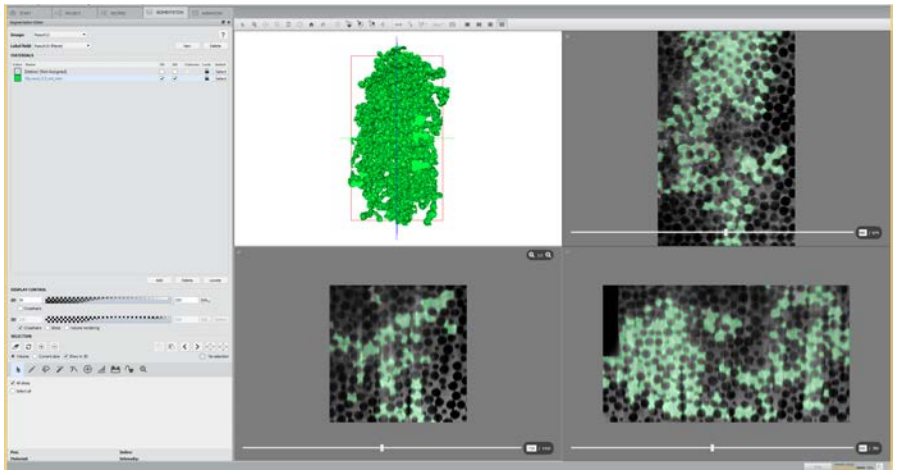

Figure 3.28: *The segmentation module. Automatic and manual methods can be used to separate the various phases. The segments can be named and labeled with a color by choice. Here, the green glycerol is segmented out.*

In figure (3.28), a screenshot from the segmentation module of the software can be seen. Various methods can be tried out, and the results can be verified real-time, as illustrated in figure (3.29)

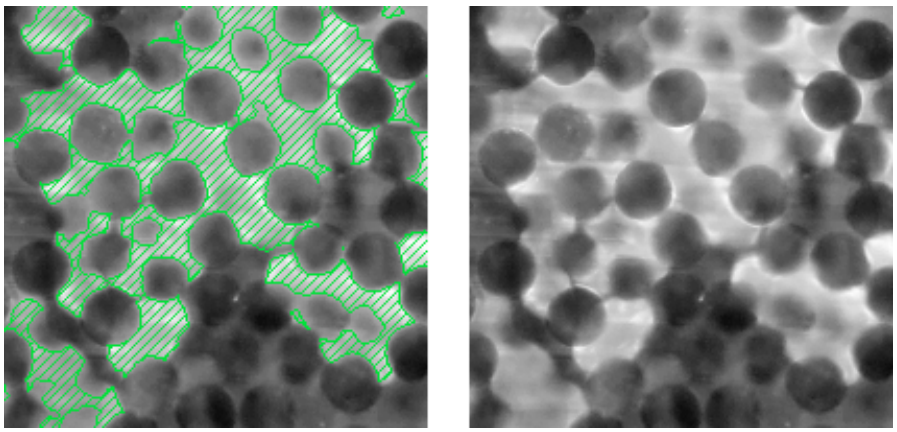

Figure 3.29: *Close-up from the inspection window. On the left, the brighter sections, after various functions and filters, have been segmented out and are marked as green, over the original channel data. On the right, we see the same segment, without the green markings.*

3.3.2.4 Binary processing

After the phases are separated, further processing is applied, to refine the volumes by smoothing over rough interfaces and removing small spots and small holes. In this project, a procedure was used to distinguish the beads, one from another, localize their centers of mass, and use the coordinate map to

regenerate the bead matrix as perfect spheres. Binary processing is also used for functions specific to porous media applications, through the *Pore Network Model* extension. The functions used:

- **Binary Smoothing** - this filter smooths over the surface of the volumes to a specified degree.
- **Remove Small Spots** - volumes consisting of less than a specified number of voxels are deleted.
- **Separate Objects** - the volume is divided into smaller volumes, separated by narrow fissures made where the volume segments are at their thinnest.
- **Label analysis** - the separate volume elements are given a unique value, and a spreadsheet is generated, with data describing the locations and sizes of each element.
- **Pore Network Model** - this is an expansion pack. It contains functions specifically designed for porous media analysis. In this project, the package was used to generate a spreadsheet with the center of mass of each of the detected beads. The pack contains many other features that will be of interest for further analysis. This is expanded on in section (5.0.6).
- **Extract Spreadsheet** - this function gather coordinates for the location of the pores, the pore volumes, their connectivity, and the pore throat areas.
- **Spreadsheet to Point Cloud** - the coordinates from the spreadsheet are used to generate a binary volume, containing single voxels at the locations.
- **Geometry to Label** - much like *Label Analysis*, this feature gives each separate volume a unique value.
- **Dilation** - this function shrinks or expands the separate objects, according to a specified geometry and scale factor. This feature was used to grow spheres of the correct dimension at the point cloud locations. In figure (3.30), we can see how the generated spheres are imposed and replace the detected beads.
- **Invert** - this function inverts the channel value. In the binary case, it turns ones to zeros, and vice versa.
- **Arithmetic** - the same function that was described above. For the binary bodies it was used to remove the bead volume from the segmented green glycerol, and then to generate the red rapeseed volume, by subtracting the beads and the glycerol from the total volume.

3.3.2.5 Data analysis

Avizo offers near endless possibilities for data analysis, as the volumes can be probed through user-made scripts, made in for instance in Matlab or Python, integrated into the software. There is a range of already available analysis

tools, ranging from simple volume calculations to more complex geometrical analysis. The most relevant features are in the Pore Network Model expansion. We did not own this expansion, but I was given a trial license and was able to use the features briefly for the purpose described in the previous section and to extract the Pore Network Model spreadsheets, containing pore locations, volumes, connectivity, and pore throat areas. Calculations of porosities and saturations were extracted and are presented in chapter (4).

3.3.2.6 3D-rendering and visualization

There are many visualization modules, as well as features to render animations. In this project the following modules were used:

- **Ortho Slice** - this feature generates a 2D cross-section in either the xy-, yz- or xz-plane. The slices can be moved through the entire volume and can be set up to traverse, or slice off, rendered 3D-bodies. It is a very useful reference tool during the processing, as it allows for instant verification of the applied filters and functions. In figure (3.30), ortho slices are used to verify the segmentation of the glass beads, as well as the generation of spheres in their place.

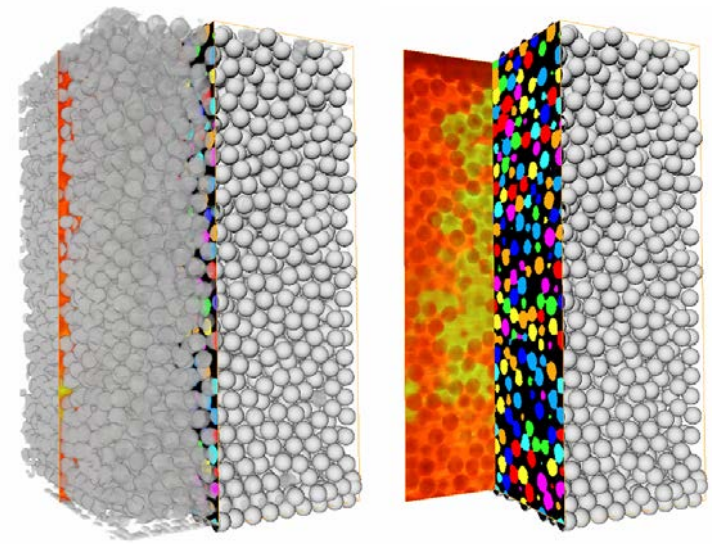

Figure 3.30: *Ortho slices and volume rendering, used in the process to localize and regenerate the bead matrix; the red and green slice is the visualization of the raw data, whereas the black slice is the label field for the localized beads, where each bead has been separated and given a unique value.*

- **Volume Rendering** - this is the main tool to generate 3D-visualizations. The module takes a RGB, grayscale or binary volume as input and renders the volume according to settings, such as color range and opacity. In this project, the binary, segmented phases were rendered by using their coordinates to cut out volumes from the initial grayscale channels. In figure (3.31), a close-up from a volume rendering can be seen.

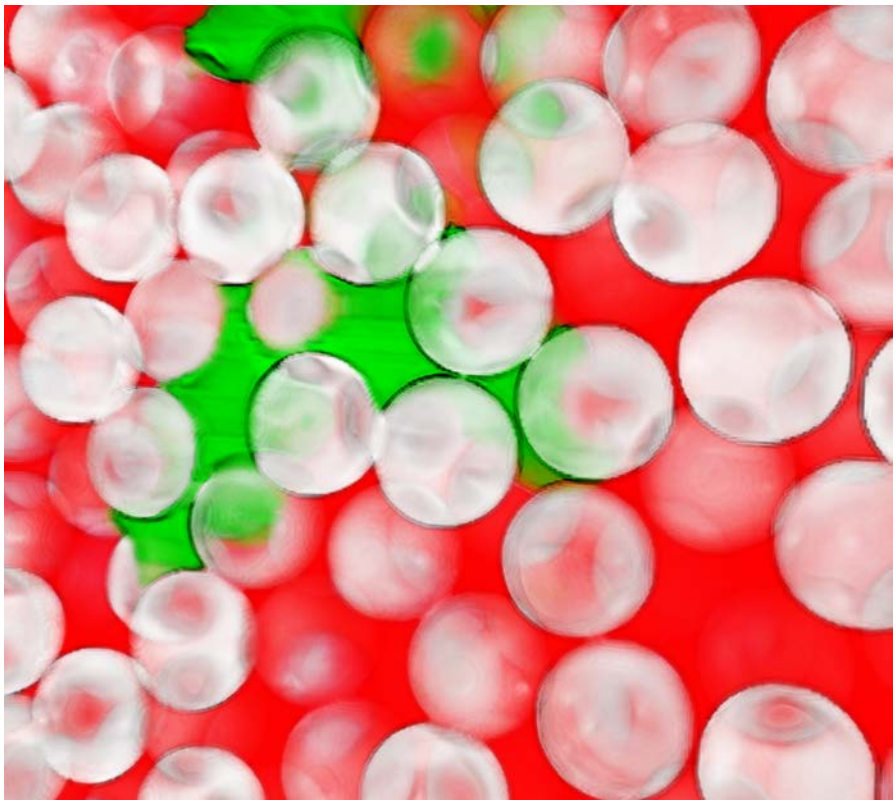

Figure 3.31: *Close-up from a volume rendering of a flow experiment. The spheres are glass beads, the red is the defending liquid, and the green is the invading.*

CHAPTER 4

Results

The goals of this masters project were to develop a functioning 3D-scanner for experiments with flow in porous media, to develop a work-flow for segmentation, rendering, and analysis of the 3D-data, and to conduct a relevant flow experiment, complete with rendering and initial data analysis. The basic outline for the set-up for the scanner was given, in the sense that it would involve index matching medium and liquids, a laser sheet and fluorescent dyes. From there on the road was created as the project progressed.

4.1 The scanner

The scanner development has been quite successful. In figure (4.1) a 3D-rendering, of the raw data from a scan is shown. In its current configuration, the set-up has capabilities as listed in table (4.1). In the following, the capabilities and limitations are outlined.

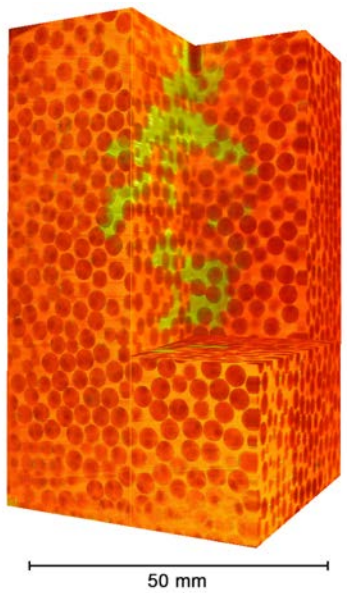

Figure 4.1: *Volume rendering of the raw data, rendered in Avizo, without any image processing or segmentation. A slice of the volume is cut out, to allow a peek inside. The rendering is from the slowest flow experiment. The cell was prepared with rapeseed oil (red) and immobilized glass beads. Glycerol (green) was injected into the cell from the top, at a constant flow rate of 0.1 ml/min. The invasion pattern can clearly be seen, and the rendering offers a convincing localization of the glass beads as well as the two liquid phases, with clear boundaries between each.*

Table 4.1: *Scanner capabilities.*

Parameter	Capability
Sample cell	Up to 100 mm x 100 mm x 100 mm
Scan resolution	Up to 1080 x 1920 x 1080 voxels
Frame rate	10-60 s per frame

In figure (4.2) a close-up of a single bead can be seen, in two orthogonal planes. The investigation offers reasonable confirmation of the rendered geometry and shows the spatial resolution in two planes.

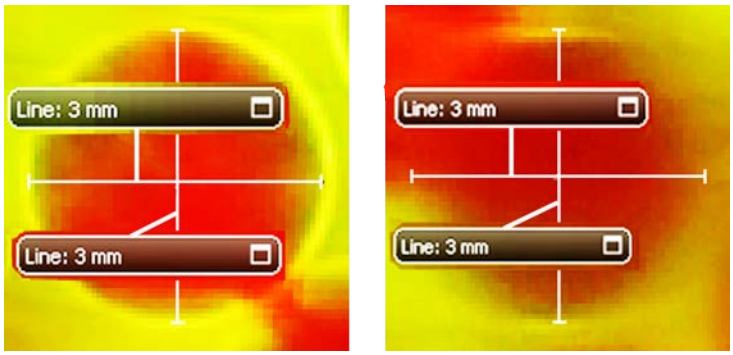

Figure 4.2: *Verification of the scale and geometry of the scan. On the left in the xy-plane and on the right in the yz-plane. The measuring bars are made with a measuring tape tool in Avizo, based on the input voxel dimensions. As can be seen, the contrast rendering is better in the xy-plane, suggesting (as can be seen from a frame of the raw data) that the mapping of the beads is far better near the maximum diameter, where the bead-fluid interface is orthogonal to the image plane.*

The development of an optical scanner for experiments with flow in porous media in 3D was one of the stipulated goals in the PoreLab SFF application. Although the developed scanner has yet to result in publications, several parties have expressed keen interest. The developed platform is a significant step towards establishing a model that could lead to numerous publications, and occupy several researchers for extended periods in the years to come. The scanner development, along with preliminary results, has already been presented prominently, in the 2018 annual reports of both PoreLab and the Njord center. It has also been suggested that the current state of the development of the experimental platform warrants the writing of an article in itself. An example of the type of publications such an article would be *Review of Scientific Instruments*. This is certainly something that I aim to pursue.

4.1.1 Scan resolution

Figure (4.3) lends insight into the level of detail the rig is capable of. In the current configuration, the scan resolution is determined by the maximum resolution of the camera in video mode. There are many video cameras on the market that offer a significantly higher resolution, 4 K (up to 4096 x 3072 pixels), for instance, has become commonplace. There are also drawbacks with increasing the resolution - for a given sensor size, increasing the number of pixels reduces the amount of light per pixel, and thus the dynamic range and a higher resolution means more data to be handled and processed.

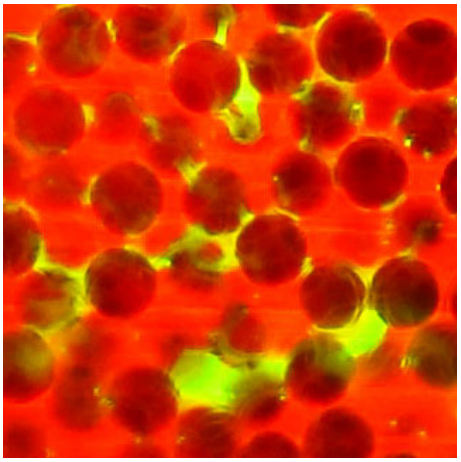

Figure 4.3: *Close-up of a frame from a scan (the glass beads are 3 mm ± 10 % in diameter). The scan is from the day after an experiment. The denser glycerol (green) had been injected from the top, forming a connected invasion pattern. As the cell was left to rest overnight, gravity drove the glycerol down in the sample, leaving behind small clusters and thin coats of film, arrested by the bead matrix.*

The set resolution offers a detail level that scales well with the experiment, coupled with a manageable amount of recorded data. Here, it should also be factored in that the work station needs resources scaled with the scan resolution. The setting used was barely handled by the computer on hand.

4.1.2 Image processing, segmentation and data analysis

Figure (4.4) shows a qualitative verification of the segmented phases. The segmentation is not perfect. Informal inspection reveals that the algorithm misinterprets about 1 in a hundred beads, especially toward the edges of the cell and in the back end of the cell, where the scan quality deteriorates. Locating tiny fluid clusters or thin coating is feasible, but will require more manual corrections in the segmentation, as setting the thresholds to include these also will lead to wrongful classification in the transition regions. As stated, I have barely scratched the surface of the capabilities of the software, more sophisticated schemes for the segmentation can surely be established, and this can thus be improved upon. That being said, the established procedure delivers very convincing results, that should be of more than high enough quality to produce data that can be published. The main challenge to tackle in this lies in generating more comparable studies, so that a model for accuracy, precision and error can be established. More on this in section (5.0.5).

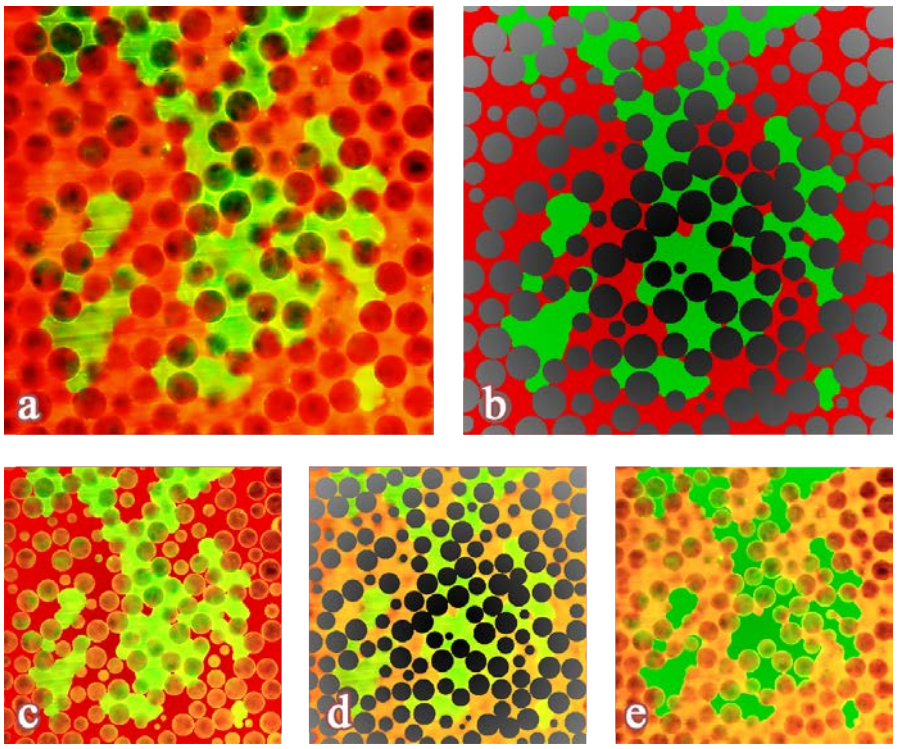

Figure 4.4: *Qualitative comparison of the raw data and the segmented 3D-volumes. The images are made from frames made with the Ortho Slice function in Avizo. All the frames are 2D-slices, in the xy-plane, from the same random location inside the flow cell, from the 0.5 ml/min experiment treated in sections (3.2) and (4.2). a is the untreated raw image data, b is the 3 binary phases as detected and segmented, c is the detected (red) rapeseed oil, laid over the raw data, d are the detected (gray) beads, laid over the raw data, and e is the detected (green) glycerol, also laid over the raw data.*

The work-flow developed in Avizo has proven to be highly successful, rendering convincing segmentation into binary volumes, and quality visualizations at a high spatial resolution. This result makes this project highly relevant in comparison with current work in the field, with rendered images of comparable or higher resolution and dynamic content [46, 90–92].

As the phases are fully rendered as segmented binary bodies, the experimental data is ideally suited for data analysis and comparison with simulations. I believe that the established protocol is an excellent initial step and that further development of these methods will lead to many new findings, fuelling both further experiments and publications.

4.1.3 The sample cell - capabilities and limitations

For the flow experiments, a cell with a base of 50 mm x 50 mm was used, filled with 5-10.000 3 mm borosilicate glass beads. The cell has the obvious limitation that the flow can reach the cell walls when the invasion front is sufficiently narrow, or if a finger branches out wide. At the boundary, the matrix no longer has the same general configuration, the permeability is altered, and the pattern formation is affected. However, the afforded matrix volume should be large enough to cover investigation into a wide range of flow regimes and pattern formations. A solution for an optimized cell has already been thought out and is treated further in section (5.0.1).

The main factor in determining the maximum cell size is the optical properties of the complete sample cell, with medium and fluids. More specifically, the cell size is limited, more than anything, by the index matching. The aim was to find a medium and fluids that were as closely matched as possible. Simple visual inspection of the cell reveals that the fit is not perfect. In figure (4.5) it is clear to see how the image quality deteriorates, as the laser sheet moves deeper into the sample. The image quality is sufficient to record up to 100 mm into the sample, but then with a reduced level of accuracy, compared to a smaller sample size. For optimal image quality, with the current level of index matching, cells up to 50 mm deep should be used.

In the direction penetrated by the laser-sheet (from the right, to the left), there is only a slight loss of intensity. There are gradients, both in light intensity and in contrast, but these can relatively easily be dealt with, through image processing.

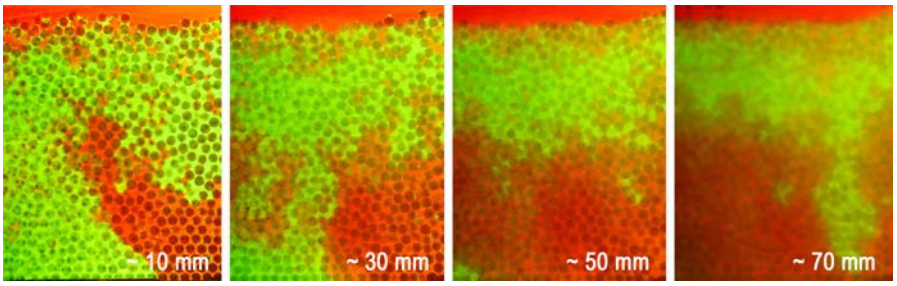

Figure 4.5: *Test with a cell with an 80 mm x 80 mm base. From the left to the right we see frames, as the laser goes deeper into the sample. The depth from the front pane is specified on the images*

An obvious limitation with the current cell design is that the columns at the corners of the cells block for scanning near the glass panes, and thus a part of the volume remains undocumented. This is something that can be improved, by making a cell design where the glass panes are fused, without any supporting structure.

4.1.4 Fluid properties

The fluid properties measured, along with the table values are presented in table (4.2). As can be seen, there are some deviations from the table values. The rapeseed oil is a very complex fluid, containing an unknown number of fats, acids and other organic molecules, as well as minerals. The oil will be unique to the origin of the rapeseed crops and the production facilities [78, 79]. It is not unreasonable to assume that one batch can vary from the other by the margins presented by the gap between the table values and the measurements.

Table 4.2: *Reference values and experimental data for the two fluids, at approximately 20° C.*

Reference data	Glycerol	Rapeseed oil
Chemical formula	$C_3H_8O_3$ [76]	-
n (refractive index)	1.46-1.48 [71]	1.47 [72]
ρ (density)	1.261 g/cm ^{3} [76]	0.914-0.917 g/cm^3 [78]
μ (dynamic viscosity)	1412 mPa·s [76]	63.5 mPa·s [79]
ν (kinematic viscosity)	1119.7 mm^2/s [76]	78.2 mm^2/s [78]
Melting point	17.8° C [76]	-10° C [78]
Boiling/smoke point	290° C [76]	220-230° C [78]
γ (surface tension - vs air)	64.0 mN/m [80]	31.3-33.4 mN/m [79]
Experimental data		
ρ (density)	1.255 ± 0.002 g/cm ^{3}	0.912 ± 0.002 g/cm^3
μ (dynamic viscosity)	962 ± 5 mPa·s	58.3 ± 0.3 mPa·s
ν (kinematic viscosity)	767 ± 4 mm^2/s	64.0 ± 0.3 mm^2/s
γ (surface tension - vs air)	59.9 mN/m	31.4 mN/m
γ (surface tension - G vs RO)	16.6 mN/m	16.2 mN/m

Viscosity of Aqueous Glycerol Solutions — **Centipoises**

Glyc. % Wt.	Temperature (°C) 0	10	20	30	40	50
0*	1.792	1.308	1.005	0.8007	0.6560	0.5494
70	76	38.8	22.5	14.1	9.40	6.61
90	1310	498	219	109	60.0	35.5
95	3690	1270	523	237	121	67.0
100	12070	3900	1410	612	284	142

*Viscosity of water taken from *Properties of Ordinary Water-Substance*, N.E. Dorsey, p. 184, New York (1940)

Figure 4.6: *Table taken from a 1990 publication on the properties of glycerol. The table has been edited, focusing on the most relevant concentrations and temperatures [77].*

The experimental values for the glycerol deviate more from the table values, especially when it comes to the viscosity. It is not unreasonable to assume that the used liquid has drawn water from exposure to the atmosphere. This notion

is also fortified by the slightly lower value than the reference value, found for the density. Figure (4.6) shows a table taken from an investigation into the properties of glycerol, as clearly can be interpreted, glycerol undergoes dramatic changes of viscosity under changes of water concentration or temperature. The temperature was not controlled or measured during the flow experiment or the viscosity measurements.

The surface tension measurements seem convincing in the sense that the procedure delivered consistent findings upon successive measurements. For a publication with these values as part of a quantitative result, the values must be refined by multiple measurements, to thus establish a statistical mean, with the standard deviation as a reasonable figure of error, coupled with an overall assessment of the accuracy of the whole procedure.

The wetting properties as presented in section (3.2.2.4) convincingly point to the combinations of fluids and medium leading to *dynamic wetting*.

In general, it is deemed that investigations into the changes in the fluid properties, as the liquids are exposed after opening the sealed containers and under temperature fluctuations, is highly necessary. It is also apparent that all measurements and flow experiments must be correlated with temperature measurements.

4.1.5 Capabilities and limitations set up by the fluids

The fluids set up possibilities and limitations in themselves. For a given temperature they have set densities, wetting properties, viscosities, and surface tension. It will of course be possible to find other fluids. Silicone oil, for instance, has a similar refractive index, and finding another material for the porous medium can give access to the use of other fluids. However, there are many investigations that can be carried out with the given configuration.

With the two fluids given and the starting point that the gravitational field would be directed parallel with the flow, there are four simple scenarios to consider, these are presented in table (4.3), where the last two columns state the expected flow patterns. The expectations are in part based on trials done with the specific combinations and partly from published experiments on porous media flows with gravitational effects [40–43].

Table 4.3: *Expected displacement patterns from experiments with the flow-rate as the tunable parameter, given the current combination of fluids and medium.*

Method	Slow injection	Fast injection
Rapeseed inj. from the top	Stable	Unstable
Rapeseed inj. from the bottom	Unstable	Unstable
Glycerol inj. from the top	Unstable	Stable
Glycerol inj. from the bottom	Stable	Stable

A natural approach is to put results found in 2D into context, but there are also other possibilities. Here are some proposals for further topics of exploration that the configuration should be suited for:

- The competition of viscous-, capillary- and gravitational forces, through tuning of the flow velocity or the pressure gradient, both in a gravity stabilized and destabilized configuration [40–42]
- Invasion percolation comparisons with flow in porous media with gravitational effects. [43].
- Capillary bridges and draining of trapped clusters, through thin film flows [38, 39, 93**?**].
- Dispersion of colloids in a porous medium with a single fluid phase [94].
- Investigation of the dynamics of Haines jumps [32, 33, 37]
- Experiments involving tuning the effects of gravity in a geophysical centrifuge [95, 96].
- Snap off fragmentation of flow structures [97, 98].
- The influence of boundary effects on the invasion patterns in 3D [35].

4.2 3D flow regimes in gravity unstable invasion

The gathered data capture behavior that, to our knowledge, has not yet been published in a 3D situation. Injection of the more viscous and dense glycerol into the porous medium saturated with less viscous and less dense rapeseed oil led to pattern formations regulated by the injection rate. We observed unstable displacement and finger formation for the gravity unstable, slow injection rate, and a more stable displacement for the viscosity stabilized higher injection rate. This behavior can be linked to comparable studies of gravitational effects on flow in porous media in 2D [40–43] and warrant further investigation.

The data analysis is as of present at an early stage, and a model for error estimations is lacking. As a consequence, this section, therefore, does not follow the traditional template, with a conclusion section at the end, but instead has a summary of the preliminary findings. In chapter (5) I elaborate on the steps I propose to deal with these shortcomings. The developed results contain image data and 3D-renderings, volumetric calculations, a proposal for a dimensionless scaling scheme, as well as estimations of fractal dimensions for the invasion patterns.

4.2.1 The flow experiments

The flow experiments were successful in qualitatively displaying the expected transition from fingering and unstable invasion at slow injection rates, to a narrow front and a more stable invasion at high flow rates. The data collected enabled convincing segmentation of the three phases (glass beads, glycerol, and rapeseed oil) into binary volumes. In figure (4.7) the resulting invasion patterns can be seen as 3D-renderings.

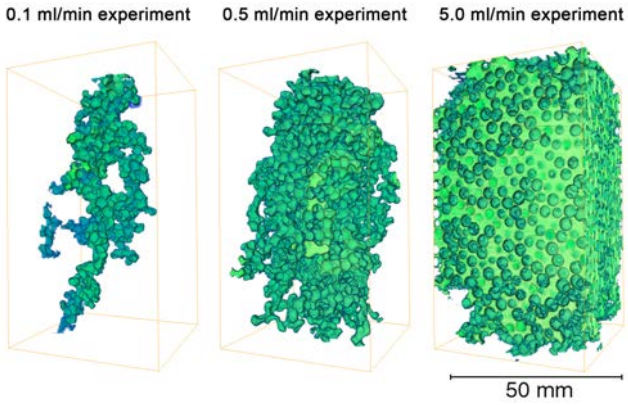

Figure 4.7: *The detected glycerol phase from the three experiments. Comparing with the familiar images from 2D-experiments we are now faced with bodies or formations, rather than patterns. However, there is certainly something both familiar and expected in the images.*

In figure (4.8) we see volume renderings of all the phases, from the three experiments.

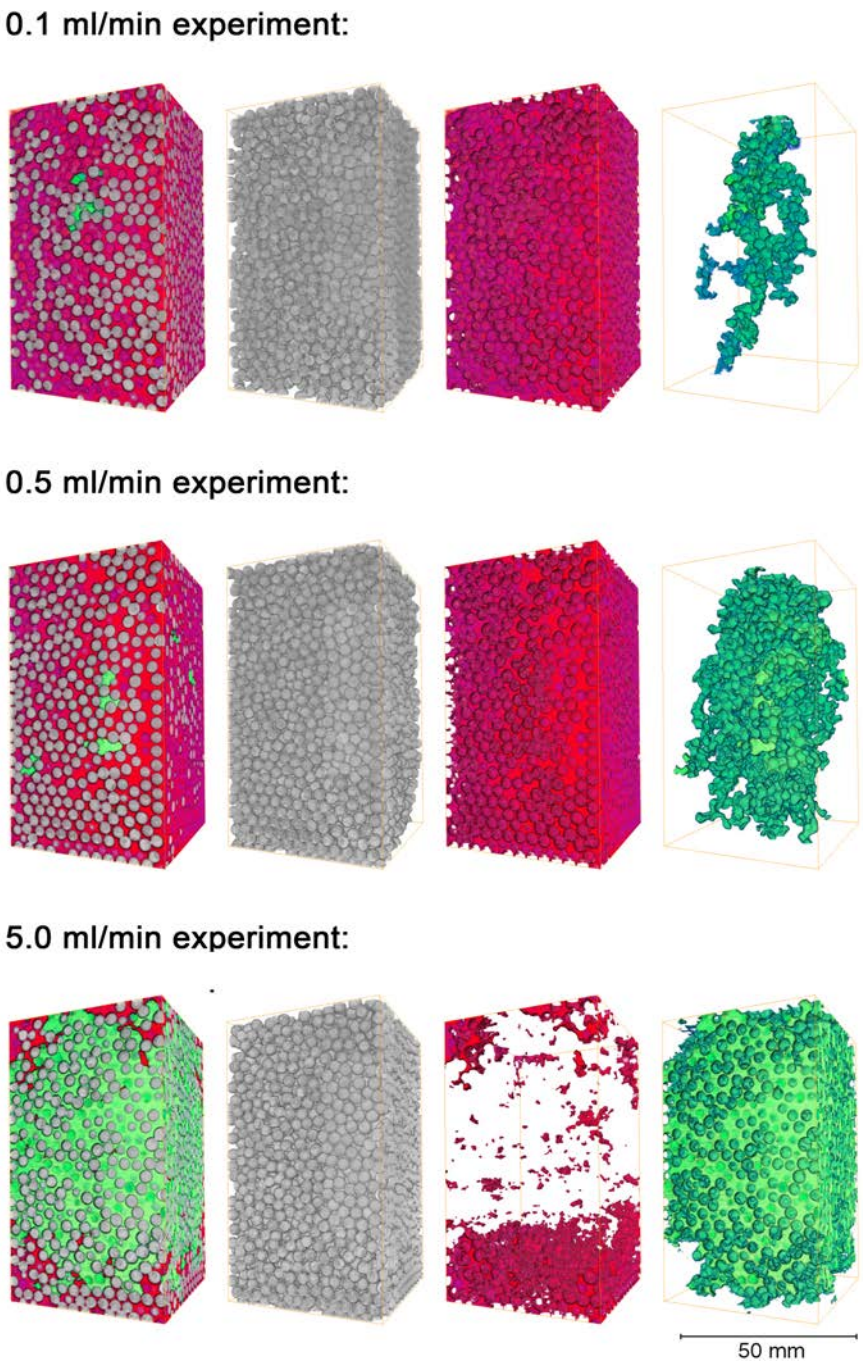

Figure 4.8: *3D-renderings of the segmented, binary bodies, with the combined volume on the left, followed by the generated spheres in the bead locations, the rapeseed oil, and the glycerol.*

Volume calculations, with resulting porosities and saturations, as well as detected numbers of glass beads, can be seen in table (4.4).

The total sample has a base of 5 cm x 5 cm and a height of 10 cm, the total volume is 250 ml. The cropped out volume is about 0.4-0.5 cm by 5 cm at each window pane, and there are about 2 cm at the top that is cropped out. This comes to a total of $\sim$ 114-130 ml. As the volume calculations show, about half the total cell volume is not part of what gets scanned. The volume not detected in the fastest experiment, should therefore reasonably be expected to be localized outside the scan range.

As can be seen, there are discrepancies in the injected and detected volumes, in particular for the slowest and for the fastest experiments. These can be accounted for by different causes. In the slow experiment, the detected volume exceeds the injected. It was plain to see, during the experiment, that the more buoyant rapeseed oil invaded the flow tube and displaced an amount of the invading glycerol. Thus a small amount of glycerol was added to the injection volume contributed by the syringe pump. This volume could reasonably be in the order of a couple of ml (this is also treated in section (3.2.4.3)). In the fast experiment, the visual representation clearly displays how the invading fluid has invaded the matrix all the way to the cell walls. In the intermediate experiment, with a flow rate of 0.5 ml/min, the invasion pattern is quite intact in the rendering, with only two fingers that barely goes out of scanner range. Here the injected volume is satisfactory accurately detected in the 3D-model, but this comes with the added remark that there is as of yet no model for error assessment in this estimation.

Table 4.4: *Volumetric results from the flow experiments. Each scan consisted of 875 frames, with the region of interest in each frame, cropped down to 870 x 1420 pixels, resulting in about 1.1 billion voxels. The total sample volume is estimated from the sample base being 5 cm by 5 cm and the height under the metal plate, pressing down on the matrix, being about 8 cm. Note that there are no estimated errors presented for the detected quantities. This will be elaborated in section (5.0.5).*

Parameter	0.1 ml/min	0.5 ml/min	5.0 ml/min
Percolation time	38.5 $\pm$ 1 min	28.5 $\pm$ 1 min	15.0 $\pm$ 1 min
Injected volume	3.85 $\pm$ 0.1 ml	14.3 $\pm$ 0.5 ml	75 $\pm$ 5 ml
Detected volume	4.0 ml	14.8 ml	47.7 ml
Detected saturation	0.069	0.26	0.88
Detected beads	5113	5167	5325
Detected porosity	0.44	0.44	0.42
Total detected volume	128.7 ml	128.7 ml	128.7 ml
Total sample volume	$\sim$250 ml	$\sim$250 ml	$\sim$250 ml

4.2.2 The pressure data

Pressure sensors were installed at the inlet (top) and outlet (bottom) of the cell. The purpose of these sensors was to get some intuitions about how the pressure would behave under the experiments[1], but also the idea that they would provide data that could be correlated with the scan data to quantitatively describe the dynamics. The first experiment conducted was the one with the intermediate injection rate (0.5 ml/min). Here the pressure sensor at the top failed after about 4 of the 28.5 minutes the experiment took. The bottom sensor worked fine, so I used this at the top in the two other experiments. For these measurements were not made at the bottom.

In figure (4.9) the readings from the sensor at the inlet are shown. The plots start at the moment the invading fluid enters the cell and ends at the moment of percolation. For the 0.5 ml/min experiments only the first 250 s, until the sensor failed, are included.

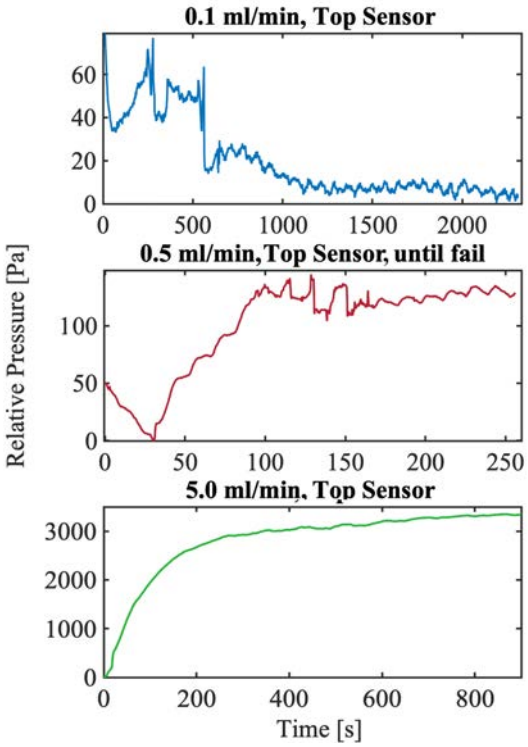

Figure 4.9: *Pressure sensor readings from the inlet (top). The readings are relative, setting the zero-level by the lowest value measured during the experiment, as the sensors have not been calibrated to give a baseline.*

[1]Pressure is not a parameter that I have the same intuitive appreciation of as, for instance, weight or velocity. The atmospheric pressure at sea level, or in the lab, is taken to be about 101 kPa. Ten meters under the sea level this pressure is about doubled. A column of water contributes about 10 kPa per m, or 10 Pa per mm.

The readings from the 0.5 ml/min experiment should be appreciated with suspicion, as there was some instability in the communication between the computer and the multimeter, causing the readings to crash. I still believe the readings recorded to be correct. In section (3.2.4.3) I explained what I think caused the strange readings in the beginning of the 0.1 ml/min experiment, relating to capillary action going on in the actual inlet tube and a pressure build-up before the valve was opened to start the flow. The pressure drop at the beginning of the 0.5 ml/min experiment can be interpreted similarly.

The more general trend that can be seen later, for the two slower experiments, and throughout the fastest, is perhaps more telling. In the 0.1 ml/min experiment the injection rate does not seem to dictate the pressure situation. The pressure is fluctuating as a response to capillary events as the fluids invading slips through the matrix. In the intermediate experiment, the injection rate becomes significant, but the capillary events can still be felt. In the fastest experiment, the pressure readings are completely dictated by the pressure build-up caused by the viscosity of the fluids and the high injection rate.

In figure (4.10), close ups from the measurements at the inlet can be seen. The idea is to further try and see if there is something to be learned about the dynamics and their time-scale.

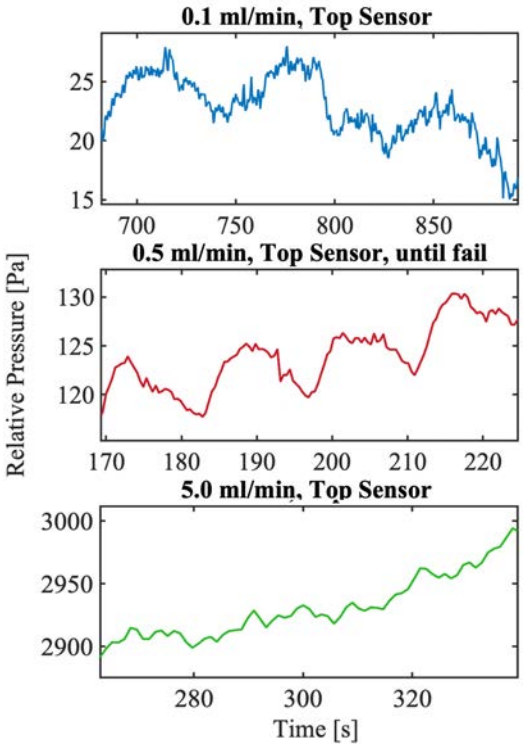

Figure 4.10: *Close-ups from the plots of the readings from the sensors at the inlet. The smaller fluctuations at the finest detail level are from one time-step to another and should reasonably be interpreted as noise.*

The close-ups seem to confirm the initial analysis. In the slow experiment, the build-ups and releases are also slow, with a period of 10-50 s. The preserved data from the more stable phase of the 0.5 ml experiment shows the most interesting pattern. This could very well be what is known as *Haines jumps* (see section (2.3.14)). In the fastest experiment, the close-up shows fluctuations that represent one time step and should be interpreted as noise. This confirms that there are no measured local fluctuations, but only a general build up, flattening out as the saturation of the invading fluid becomes more and more dominant.

In figure (4.11) a plot from the outlet during the 0.5 ml/min experiment can be seen. The outlet tube was submerged at the bottom of a basin with a surface of approximately 1500 cm^3, meaning that per ml of added fluid, the pressure would rise by about 0.007 Pa, putting the total rise, for the injected 14 ml, at $\sim$0.1 Pa, which is not measurable by the used sensors. As already mentioned in the methods section I did make a mistake in my thinking here. The outlet basin was filled with water; it should have been filled with the defending fluid. As the displaced fluid was ejected into the basin the interface between the oil and the water curved out until a drop was released, creating pressure build-ups and releases.

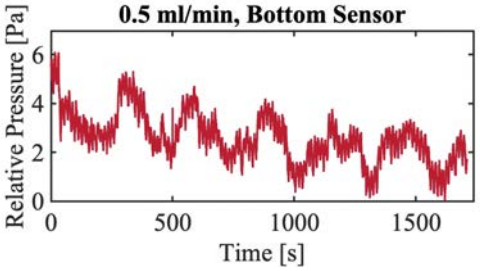

Figure 4.11: *Pressure readings from the outlet (bottom) sensor during the 0.5 ml/min experiment. The readings are relative, setting the zero-level by the lowest value measured during the experiment*

The measured fluctuations at the outlet are very minute. The larger oscillations could be from drop formation and release at the tube end, but the number of tops seems a bit small for a total of 14 ml ejected. It is also curious to see that the pressure seems to drop slightly, rather than rise (there is of course the chance that the data could be inverted, but I did a test for this, and the values suggest that it is not). The drop is minimal, but certainly higher than what would be expected from a change in the height of the water column.

4.2.3 The Reynolds, Capillary and Bond numbers

To further establish the significance, of the measured fractal dimensions and their respective flow regimes, one can look at the various dimensionless numbers attributed to flow in porous media, Re, Ca and Bo, as described in sections (2.3.9), (2.3.12), and (2.3.15). For clarification, I restate the definitions I have used.

$$Re = \frac{\rho u a}{\mu},\ Ca = \frac{u\mu}{\gamma},\ Bo = \frac{\Delta\rho g a^2}{\gamma},\ \text{ and } Bo^* = \frac{Bo}{Ca} = \frac{\Delta\rho g a^2}{u\mu}, \tag{4.1}$$

By these definitions $Bo >> Ca$, therefore I propose Bo^* as a possible dimensionless number. For easy reference I have included the used values in table (4.5).

Table 4.5: *Values from table (4.2), converted to compatible units.*

Parameter	Value
ρ	$1.255 \cdot 10^3$ kg/m^3
a	$3.0 \cdot 10^{-3}$ m
μ_1	$962 \cdot 10^{-3}$ Ns/m^2
γ	$16.6 \cdot 10^{-3}$ N/m
$\Delta\rho$	$(1.255 - 0.912) \cdot 10^3$ kg/m^3 = 343 kg/m^3
g	9.81 m/s^2

The average flow velocity in the pores, u, can be evaluated as the flow rate, Q, divided by the average cross section, A, of the flow body. The flow bodies are binary data organized with x as the horizontal direction and y as the vertical direction captured by the camera as 2D-frames, and with z as the horizontal direction represented by the individual frames as the laser moved through the sample. A can be evaluated as the average over the sums of all the frames parallel to the xz-plane (or simply the sum over the bodies, divided by the number of horizontal planes), multiplied by the pixel dimensions. The resulting numbers, Re, Ca and Bo, are presented in table (4.6).

Table 4.6: *Dimensionless numbers and the parameters used in the calculations.*

Parameter	0.1 ml/min	0.5 ml/min	5.0 ml/min
Q	$1.7{\cdot}10^{-9}$ m^3/s	$8.3{\cdot}10^{-9}$ m^3/s	$8.3{\cdot}10^{-8}$ m^3/s
A	$5.3{\cdot}10^{-5}$ m	$2.0{\cdot}10^{-4}$ m	$6.4{\cdot}10^{-4}$ m
u	$3.1{\cdot}10^{-5}$ m/s	$4.2{\cdot}10^{-5}$ m/s	$1.3{\cdot}10^{-4}$ m/s
Re	$1.2{\cdot}10^{-4}$	$1.6{\cdot}10^{-4}$	$5.1{\cdot}10^{-4}$
Ca	$1.8{\cdot}10^{-3}$	$2.4{\cdot}10^{-3}$	$7.5{\cdot}10^{-3}$
Bo	1.8	1.8	1.8
$Bo^* = Bo/Ca$	1003	751	242

4.2.4 Fractal dimension estimations

Fractal dimensions estimations is a well-established method to analyze the geometric shapes created from flow regime transitions (see sections (2.3.13) and (2.3.16)). The method used for the calculations is as described in section (2.3.10). The binary data was imported into Matlab, where the box-counting algorithm was applied. The resulting associated plots and results are presented in figure (4.12)

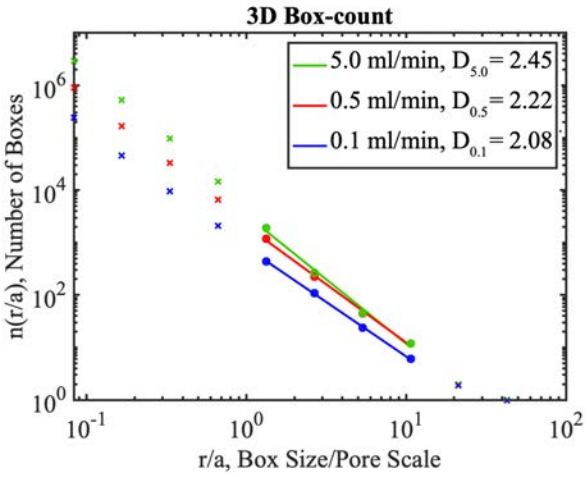

Figure 4.12: *Fractal dimension calculations from a 3D-box-counting method, as described in section (2.3.10). The x-axis on the plot has been rescaled, from the voxel scale to the pore scale. The fractal dimension is as the slope of a linear fit from the four points scaling from the pore scale (3 mm) and up one decade (∼3 cm), which is about the range of the relevant geometry. The estimations are made from the entire segmented binary bodies of the invading fluid, glycerol. The data was reduced to 20% of the original resolution, by simply extracting every fifth element in each dimension, for reasons of restrictions on the matrix size in Matlab.*

The fractal dimensions are calculated on a very small scale, going over only one decade. Thus, the results should be considered approximations. This is a given with the current sample cell size. To get more reliable results investigations with a more extensive system should be made, or alternatively, a large number of experiments could be conducted, to give the findings statistical credibility.

4.2.5 Summary of the experiments

The found patterns show a clear transition, from unstable displacement and fingering, at the slow injection rate, via an intermediate stage, to stable invasion with a narrow front, at the high injection rate.

To meaningfully interpret the data it must be put into context with similar experiments and a theoretical framework.

Both invasion percolation and diffusion-limited aggregation algorithms have established ranges for the fractal dimensions of 3D branch bodies. As the established patterns found by these methods in 2D are very convincingly similar to the flow patterns made in 2D-experiments with flow in porous media, it is also of interest to compare simulation generated 3D-bodies with 3D-experiments. In 1982 Paul Meakin conducted DLA simulations in 2D, 3D and 4D. For 3D with a cubic lattice he found a Hausdorff dimensionality corresponding to the fractal dimension of 2.51 [99]. Critical values for percolation with IP puts the

fractal dimension in 3D in the range of 2.52-2.9, depending on the simulation lattice [26].

Gérard Daccord and Roland Lenormand conducted some interesting experiments, published in 1987 [100]. They obtained very real 3D-data, by pouring a polymerizable resin into dissolution patterns created by flowing water through plaster samples. They then fully dissolved the plaster and were left with treelike structures in the shape of the dissolution patterns. They were still forced to use an indirect method to estimate the fractal dimensions. They analysed the injection-pressure curve and observed that the pressure, p, decreased linearly with ln t (t is time). From Darcy's law for a homogeneous cylindrical porous medium of radius R, they interpreted that the pressure at a distance r scales as $p(r) \sim \ln(R/r)$. It was experimentally established that there was no pressure drop from $r = 0$ to $r = R_e$, where R_e is a characteristic dimension of the dissolution pattern, varying with thime according to a power law, $R_e \approx t^{\alpha}$. The fractal dimension, D, is found by the relation $D = d - \alpha$, where d is the space dimension. They arrived at resulting fractal dimensions in the range of 2.30-2.35.

There are a few comparable experimental studies. Frette et al. made 3D-experiments and IP simulation in the 1990s and in a 1994 paper [45] (see section (2.3.17) for more about this article). The method did not consider gravitational effects, as they used density matched liquids, but with a viscosity ratio of $m \approx 14$, with the invading fluid being the less viscous (the inverse of our experiments). They estimated fractal dimensions in the range of $2.6 - 3.0$ for their 3D-pattern formations, from slow to fast injection, with the corresponding capillary numbers in the range $1 \cdot 10^{-3} - 3 \cdot 10^{-2}$, and Reynolds numbers in the range of 1-24. They did, however, not have real 3D-data, as we have. Instead, they had orthogonal 2D-projections of the invasion structures. The Fractal dimensions were then estimated, through an argument about the type of 3D-structure these projections represented.

In section (2.3.17) i present a study by Dalbe and Juanes [46], where they found fractal dimensions for 3D-flow bodies in the range of of 2.2-2.8.

These two studies are both different from the one conducted, but they serve as a good starting point for putting the findings into context. Since the Bond number is the same for all three flow rates, it seems meaningful to consider some version of a modified bond number. As the Ca and Bo are three orders of magnitude apart, it is more reasonable to multiply or divide them with one another, than it would be to subtract them from one another. Here the findings are considered in light of a definition $Bo^{**} = Bo/Ca$, which makes sense, as a higher Bo^{**} then signifies the gravitational forces playing a more significant role. The results do not reveal any critical thresholds. To discover at what Bo^{**} the flow is fully determined by the gravitational forces, we could conceivably conduct a number of slow experiments, until decreasing the flow rate no longer alters the pattern characteristics. Similarly finding a high rate where further increase no longer changes the front would establish a critical Bo^{**}, where viscous forces fully dominate. These thresholds could then be coupled with the corresponding fractal dimensions.

The found fractal dimensions $\sim 2.1 - 2.5$ in the range of the results from DLA and IP simulations, as well as the comparison experiments. As stated, significant uncertainties should be associated with the found values, but they nevertheless stand out as a starting point for establishing a better understanding.

As a conclusion, the following qualitative description of the findings is offered: For the slow injection the dynamics are dominated by gravitational and capillary forces, there is a marked net downward direction on the flow. The pattern meanders some horizontally, suggesting that the geometry of the matrix, as well as the capillary forces, also contribute to the evolution of the invasion front. As the flow rate is increased the viscous forces become apparent, redistributing the force gradients throughout the invasion body, through feedback between the driving pressure and friction in the liquid. The overall downward pull of gravity then is becoming of lesser importance, as the viscous forces generate a global pressure in all directions. This result is further put into context with found indicative fractal dimensions and modified bond numbers, ranging from $D_{0.1} \approx 2.1$ and $B^{**}_{0.1} \approx 1000$ for the slowest injection rate, to $D_{5.0} \approx 2.5$ and $B^{**}_{5.0} \approx 240$ for the fastest rate.

CHAPTER 5

Discussion

Many issues which belong in this section have already been brought up. Here I shall try to summarize and further them, as well as topics that have been left out.

5.0.1 The scanner

At the onset of this project other groups around the world had already developed models for 3D-scanning of flow in porous media, with similar experimental ideas. Several of these projects had produced published findings [46, 90, 91]. It was given that a scanner could be achieved. Nevertheless, there were many unknowns. The aim was always to make a better, or at least different, set-up than what had been used in published experiments. The details of the experimental methods, used in these other projects, are not all easily extracted from published articles, and even though the porous media community is very open and accessible, I never came in contact with the actual researchers that had performed these experiments. Ruben Juanes from MIT and Tanguy Le Borgne from the University of Rennes, where similar projects have been undertaken, both came for seminars at UiO, and I had the occasion to ask them some questions, but they had not participated in all of the experimental work, so there were details they could not provide. This is not to say that valuable help was not to be found. Testing the liquids versus the borosilicate glass beads was already initiated, by Knut Jørgen Måløy and Mihailo Jankov, and although the final liquids were not yet established, the method was outlined.

Finding the dyes was one of the more challenging stages of the process, but with great help via numerous emails, from sales representative Paul Cahill from the company Exciton, the final dyes were found, and upon testing them, the greatest moment of elation, of the whole project, came forth. In figure (5.1) a frame, from this test, can be seen.

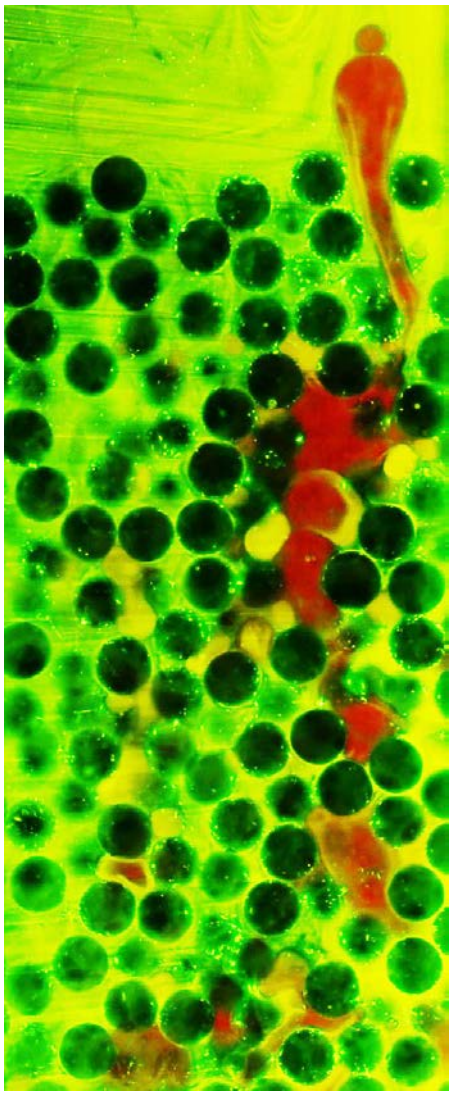

Figure 5.1: *After running a number of tests with different set-ups, cell sizes, liquids, dyes and filters, I finally found a combination that gave me this image. The slice is from the middle of a sample cell with a 30 mm x 30 mm base and a height of 10 cm. The sample was initially filled with glycerol, with Fluorescein 548 dye. 3 mm borosilicate glass beads were poured slowly in, to avoid trapping air bubbles. The glycerol can be seen as the green liquid, the beads are the dark patches. Rapeseed oil, dyed with Pyrromethene 650, was then injected, through a valve at the bottom of the sample, and is seen as red. The moment caught is of a dynamic situation. We can see the bubbles of red soaring up, driven by buoyancy, even displacing beads and creating larger pores. The actual scan process, of the whole sample, takes about 20 seconds. This means that the flow-regime caught is not suited for the scanner, but the image still felt like final confirmation that the set-up would work. It was the first image that really impressed me and spurned me to finalize the algorithm to analyze the images, with the goal to develop a 3D-model, with the porous medium and the two liquids each localized and fully rendered.*

A crossroad was choosing how to propagate the laser sheet through the sample. Two main options were considered, either shifting a stationary sheet through by motorizing the laser, as have been done, or by shifting the sheet itself, by letting it pass through a rotating prism, as done by Kong et al. [90]. The advantage of such an approach is the mechanic simplicity of the sheet propagation, enabling very high time resolution, without risking mechanical vibrations, such that would be created with a rapidly oscillating actuator.

To benefit from the rotating prism Kong et al. used a stationary camera, with a reduced aperture, to maintain the whole sample volume in focus. This leads to disadvantages already treated in section (3.1.7). One possible work around could be emerging lens technology, where the focal length can be very rapidly altered, by stretching and compacting a flexible lens element [101], much as is

done by our eyes. Figure (5.2) shows the illustration of their set-up, from the published article [90].

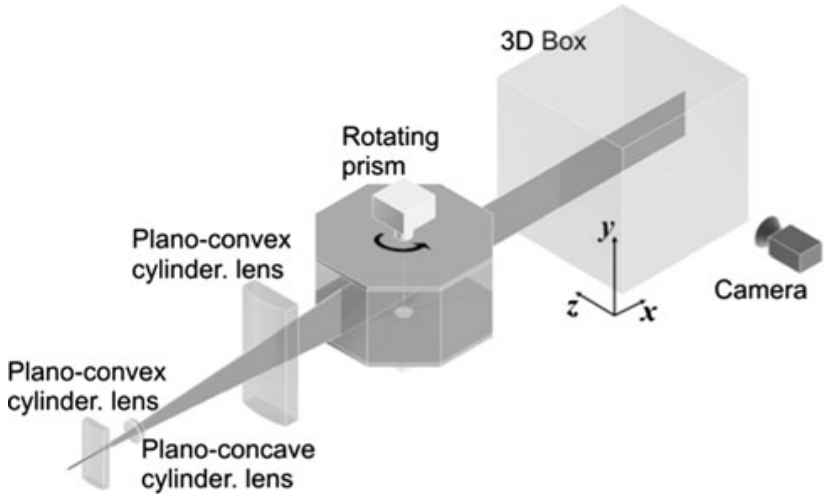

Figure 5.2: *Illustration of the experimental setup developed by Kong et al.. From the figure caption: Sketch of the 3D-experimental setup. The laser beam is expanded and thinned to a light sheet and then scanned through the observation volume using an eight-face prism [90].*

The solution we have settled on has the obvious limitation of poor time resolution. It is hard to imagine the set up being able to deliver scans at a much lover integration time than 10 s. Therefore I suggest to continue on a path where the studied dynamics are either sufficiently slow, happen in burst between static situations or are in a steady state configuration.

In the current configuration of our scanner the limiting factor that should be considered above all, is the refractive index matching. The optical quality of the transparency is of vital importance to the precise and detailed scanning. If there is a way to improve the matching, either by modifying the liquids chemically, regulating the temperature or by simply finding better fluids, this would indeed be interesting, especially if one wants to study a larger sample. Another approach to increasing the sample size could be to simply reduce the characteristic pore scale, for instance by using smaller glass beads, but there is an evident risk that the flawed index matching will make this futile, as a smaller pore scale only will lead to an increased frequency of fluid-medium interfaces, that each leads to distortions. A factor to consider, when reducing the pore scale, is the added complication in ridding the sample of trapped air, in the experimental procedure.

We have already had some discussions about building a new, larger scanner. I certainly have some ideas about how to go about this. One proposed addition would be to use two lasers, on either side. I initially embraced this idea, but I now believe this to be the wrong way to go about it. The brightness gradients in

the imaging plane are not beyond what can be dealt with with image processing and in what I have seen the penetration depth of the laser sheet is not what primarily limits using larger samples, but as already stated the main limiting factor remains the index matching, it is not the penetration depth of the laser sheet that is insufficient, it is the transparency needed to transfer the images at far distances from the front window. To work around this the solution should rather be to add another camera, at the back, and then synchronize and merge the two recordings, taking data from the front from one, and from the back from the other. This does off course involve some complicating factors.

Here is my proposed strategy for developing a new scanner, or possibly merely improving on the existing one.

- Sample cell design - The general idea of the existing sample cell, with a base and top made of plexiglass, with groves for the glass panes, was sound, but a solution that eliminates the need for columns at the corners should be found, to allow for scanning of the entire volume.
- Implementing a fixed sample cell holder - ensuring that the sample cell is held at precisely the same location for every experiment, will make it easier to implement automated location data, linking the recorded frames to spatial and temporal coordinates and such as pressure readings.
- Finer tuning of the refractive index matching - this topic has been elaborated in this section already. Possible approaches could be influencing the refractive indices of the used fluids, either by temperature control or by chemical tuning, or by finding better fluids or another material for the porous medium.
- A better suited camera - the camera currently used has sufficient image quality, dynamic range and resolution, but it is lacking in frame-rate. Improvements in dynamic range and poor light performance will always be valuable. However, it is not optimized for synchronized recordings. Ideally the image data should be recorded directly into a computer, in such a manner that each scan holds a precise amounts of frames, beginning and ending at the exact same location of the sample, and each mapped in time and space. There are cameras better suited for these applications available.
- Adding another camera at the rear end. As already stated the flow cell size can possibly be doubled by adding another camera at the back side of the cell. This would further stress the need for a good routine in terms of data recording and synchronization, as treated in the previous point.
- Exploring the possibility of using a laser that radiates at a higher frequency - as the key to separating the phases lies in the fluorescent dyes radiating at separable frequencies, making them have the largest frequency gap possible is desirable. As fluorescent radiation always will occur at a longer wavelength than the light used to excite, a shorter wavelength source could offer a larger range to play with. This would then entail finding

new, matching dyes, that also work with whatever fluids that are going to be used.

5.0.2 Segmentation and visualization

The segmentation and visualization have been succesful beyoind expectations. The qualitative assesment of the results is very promising and the images draw a lot of positive attention. That being said, there is definite room for improvement, both in the streamlining of the segmentation process, and in the establishment of a fully comparable and consistent process, to ensure that each scan is segmented by the same criteria.

5.0.3 The fluid properties

Establishing accurate and dependable values for the fluid property parameters will be vital both to the credibility of any publication and to the possibility to correctly identify any physical mechanism in the studied dynamics. Here I dare say that this is something that perhaps have been taken too lightly in quite a few of the papers I have read during this work. This topic should be an immediate focus for any continuation of the experimental work initiated in this project.

5.0.4 The flow experiments

Certain aspects of the experiments were partially failed, in particular the recording of data from the pressure sensors, where only segments of the flow are preserved, from two of the three experiments, whereas the third contains the full data-set. In retrospect it is also clearly desirable to have a sample cell that allows for scanning all the way up to the glass panes. The outlet should have gone out in a basin filled with the defending fluid, to strengthen the approximation of constant pressure at the outlet.

That being said, the gathered data has allowed for very fruitful analysis, immediately putting the experiments into context with significant studies conducted in 2D. It should be relatively easy to redo the experiments, correcting for the slight errors, and more importantly, in the context of more well established fluid properties and a fully developed model for error estimations. The preliminary analysis here should then be a very good guideline for what very reasonably should result in a publication.

However, another modified bond number should perhaps be derived, along the lines used Méheust et al. [40] as a characteristic scaling parameter. In figure (5.3) some length scales and reference values used in the consideration are presented.

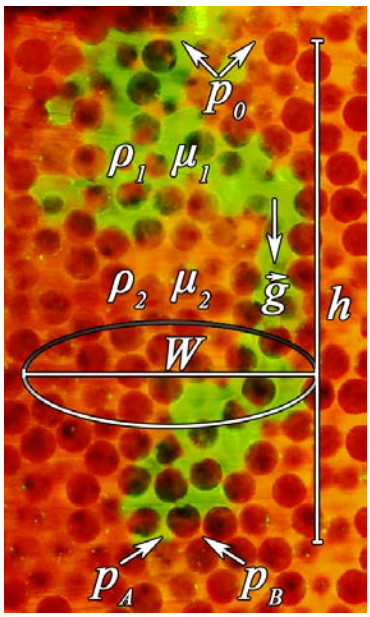

Figure 5.3: *Close-up from an intermediate moment in the 0.1 ml/min (slowest) experiment. Fluid 1 is the invading glycerol, which is more dense and more viscous, fluid 2 is the defending rapeseed oil. The height, h, is the vertical distance from the inlet to the lowermost tip of the invasion finger, and W is the width, or diameter, of the global invasion body. p_0, in either fluid should be equal at the height of the inlet at the top. The pressures in the fluids at the height of the lower most points should then be determined by the columns of liquid of different densities, modified by viscous pressure drops. Thus, we should get $p_A = p_0 + \rho_1 gh - \mu_1 uh/k$ and $p_B = p_0 + \rho_2 gh - \mu_2 uh/k$, where k is the permeability.*

From the figure we can see that the combined gravitational and viscous pressure, Δp_{gv} can be written as

$$\Delta p_{gv} = P_A - P_B = \left(p_0 + \rho_1 gh - \frac{\mu_1 uh}{k}\right) - \left(p_0 + \rho_2 gh - \frac{\mu_2 uh}{k}\right). \quad (5.1)$$

With the added relation $\mu_1 >> \mu_2$ we get

$$\Delta p_{gv} = \Delta\rho gh - \frac{\mu_1 uh}{k} \quad (5.2)$$

To get the Bond number and capillary number to assume similar orders of magnitude Méheust et al. [40] defines a capillary number

$$Ca^{**} = \frac{\mu u a^2}{\gamma k}, \quad (5.3)$$

where an experimentally derived permeability, k, scales Ca^{**} to a comparable order as Bo. They further introduces the modified Bond number

$$Bo^{**} = Bo - Ca^{**} = \frac{\Delta\rho g a^2 k - \mu_1 u a^2}{\gamma k} \quad (5.4)$$

By using the derived Δp_{gv} a Bond number, Bo^{***} can be written as

$$Bo^{***} = \frac{\Delta p_{gv}}{\Delta p_{\gamma}} = \frac{\Delta \rho g h - \frac{\mu_1 u h}{k}}{\frac{\gamma}{a}} = \frac{\Delta \rho g h a k - \mu_1 u h a}{k\gamma}, \tag{5.5}$$

As the permeability has not yet been measured it is hard to evaluate if this is a good approach. The modified bond number makes sense if the permeability is found to be in an order of magnitude ($\sim 10^{-3}$) that scales the viscous term to a comparable size with the gravity term.

This further rises the question, of whether a scaling law can be found, connecting the flow body geometry, to such a Bond number? For instance along the lines of the relation, found in [40], $w \sim F^{-\nu/(1+\nu)} = [(\gamma/W_t a)(Bo - Ca))]^{-\nu/(1+\nu)} \sim (Bo^*)^{-\nu/(1+\nu)}$, where w is the front width, ν the correlation length exponent, γ is the surface tension, W_t is the width of the normalized capillary threshold distribution, and a is the typical pore size.

5.0.5 Establishing a model for error estimations

The model for error measurements is perhaps the single most important aspect one should consider, when assessing the quality and credibility of any scientific finding. This aspect certainly is a shortcoming in this work so far. I could have pushed the insights I have and derived some more initial estimations, but I have not. Partly it is a consequence of having prioritised other aspects, I felt that I needed to produce results foremost, but I honestly think that such estimations would have been both premature and speculative. I have not developed enough data to reasonably compare and establish any idea of a baseline, and I have also been working mostly alone, so there are surely factors I have overlooked. I find it much more probable that a good understanding of the precision and accuracy of the measurements can be reached by conducting these steps again, with more than one head in the loop (preferable one with more experience in the field than me).

The model for error estimations should couple at least four aspects of the experimental chain:

- The fluid properties
- The scanning, image processing and phase segmentation
- Analysis of the image data
- Time correlated pressure and temperature data

The error model should follow established procedures, for instance by the methods described in *Practical Physics*, by G. Squires [102], combining errors as stipulated by the data-sheets of the involved measuring tools, and errors derived from statistical approaches.

5.0.6 Further analysis

The conducted experiments certainly warrant further analysis, both to expand on the specific case, but also as a map for further experiments. At this point I am overwhelmed by the number of aspects I want to expand on and further develop. I have not yet been able to carry out further analysis, but the *Pore Network Model Extension* in Avizo should provide a very good starting point for further investigations. Here is a list of the specific parameters it claims to estimate:

- Pore volume
- Pore area
- Pore equivalent radius
- Pore center of gravity
- Pore coordination number (i.e., number of connected neighbors)
- Intersection percentage between pore network model and original pore space
- Throat area
- Throat equivalent radius
- Throat channel length
- Throat connection (i.e., Id of pore 1, Id of pore 2)

In addition a measure of the front width can be introduced, as well as

Together the initiated investigations, and the many new parameters that can be taken into account, should be an ample foundation, both to put the experiments into context with previous work, an hopefully to develop novel approaches.

Beyond the comparisons with IP and DLA, by looking at the scaling of dimensionless numbers such as, Ca and Bo with fractal dimensions and other geometric characterizations, I am intrigued by the possibility to link the work exerted by the injection pump to the dynamics by looking at dissipation processes, for instance along the line of the work relating to Haines jumps by Berg et al. [37].

5.0.7 Outlook

The development of the optical scanner and the preliminary experimental results have drawn quite a bit of attention in the community surrounding PoreLab. I am excited and motivated by the work so far. I greatly hope that what has been done in this project is only a beginning, and also that I might have a role in what is to come.

Apart from that I would love to achieve cold fusion as a table top experiment, and design more efficient steam turbines (than the ones we loose nearly all the energy from nuclear- and fossil-power stations with), but mostly I would love to be able to even begin to understand human behaviour and relationships (why is it so hard to do something right?)!

Postface

It is with a touch of melancholia I write this. Many do not, in particular, enjoy the period around exams or deadlines for written assignments - I do. The exam periods during the past years as a physics student have actually been some of the best times in these years. I love the feeling of state of emergency, the dissolution of day and night, the ceaseless one-sided focus - as well as the inevitable feeling that it is not at all going to work out, that it will all flop, that I will be left unmasked, barren and pitiful, standing in the middle of the square with my pants down on my ankles. Mostly, I like the period because it puts me into a condition of focus and learning, in many ways those few weeks are the only time of the year when my brain is functioning at somewhere near peak level. Something I think brains occasionally should do.

Before starting I associated a certain mystique with the term *physicist*, a little like most people tend to when it comes to *doctors*. Just like we expect doctors to be able to diagnose us and prescribe an appropriate cure from merely seeing us, I expected physicists to walk around with the answers to all kinds of highly important questions that ordinary people did not even know existed. In a way, I suppose that both of these assumptions are slightly justified, but physicists and doctors differ in one crucial regard. Through their education and from our general perceptions, doctors can actually know what *they are* and what it is expected that *they should do*. When I am asked about what I am going to do with all of these hidden mysteries I now possess, I like to quote from a fictional tv-series about Albert Einstein: *I am going to zink for ze sake of zinking!* I think it is a quite catchy thing to say. But I would actually like to do something more. I would greatly appreciate being able to be a part developing something that can be of use, especially in the context of the many challenges we are facing, both as a species and in the greater context of being matter in the unique configuration we refer to as *life*.

There are certainly serious issues and processes that should be treated with respect, but I do not think that life is fundamentally serious. It is just as much absurd actually! Anyone who claims otherwise should do some more zinking! One of the precious mechanisms that actually lends some feeling of sense to the madness is what we call *humour*. We do not understand, but hopefully, we can laugh about it. Figure (1) is my parting remark.

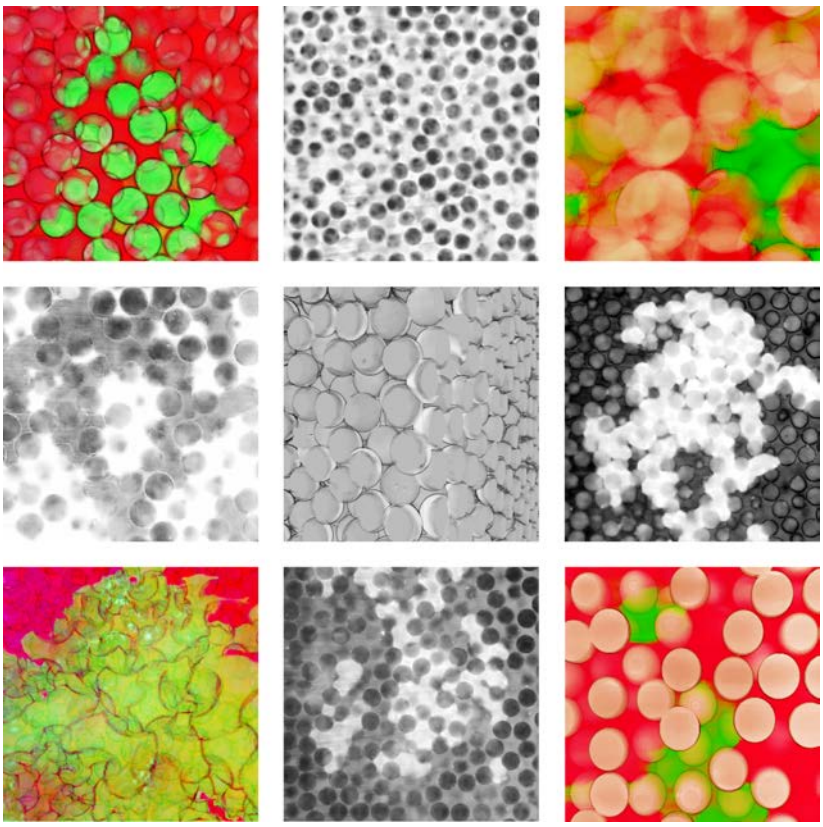

Figure 1: *To be read out loud by Sir David Attenborough as you look at the pictures: The herd of fluid elements faces a perilous journey. As the newly created element enters the matrix it is entirely cubic, but immediately it is deformed by shear and insurmountable stresses, added to this it is constantly exchanging molecules with the surroundings. Still, it must remain one element, the equations simply demand it. As it is faced with alternative pore-throats the element alone holds the secret as to whether it has a wave- or particle nature, perhaps it could even have told whether space is discrete or continuous. Alas, before it reaches any statistical significance, it has been entirely smeared out, ripped to shreds in a merciless vortex of staggering Reynolds numbers. The equations have completely broken down, and the model is left in tatters, only wisps of faint green are left - thin film flows - gathering the remains of a once glorious theory and sending them irretrievably down the drain.*

To put figure (1) in to context, I urge you to consider that the number of infinitesimal fluid elements, in say, a herd of antelopes on the savannah, is a very large finite infinite, but still, it is much, much smaller, than say, the number of ways you can put all the socks you have in the sock drawer, one over the other on a single foot[1].

[1]This actually has an analytical result, $N_{\text{sock combinations to consider}} = 107! = 1.2 \cdot 10^{172}$ [103], which coincidentally happens to be about the estimated number of atoms in the observable universe, *times itself.*

Bibliography

[1] H. S. Hele-Shaw. The flow of water, Nature 58, 34–36 1898.

[2] Slice of bread. Photo from web-page.
URL www.womenshealthmag.com/food/a19901697/high-carb-foods/.

[3] Jens Feder, Eirik Grude Flekkøy, and Alex Hansen. Flow in Porous Media, 2018. Unpublished.

[4] J. D. Bernal and J. Mason. Packing of spheres: Co-ordination of randomly packed spheres. Nature 188, 910–911 1960. doi: 10.1038/188910a0.

[5] Grunde Løvoll, Knut Jørgen Måløy, and Eirik G. Flekkøy. Force measurements on static granular materials. *Physical Review E - Statistical Physics, Plasmas, Fluids, and Related Interdisciplinary Topics*, 1999. doi: 10.1103/PhysRevE.60.5872.

[6] Wu-Yi Hsiang. On the sphere-packing problem and the proof of Kepler's conjecture. *International Journal of Mathematics*, 2004. doi: 10.1142/s0129167x93000364.

[7] Thomas C. Hales. A proof of the Kepler conjecture, 2005.

[8] Daniel M. Mueth, Heinrich M. Jaeger, and Sidney R. Nagel. Force distribution in a granular medium. *Physical Review E - Statistical Physics, Plasmas, Fluids, and Related Interdisciplinary Topics*, 1998. doi: 10.1103/PhysRevE.57.3164.

[9] C. H. Liu, S. R. Nagel, D. A. Schecter, S. N. Coppersmith, S. Majumdar, O. Narayan, and T. A. Witten. Force fluctuations in bead packs. *Science*, 1995. doi: 10.1126/science.269.5223.513.

[10] Bjørn Gjevik. Innføring i fluidmekanikk mek3230/4230 - forelesningsnotater, 2009.

[11] Wikipedia: Viscosity.
URL en.wikipedia.org/wiki/Viscosity.

[12] D. J. Acheson. Elementary Fluid Dynamics, 2005.

[13] Brian Kirby. *Micro- and Nanoscale Fluid Mechanics*. 2012. doi: 10.1017/cbo9780511760723.

[14] A J Smits. A Physical Introduction to Fluid Dynamics, 2000.

[15] I. M. Cohen P. K. Kundu. Fluid mechanics, Second Edition, 2002.

[16] Wikimedia: the stress tensor. Illustration downloaded from web-page, . URL commons.wikimedia.org/wiki/File:Components_of_Stress_Tensor.png.

[17] Wikipedia: Darcy's law. Illustration downloaded from web-page, . URL en.wikipedia.org/wiki/Darcy{%}27s_law.

[18] Osborne Reynolds. An experimental investigation of the circumstances which determine whether the motion of water shall be direct or sinuous, and of the law of resistance in parallel channels. *Proceedings of the Royal Society of London*, 1883. doi: 10.1098/rspl.1883.0018.

[19] Jens Feder. *Fractals*. 1988. ISBN 978-1-4899-2126-0 978-1-4899-2124-6.

[20] R. Lenormand. Flow Through Porous Media: Limits of Fractal Patterns, 2006.

[21] R. Lenormand, C. Zarcone, and A. Sarr. Mechanisms of the displacement of one fluid by another in a network of capillary ducts, 1983.

[22] Knut Jørgen Måløy, Jens Feder, and Torstein Jøssang. Viscous fingering fractals in porous media, 1985.

[23] Motofumi T Suzuki. A three dimensional box counting method for measuring fractal dimensions of 3D models. In *Proceedings of the 11th IASTED International Conference on Internet and Multimedia Systems and Applications, IMSA 2007*, 2007.

[24] T. A. Witten and L. M. Sander. Diffusion-limited aggregation, a kinetic critical phenomenon. *Physical Review Letters*, 1981. doi: 10.1103/PhysRevLett.47.1400.

[25] Paul Bourke. Constrained diffusion-limited aggregation in 3 dimensions. *Computers and Graphics (Pergamon)*, 2006. doi: 10.1016/j.cag.2006.03.011.

[26] D. Wilkinson and J. F. Willemsen. Invasion percolation: A new form of percolation theory. *Journal of Physics A: Mathematical and General*, 1983. doi: 10.1088/0305-4470/16/14/028.

[27] S. R. Broadbent and J. M. Hammersley. Percolation processes: I. Crystals and mazes. *Mathematical Proceedings of the Cambridge Philosophical Society*, 1957. doi: 10.1017/S0305004100032680.

[28] R Toussaint, G Løvoll, Y Méheust, K. J Måløy, and J Schmittbuhl. Influence of pore-scale disorder on viscous fingering during drainage, 2005.
URL stacks.iop.org/0295-5075/71/i=4/a=583?key=crossref.a40877f2a9823f9199ac26828396f3dc.

[29] P.G. Saffman and F.R.S. Sir Geoffrey Taylor. The penetration of a fluid into a porous medium or Hele-Shaw cell containing a more viscous liquid. In *Dynamics of Curved Fronts*. 2014. doi: 10.1016/b978-0-08-092523-3.50017-4.

[30] R L Chuoke, P van Meurs, and C. van der Poel. The instability of slow, immiscible, viscous liquid-liquid displacements in permeable media. *Petroleum Transactions, AIME*, 1959. doi: SPE-1141-G.

[31] Lincoln Paterson. Diffusion-limited aggregation and two-fluid displacements in porous media. *Physical Review Letters*, 1984. doi: 10.1103/PhysRevLett.52.1621.

[32] Liv Furuberg, Knut Jørgen Måløy, and Jens Feder. Intermittent behavior in slow drainage. *Physical Review E - Statistical Physics, Plasmas, Fluids, and Related Interdisciplinary Topics*, 1996. doi: 10.1103/PhysRevE.53.966.

[33] Knut Jorgen Måloy, Liv Furuberg, Jens Feder, and Torstein Jossang. Dynamics of slow drainage in porous media. *Physical Review Letters*, 1992. doi: 10.1103/PhysRevLett.68.2161.

[34] G. Løvoll, M. Jankov, K. J. Måløy, R. Toussaint, J. Schmittbuhl, G. Schäfer, and Y. Méheust. Influence of Viscous Fingering on Dynamic Saturation-Pressure Curves in Porous Media, 2011.

[35] M. Moura, E. A. Fiorentino, G. Schäfer, and R. Toussaint. Impact of sample geometry on the measurement of pressure-saturation curves: Experiments and simulations. *Water Resources Research*, 2015. doi: 10.1002/2015WR017196.

[36] William B. Haines Studies in the physical properties of soil. V. The hysteresis effect in capillary properties, and the modes of moisture distribution associated therewith. *The Journal of Agricultural Science*, 20, 97-116, 1930.

[37] Steffen Berg, Holger Ott, Stephan A Klapp, Alex Schwing, Rob Neiteler, Niels Brussee, Axel Makurat, Leon Leu, Frieder Enzmann, Jens-Oliver Schwarz, Michael Kersten, Sarah Irvine, and Marco Stampanoni. Real-time 3D imaging of Haines jumps in porous media flow. *Proceedings of the National Academy of Sciences of the United States of America*, 2013. doi: 10.1073/pnas.1221373110.

[38] Arshad Kudrolli Sticky Sand. *Nature Materials*, 2008.

[39] Olav Aursjø, Marion Erpelding, Ken T. Tallakstad, Eirik G. Flekkøy, Alex Hansen and Knut J. Måløy Film flow dominated simultaneous flow of two viscous incompressible fluids through a porous medium. *Frontiers in physics*, 2014.

[40] Yves Méheust, Grunde Løvoll, Knut Jørgen Måløy, and Jean Schmittbuhl. Interface scaling in a two-dimensional porous medium under combined viscous, gravity, and capillary effects. *Physical Review E - Statistical Physics, Plasmas, Fluids, and Related Interdisciplinary Topics*, 2002. doi: 10.1103/PhysRevE.66.051603.

[41] A. Birovljev, L. Furuberg, J. Feder, T. Jssang, K. J. Mly, and A. Aharony. Gravity invasion percolation in two dimensions: Experiment and simulation. *Physical Review Letters*, 1991. doi: 10.1103/PhysRevLett.67.584.

[42] Vidar Frette, Jens Feder, Torstein Jøssang, and Paul Meakin. Buoyancy-driven fluid migration in porous media. *Physical Review Letters*, 1992. doi: 10.1103/PhysRevLett.68.3164.

[43] Grunde Løvoll, Yves Méheust, Knut Jørgen Måløy, Eyvind Aker, and Jean Schmittbuhl. Competition of gravity, capillary and viscous forces during drainage in a two-dimensional porous medium, a pore scale study, 2005.

[44] V. Frette, K. J. Måloy, F. Boger, J. Feder, T. Jossang, and Paul Meakin. Diffusion-limited-aggregation-like displacement structures in a three-dimensional porous medium. *Physical Review A*, 1990. doi: 10.1103/PhysRevA.42.3432.

[45] Vidar Frette, Jens Feder, Torstein Jøssang, Paul Meakin, and Knut Jørgen Måløy. Fast, immiscible fluid-fluid displacement in three-dimensional porous media at finite viscosity contrast. *Physical Review E*, 1994. doi: 10.1103/PhysRevE.50.2881.

[46] Marie-julie Dalbe and Ruben Juanes. Morphodynamics of Fluid-Fluid Displacement in Three-Dimensional Deformable Granular Media, 2018. URL

[47] Eugene Hecht. Optics 4th edition, 1998.

[48] Harry Edwin Burton. The Optics of Euclid, 2008.

[49] Bruce Eastwood and David C. Lindberg. Theories of Vision from Al-Kindi to Kepler, 2006.

[50] Roshdi Rashed. A Pioneer in Anaclastics: Ibn Sahl on Burning Mirrors and Lenses. *Isis*, 2002. doi: 10.1086/355456.

[51] Chris Pritchard and M. S. Mahoney. The Mathematical Career of Pierre de Fermat 1601-1665. *The Mathematical Gazette*, 2007. doi: 10.2307/3618554.

[52] Arnt Inge Vistnes. *Physics of Oscillations and Waves*. 2018. ISBN 978-3-319-72313-6. doi: 10.1007/978-3-319-72314-3.

[53] Opticks - Newtons original book, from 1704, scanned and downloaded.

[54] Wikipedia: Illustration for Fresnel's calculations, downloaded from web page.
URL en.wikipedia.org/wiki/Huygens\T1\textendashFresnel_principle#/media/File:Huygens-Fresnel_BW.svg.

[55] James Clerk Maxwell. A dynamical theory of the electromagnetic field, 1927.

[56] Andrew H. Rawicz. Theodore Harold Maiman and the invention of laser. In *Photonics, Devices, and Systems IV*, 2008. doi: 10.1117/12.817966.

[57] Wikipedia: Laser. Illustration downloaded from web-page, .
URL en.wikipedia.org/wiki/Laser#/media/File:Laser.svg.

[58] A Ulises Acun and Francisco Amat-guerri. ChemInform Abstract : Structure and Formation of the Fluorescent Compound of Structure and Formation of the Fluorescent Compound of Lignum nephriticum, 2016.

[59] Mark A Behlke, Lingyan Huang, Lisa Bogh, Scott Rose, and Eric J Devor. Fluorescence and Fluorescence Applications. *Integrated DNA Technologies*, 2005.

[60] Wikipedia: Optical lenses. Illustrations downloaded from web-page, .
URL en.wikipedia.org/wiki/Lens_(optics).

[61] Aperture blades. Illustration downloaded from web-page.
URL xlightphotography.com/wp-content/uploads/2017/10/aperture-blades.jpg.

[62] Barry R. Masters. Ernst Abbe and the Foundation of Scientific Microscopes. *Optics and Photonics News*, 2007. doi: 10.1364/opn.18.2.000018.

[63] Christopher M. Graney and Timothy P. Grayson. On the telescopic disks of stars: A review and analysis of stellar observations from the early seventeenth through the middle nineteenth centuries, 2011.

[64] Wikipedia: Airy disk. Illustration downloaded from web-page, .
URL en.wikipedia.org/wiki/Airy_disk.

[65] DSLR diagram. Illustration downloaded from web-page.
URL www.ephotozine.com/article/this-cutaway-diagram-shows-the-inside-of-a-dslr-30546.

[66] Microlens Array. Illustration downloaded from web-page.
URL micro.magnet.fsu.edu/primer/digitalimaging/concepts/microlensarray.html.

[67] Torbjørn Skauli. UNIK4330. Lecture notes.

[68] G. D. Dereniak, E. L., Boreman. *Infrared Detectors and Systems*. 1996. ISBN 9780471122098.

[69] Histogram. Illustration downloaded from web-page.
URL www.paolo9785.com/en/art/9/histogram-in-digital-photography.

[70] Wikipedia: Borosilicate glass.

[71] Glycerol - refractive index.
URL refractiveindex.info/?shelf=organic{&}book=glycerol{&}page=Rheims.

[72] M. Abbas Ali, Zahrau Bamalli Nouruddeen, Ida Idayu Muhamad, Razam Abd Latip, and Noor Hidayu Othman. Effect of microwave heating on the quality characteristics of canola oil in presence of palm olein, 2013.

[73] Ting Ting Luo. Index Of Refraction Of Vegetable Oil.
URL hypertextbook.com/facts/2006/TingTingLuo.shtml.

[74] Index of Refraction.
URL hyperphysics.phy-astr.gsu.edu/hbase/Tables/indrf.html.

[75] Refractive Index for some common Liquids, Solids and Gases.
URL www.engineeringtoolbox.com/refractive-index-d_1264.html.

[76] Wikipedia: Glycerol, .
URL en.wikipedia.org/wiki/Glycerol.

[77] Soap Association and Detergent. Glycerine: An Overview, 1990.

[78] Roman Przybylski. Canola Oil : Physical and Chemical Properties, 1992.

[79] Shreya N. Sahasrabudhe, Veronica Rodriguez-Martinez, Meghan O'Meara, and Brian E. Farkas. Density, viscosity, and surface tension of five vegetable oils at elevated temperatures: Measurement and modeling, 2017.

[80] Surface tension table.
URL www.surface-tension.de.

[81] Paul Mandel and Paul Mandel. Second harmonic generation. In *Theoretical Problems in Cavity Nonlinear Optics*. 2009. doi: 10.1017/cbo9780511529337.011.

[82] Exciton dye chart.
URL www.exciton.com/pdfs/SirahLaser.pdf.

[83] Thorlabs: filter chart.
URL www.thorlabs.com/thorproduct.cfm?partnumber=NF533-17.

[84] Nikon D7200 specifications.
URL imaging.nikon.com/lineup/dslr/d7200/spec.htm.

[85] Krüss - pendant drop method.
URL www.kruss-scientific.com/services/education-theory/glossary/pendant-drop/.

[86] Jill S Buckley, John Edwards, and Edmund Fordham. Fundamentals of Wettability. *Oilfield Review*, 2007.

[87] T. D. Blake and Y. D. Shikhmurzaev. Dynamic wetting by liquids of different viscosity. *Journal of Colloid and Interface Science*, 2002. doi: 10.1006/jcis.2002.8513.

[88] Jiayu Wang, Minh Do-Quang, James J. Cannon, Feng Yue, Yuji Suzuki, Gustav Amberg, and Junichiro Shiomi. Surface structure determines dynamic wetting. *Scientific Reports*, 2014. doi: 10.1038/srep08474.

[89] Pressure Sensor. Image downloaded from a web-page.
URL sensing.honeywell.com/2XPCXXG6G-highres-photo.jpg.

[90] Xiang-zhao Kong Markus Holzner, Fritz Stauffer, and Wolfgang Kinzelbach. Time-resolved 3D visualization of air injection in a liquid-saturated refractive-index-matched porous medium, 2011.

[91] S. M. Shah, J. P. Crawshaw, and E. S. Boek. Three-dimensional imaging of porous media using confocal laser scanning microscopy, 2017.

[92] Joris Heyman, Daniel Lester, and M Yves. Transverse mixing in 3D porous flows : experimental results & stochastic inference . pages 2–3.

[93] S B G O Brien and L. W. Schwartz. Theory and Modeling of thin film flows. *Encyclopedia of Surface and Colloid Science*, 2002. doi: 10.1081/E-ESCS-120000885.

[94] A. Ahmadi-Sénichault, V. Canseco, N. Sefrioui-Chaibainou, A. Omari, and H. Bertin. Displacement of Colloidal Dispersions in Porous Media: Experimental & Numerical Approaches. *Diffusion Foundations*, 2016. doi: 10.4028/www.scientific.net/df.7.53.

[95] Jean Schmittbuhl, Alex Hansen, Harold Auradou, and Knut Jørgen Måløy. Geometry and dynamics of invasion percolation with correlated buoyancy. *Physical Review E - Statistical Physics, Plasmas, Fluids, and Related Interdisciplinary Topics*, 2000. doi: 10.1103/PhysRevE.61.3985.

[96] H. Auradou, K. J. Måløy, J. Schmittbuhl, and Alex Hansen. Drainage in a rough gouge-filled fracture. *Transport in Porous Media*, 2003. doi: 10.1023/A:1021164109061.

[97] Aleksandar Birovljev, Geri Wagner, Paul Meakin, Jens Feder, and Torstein Jøssang. Migration and fragmentation of invasion percolation clusters in two-dimensional porous media. *Physical Review E*, 1995. doi: 10.1103/PhysRevE.51.5911.

[98] G. Wagner, A. Birovljev, P. Meakin, J. Feder, and T. Jøssang. Fragmentation and migration of invasion percolation clusters: Experiments and simulations. *Physical Review E - Statistical Physics, Plasmas, Fluids, and Related Interdisciplinary Topics*, 1997. doi: 10.1103/PhysRevE.55.7015.

[99] Paul Meakin. Diffusion-controlled cluster formation in two, three, and four dimensions. *Physical Review A*, 1983. doi: 10.1103/PhysRevA.27.604.

[100] Gérard Daccord and Roland Lenormand. Fractal patterns from chemical dissolution. *Nature*, 1987. doi: 10.1038/325041a0.

[101] June Kyoo Lee, Kyung Woo Park, Geunbae Lim, Hak Rin Kim, and Seong Ho Kong. Variable-focus Liquid Lens Based on a Laterally-integrated Thermopneumatic Actuator, 2012. 12264776.

[102] G. L. Squires. Practical Physics, 2003.

[103] Me. Vastly underestimated survey of the actual number of sock pairs, as well as solitary socks, in my sock drawer.